ELECTRONIC AND MAGNETIC PROPERTIES OF METALLIC AND ALLOY SURFACES.

THESIS SUBMITTED FOR THE DEGREE OF
DOCTOR OF PHILOSOPHY (SCIENCE)
OF THE
WEST BENGAL UNIVERSITY OF TECHNOLOGY

MONODEEP CHAKRABORTY
SATYENDRANATH BOSE NATIONAL CENTRE
FOR BASIC SCIENCES
JD BLOCK, SECTOR 3, SALT LAKE CITY
KOLKATA 700 098, INDIA

JUNE, 2006

CERTIFICATE FROM THE SUPERVISOR

This is to certify that the thesis entitled **E**lectronic and magnetic properties of metallic alloys and surfaces submitted by Monodeep Chakraborty, who has been registered by the **W**est **B**engal **U**niversity of **T**echnology for the award of **Ph.D.** (**S**cience) degree, is absolutely based upon his own work under the supervision of **P**rofessor **A**bhijit Mookerjee at **S. N. B**ose National **C**entre **F**or **B**asic Sciences, **K**olkata, **I**ndia and that neither this thesis nor any part of it has been submitted for any degree/diploma or any other academic award anywhere before.

ABHIJIT MOOKERJEE
Senior Professor,
Dean (Faculty),
Satyendranath Bose National Centre For Basic Sciences,
JD Block, Sector 3, Salt Lake City, Kolkata 700 098
India
Date :

Acknowledgments

At the end of my Ph.D, the hour has arrived where I would like to recollect with gratitude and humility all the people who made this possible for me. First of all I would take this opportunity to express my gratitude to my supervisor Professor Abhijit Mookerjee for inspiring and encouraging me to pursue the field of surface science. Not only he helped me at every step but also provided abundant independence to do my work. I would also like to thank Professor Kajal Ghosh Ray of Saha Institute of Nuclear Physics, who initially introduced me into this field. I would like to thank Dr. Sugata Mukherjee and Dr. Tanusri Saha-Dasgupta for their very useful discussion and advices. I would like to thank Dr. P.A. Sreeram for his extremely useful suggestions. I would thank Dr. Jayita Chatterjee for many useful discussions. I would like to thank all my research colleagues, who made my stay here a very memorable experience. My academic discussions with Mr. Kamal Krishna Saha, Mr. Kartick Tarafdar, Mr. Soumendu Dutta and Mr. Debashis Chowdhury helped me to learn a lot of new things. Words are not enough to describe the role played by Mr. Atisdipankar Chakrabarti, my friend for last eleven years. We have discussed, argued and learned things together. All my relatives, specially my parents and my grandparents left no stone unturned to see me properly educated. My wife Mohua who joined me few months back, took every pain with a smile, to see that I could complete my thesis comfortably. Last but not the least I would thank every woman and man of my country who brave unsurmountable odds,but contribute their hard earned money to the national exchequer(in form of taxes) to ensure that the lamp of learning keeps burning in this ancient land.

List of Publications

1. **E**lectronic structure and magnetism of Nickel **T**hin **F**ilms
   Monodeep Chakraborty, Abhijit Mookerjee and Ashok K. Bhattacharya
   International Journal of Modern Physics B 17 (2003) 5839-5848.

2. Magnetism in surfaces: an orbital-resolved study
   Monodeep Chakraborty, Abhijit Mookerjee and Ashok K. Bhattacharya
   Journal of Magnetism and Magnetic Materials **285** (2005) 210-223.

3. **T**he Study of electronic and magnetic properties of the partially disordered pseudo-**H**eusler alloy $\mathbf{Co_2Fe_{0.4}Cr_{0.6}Al}$: an augmented space approach
   Monodeep Chakraborty,Atisdipankar Chakrabarti and Abhijit Mookerjee
   Communicated to Journal of Magnetism and Magnetic Materials.

4. Study of the one dimensional **H**olstein model using the augmented space approach
   Atisdipankar Chakrabarti, Monodeep Chakraborty and Abhijit Mookerjee
   Accepted for publication in Physica B

5. **E**lectron-**P**honon interaction in ground state: a real space study
   Monodeep Chakraborty,Atisdipankar Chakrabarti and Abhijit Mookerjee
   Communicated to Physica B

Contents

List of Figures

List of Tables

Chapter 1

A brief overview of theoretical studies of surfaces and thin Films.

1.1 Introduction

Surfaces are the first line of defence of any substance in its interaction with its surroundings. This is precisely the reason, that knowledge about material surfaces has become indispensable in order to produce novel materials which will aid the technological and scientific advancement of the human civilization.

One of the interesting features of magnetism at a surface is the modification of the surface magnetic moment because of difference between atomic environments in the surface and the bulk. The study of surface magnetism had a dramatic start, when it was suggested that *dead* or paramagnetic layers in overlayers of Ni were formed when they were deposited on Cu (Liebermann *et al* 1969). But those controversies have now been laid to rest with new and more sophisticated experiments refuting the earlier controversial findings. Another exotic feature of surface magnetism is its anisotropy, which has immense potential for industrial applications.

In bulk materials where we have lattice translational symmetry, Bloch Theorem based reciprocal space methods are used to determine their electronic and magnetic structures. But for surfaces and thin films this translational symmetry is lost. If we are dealing with a (001) surface, there still exits a remnant translational symmetry in the x-y plane, while that in the z-direction is lost. Therefore one can still take advantage of this planar

symmetry and use the Green function techniques. Alden *et al* 1992 have utilized the two-dimensional periodicity on flat surfaces to deal with a two-dimensional reciprocal space while treating the direction perpendicular to the surface by a real-space method.

For a rough surface(100) even this planar symmetry is lost . In such a scenario we cannot afford the comfort of reciprocal space based methods. The real space based "Recursion method" (Haydock *et al* 1972, Haydock 1980) is an alternative , as it does not take recourse to any translational symmetry.

In chapter 2 we have first carried out TB-LMTO *super cell* calculations for ordered thin films . Then we performed a real space recursion with the TB-LMTO *super cell* Hamiltonian. We have calculated the orbital(ℓ-m-m_s) resolved Local density of States(LDOS) and magnetic moments for different layers of the thin film. We obtained surface enhancement of magnetic moment for body-centered cubic Fe(100) and Cr(100), face-centered cubic Co(100), Ni(100), Ni(110) and Ni(111), hexagonal closed-packed Co(100) nine-layered thin films. Our results (Chakraborty *et al* 2003, Chakraborty *et al* 2005) matched well with the existing results. In addition, our (ℓ-m) resolved moments and (ℓ-m-m_s) resolved charge revealed some interesting facts (Chakraborty *et al* 2005). We found that all the d-orbitals do not contribute to the surface magnetic enhancement , on the contrary the surface magnetic moment of some d-orbitals are suppressed (in some cases like face-centered cubic Ni(100) and Ni(111) surface).In fact it is the way in which the electronic charge redistributes among the different d-states, that determines their contribution to the surface enhancement. The s and p states in some cases (like face-centered cubic Ni(100)and hexagonal closed-packed Co(100) where the enhancement is feeble) facilitate the surface enhancement. We also observed a *Friedel* like oscillation in the charge and magnetic moments of the layers of thin films. We have also applied the recursion method to see how different types of roughness affects the surface magnetism in Ni(100) and Fe(100) surfaces.

Substitutionally disorder is a common occurrence in the field of materials and is of immense importance, both from the point of view of physics as well as technology. Partial disorder is another form of substitutional disorder where some of the sub-lattices are ordered while others are disordered. This generally occurs when we are slightly away from stoichiometry(example Cu_3Au). In chapter 3 we have dealt with the partial disorder

in bulk and thin film(100) of $Co_2Fr_xCr_{1-x}Al$ a doped quaternary Heusler alloy in $L2_1$ phase. The Heusler compounds are of great technological importance as they are potential candidate for application in spintronics, since many of them exhibit the property of half-metallicity. For partially disordered bulk, thin films and surfaces of $Co_2Fr_xCr_{1-x}Al$, we have employed the augmented space formalism (Mookerjee 1973) in conjunction with TB-LMTO super-cell calculation. The augmented space theorem which calculates configuration averaged quantities , is one of the most elegant methods to do the configuration averaging in disordered systems.

In chapter 4 we have studied the effect of electron-phonon interaction in ground state for chemically uniform and alternating 1-d lattice and a trilayered thin film(100) in real space. We have achieved an excellent matching with the ground state K-space results(Chakrabarti *et al* 2006, Bonca *et al* 1999) for the uniform 1-d lattice and then we have applied our real space methodology to study the ground state electron-phonon interactions in a chemically alternating lattice and a trilayered thin film. The advantage of the real space method is that, it can be applied to cases where one cannot do reciprocal space calculations.

1.2 Review of the basic theoretical tools.

In the following two sections we shall review the two basic theoretical tools we shall use subsequently in the course of all our work : the density functional theory and the linear muffin-tin orbitals method. In the next two chapters we shall take the outcomes of these two methods and modify them to suit our problem at hand.

The cohesive, electronic, optical, magnetic and superconducting properties of solids are dominated by the behaviour of valence electrons moving in the field of the ion-cores of the constituent atoms. Ion-cores are the nuclei together with the core electrons which do not participate in bonding in solid. This many-body problem is impossibly difficult to solve without introducing simplifying, but reasonable approximations. Explanation of different properties of the solid requires different levels of sophistication in the treatment of electron-electron correlations.

One level of sophistication is the density functional theory (DFT). The DFT is a

self-consistent field approximation which reduces this many-body problem to essentially a one-electron one and has been the basis of the band theory of solids. It has proved to be immensely successful, especially in the physics of metals and semiconductors. It provides us with the most handy first-principles technique to verify, as well as predict, the properties of materials with quantitative accuracy. Today it is possible, for example, to calculate total energies of solids with $\sim$ 50-100 mRyd. accuracy, so that we may investigate surface reconstruction, interface relaxation or bond formation with confidence (Das 1998). The developments of band structure methods have been well documented.

Our aim here is to review the energy band description of solids based on the density functional approach which maps the ground state of an interacting electron gas onto the ground state of non-interacting electrons that experience an effective potential. The most crucial term in this effective potential is the exchange-correlation potential whose origin lie in the quantum mechanical and electrostatic interactions between the electrons. One electron band structure methods, where this exchange-correlation term is treated in a mean-field sense, is surprisingly successful in yielding the correct ground state properties of a large variety of solids that are of interest in material science have been recently tackled with *chemical accuracy*. To a limited extent, it is also successful in describing single particle excitations due to prodding the materials with photons, electric and magnetic field, temperature etc. , although there are limitations of band theory in explaining strongly correlated phenomena.

We shall concentrate on the Korringa-Kohn-Rostocker (KKR) scattering approach to band structure and its linearized version : the linear muffin-tin orbitals technique (LMTO). The advantages of the technique are :

(a) it leads to the Hamiltonian and overlap matrices with smallest rank and hence fastest from the computational point of view, in particular in dealing with complex solids with many atoms per unit cell.

(b) it is possible to define a localized basis such that the Hamiltonian can be recast in a tight-binding form which can be solved in reciprocal as well as real space. For handling non-periodic systems where k is no more a good quantum number and real space methods are extremely important.

1.3 The density functional theory

We start learning quantum mechanics with the simplest electron-nucleus system, for example, the hydrogen atom whose Schrödinger equation

$$\left[-\nabla^2 + V(r)\right]\ \psi_n(r) = E_n\psi_n(r), \tag{1.1}$$

can be exactly solved as the potential energy $V(r)$ of the electron in the electrostatic field of the proton is known to be $-2/r$ where r is the electron-nucleus distance. We shall use Rydberg units with $\hbar$=1, e^2=2, m=$\frac{1}{2}$, a_0=$\hbar^2/me^2$=0.52918$\times10^{-8}$cm for the unit of length and Rydberg ($e^2/2a_0$)=13.6057 for the unit of energy. The wave function $\psi_n(r)$ and the energy levels E_n are obtainable analytically. However, as we move towards higher Z elements and their compounds, the electrostatic repulsion amongst multiple electrons in presence of attractive centres, the ion-cores, make the exact solution of the problem intractable. The only plausible way is to somehow replace the many-electron problem to an effective one-electron problem; but this has to be at the cost of introducing certain approximations. To start with we decouple the ionic and electronic motions via the Born-Oppenheimer (or adiabatic) approximation. The second is the DFT which reduces the many-body problem to an equivalent single-electron one. This DFT was proposed by Hohenberg and Kohn 1978 and Kohn and Sham 1965. The basic idea of DFT originated from the query, *"Can we arrive at a potential V(r) uniquely; given the charge density $\rho(r)$ of the system ?"*. Our conventional wisdom of the Schrödinger and Poisson equations suggests that the converse is true anyway, i.e. given $V(r)$, one can easily obtain $\rho(r)$. It is this unique search prescription, that is at the heart of the DFT.

More formally, Hohenberg-Kohn theorem expresses the total energy of an electron-nucleus system as a functional of the electron density and also proves that for a fixed external potential $V_{ext}(r)$, the energy functional $E[\rho(r)]$ is minimum for the true ground state density $\rho_o(r)$.

The *Total Energy functional* for a system containing interacting electrons in presence of nuclei can be written in terms of density as

$$\begin{aligned} E[\rho(r),\{R\}] &= E_{el}[\rho(r),\{R\}] + E_{ion}[\{R,R'\}] \\ &= T_s[\rho] + E_{xc}[\rho] + E_{ES}[\rho,\{R\}] \end{aligned}$$

where R and R' denote the nuclear coordinates. Here $T_s[\rho]$ is the kinetic energy of a non-interacting electron gas of the same density as that of the actual interacting system, $E_{xc}[\rho]$ is the exchange-correlation energy including the correction term $(T - T_s)$ to the kinetic energy, $E_{ES}[\rho]$ is the total electrostatic energy, *i.e.* energies due to classical electron-electron Coulomb (or Hartree) potential, external potential and ion-ion Madelung potential. This last term, written explicitly in terms of the electronic and ionic coordinates, takes the form

$$\begin{aligned} E_{ES}[\rho] &= E_H[\rho] + E_{ext}[\rho,\{R\}] + E_{Mad}(\{R,R'\}) \\ &= \int\int \frac{\rho(r)\rho(r')}{|r-r'|} dr\,dr' + \int V_{ext}(r)\rho(r)dr + \sum_{R,R'} \frac{Z_R Z_{R'}}{|R-R'|} \end{aligned}$$

On applying variational principle on $E^{el}[\rho(r)]$ i.e. making total energy stationary with respect to the first-order variation in the density, $\delta E[\rho]/\delta\rho|_{\rho=\rho_o} = 0$, one arrives at the Euler equation

$$\delta\{E^{el}[\rho(r)] - \mu \int \rho(r)dr\} = 0$$

where μ is the Lagrange multiplier, which turns out to be the *chemical potential* of the system. Solution of this Euler equation yields the so-called Kohn-Sham (KS) equation :

$$\left[-\nabla^2 + V_{eff}(r)\right]\ \psi_i(r) = \varepsilon_i \psi_i(r), \tag{1.2}$$

where the effective potential

$$V_{eff}(r) = 2\int dr' \frac{\rho(r')}{|\,r-r'\,|} + 2\sum_R \frac{Z_R}{|\,r-R\,|} + \frac{\delta E_{xc}[\rho]}{\delta\rho(r)} \tag{1.3}$$

consists of the Hartree potential Φ *(first term)*, the external or ionic potential V_{ext} *(second term)* and the exchange-correlation potential μ_{xc} *(third term)*. The KS equation represents a mapping of the interacting many-electron system onto a system of non-interacting electrons moving in an effective potential due to all other electrons and ions. The crucial quantity in this scheme is $E_{xc}[\rho]$, since an exact knowledge of this functional implies that the exact solution of the entire many body problem is known !

In terms of the one-electron eigenfunction $\psi_i(r)$ and occupancy f_i, the density is obtained as

$$\rho(r) = \sum_i f_i |\psi_i(r)|^2 \tag{1.4}$$

and the resulting energy functional is

$$\begin{aligned} E[\{\psi_i\}, R] &= -\sum_i^{occ} n_i \int \psi_i^*(r)\nabla^2\psi_i(r)dr + \int dr\rho(r)V_{ext}(r) \\ &+ \int\int \frac{\rho(r)\rho(r')}{\mid r - r' \mid} dr dr' + E_{xc}[\rho(r)] + \sum_{R,R'} \frac{Z_R Z_{R'}}{\mid R - R' \mid} \end{aligned} \tag{1.5}$$

It is to be noted that this KS Equation(1.2) is of the same form as the Schrödinger equation(1.1) for a hydrogen atom, excepting for the fact that the effective potential contains, amongst other terms, the exchange-correlation (XC) energy term, the exact form of which is unfortunately not known. One needs to introduce some approximation and the most successful and well tested is the so called local density approximation (LDA) which was first introduced by Slater for simplifying the non-local exchange energy in terms of the local $\rho^{1/3}$ potential. The local approximation essentially amounts to the assumption that the XC-energy density depends only on the *local electron density* $\rho(r)$ around each volume element dr i.e.

$$E_{xc}^{LDA} \simeq \int \rho(r)\varepsilon_{xc}[\rho(r)]\, dr$$

The XC-energy density $\varepsilon_{xc}[\rho(r)]$ of a homogeneous electron gas has been calculated by several approaches : (a) many-body perturbation theory (b) quantum Monte-Carlo

method. Amongst which the most widely used XC potentials used are the Barth-Hedin (von Barth and Hedin 1972) and the Ceperley-Alder XC parameterizations.

The energy functional in equation(1.5) is *variational* which means that a self-consistent solution of the KS equation (1.2) leads to the true ground state density. In practice, one can use some trial V_{eff} (which need not be the exact self-consistent value), solve the KS equation to get $\psi_i(r)$ and hence the output total electronic charge density $\rho(r)$, which in turn can be used as a new input charge density in the self-consistency loop. The cumbersome part is that $T_s[\rho]$ can not be evaluated unless ρ is calculated via the equation (1.4) from the eigenfunctions ψ_i of the single-particle KS equation for some potential V_{eff}. Nevertheless, it is this orbital structure dependence of T_s in the KS scheme (unlike say in Thomas-Fermi-Dirac theory) that enables it to describe all kinds of chemical behaviour. In actual computation, the K.E. is expressed as the difference between the total energy and the potential energy of the non-interacting electrons in the potential V_{eff}

$$T_s = -\sum_i^{occ} n_i \langle \psi_i \mid \nabla^2 \mid \psi_i \rangle = \int^{E_F} \varepsilon n(\varepsilon) d\varepsilon - \int V_{eff}(r)\rho(r) dr$$

Here, the first term on the right hand side is the occupied one-electron band energy which can be expressed in terms of the density of states (DOS) $N(\varepsilon)$. The KS total energy expression (Equation (1.3)) therefore can be recast as

$$E^{KS}[\rho] = \int^{E_F} \varepsilon n(\varepsilon) d\varepsilon - \int \left[\frac{1}{2}\Phi + \mu_{xc}\right] \rho(r)\, dr + E_{xc}^{LDA} + E_{Mad} \qquad (1.6)$$

It is this expression which is used in practice in all the one-electron band structure total energy computational schemes, and we shall come back to it in a later section.

In order to handle magnetic systems, one needs spin-polarized calculations, for which the local spin density approximation (LSDA) has to be invoked instead of LDA. The fundamental quantity $\rho(r)$ is then replaced by two quantities : *spin-up density* $\rho_\uparrow(r)$ and *spin-down density* $\rho_\downarrow(r)$, which in turn define the *total charge density* $\rho(r)$ and the *spin density* $\sigma(r)$ as

$$\rho(r) = \rho_\uparrow(r) + \rho_\downarrow(r) \qquad \sigma(r) = \rho_\uparrow(r) - \rho_\downarrow(r)$$

Accordingly one has to calculate two sets of single-particle wave functions for up-spin

and down-spin electrons, with the corresponding one-electron eigenvalues from the spin-polarized KS equation which takes the form

$$[-\nabla^2 + V^{\sigma}_{eff}(r)]\ \psi^{\sigma}_i(r) = \varepsilon^{\sigma}_i \psi^{\sigma}_i(r),$$

where σ denotes the spin index (up or down). Obviously for equal spin-up and spin-down densities, $\sigma(r)$ is zero throughout the real space and LSDA becomes identical with the LDA approach.

The LDA and the LSDA have proved to be astonishingly successful for many condensed matter systems (Jones and Gunnarsson 1989). However, one must keep in mind that the success is restricted mainly to ground state properties, and not rigorously for excited state properties. The KS eigenvalues ε_i are only loosely interpreted as single-particle excitation energies, although the so-called Janak's theorem rigorously proved that the highest ε_i^{DFT} corresponds to the exact ionization energy. The facts remain that LDA underestimates the band-gaps in semiconductors and insulators, overestimates bonding (cohesive energy) in a solid and fails to describe the ground state of highly correlated systems e.g. Mott insulators such as NiO. Because of all these, there have been attempts in the recent past to improve upon the correlation effects with better energy functionals, but still remaining within the purview of DFT.

1.4 Multiple scattering approaches to electronic structure

1.4.1 The Muffin-tin potential and partial wave solutions

The local density functional approximation (LDA), discussed in the earlier sections, reduces the many-body Hamiltonian of the valence electron cloud in the presence of a 'frozen' array of ion-cores. The effective Hamiltonian as seen by an electron within the LDA is :

$$V(\underline{r}) \ = \ \sum_{\underline{R}} \ v(\underline{r} - \underline{R})$$

where $\underline{R}$ are the positions of the ion-cores and $\underline{r}$ is the position of the electron.

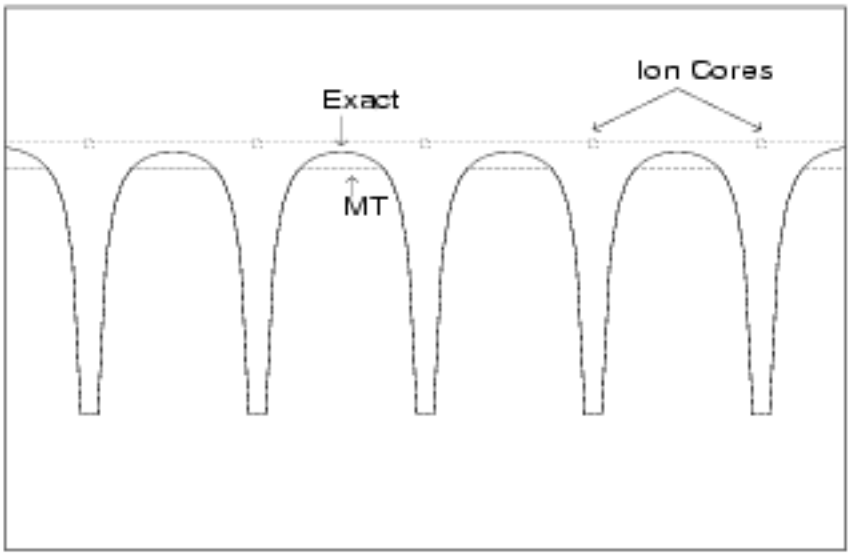

Figure 1.1: The construction of the muffin-tin potential

In the neighbourhood of an ion-core the potential seen by the electron in a solid is not very different from that in the atom whose ion-core we are focussing on. We shall define a radius s_R around R within which we shall assume that the potential is spherically symmetric. These spheres will be called the *muffin-tin spheres*. In the *interstitial*, that is the rest of the space from which the muffin-tin spheres are carved out, the potential varies very slowly. We shall replace the potential in this region by a constant average. The resulting potential is called a *Muffin-tin Potential*. A schematic diagram showing the approximation is the figure 1.1 above. A more realistic illustration comparing a full potential with a muffin-tin one, is shown in figure 1.2.

Before we attempt to solve the full problem of an electron in a solid, let us first examine the problem of an electron in a single muffin-tin potential. This potential is given by :

$$v(\underline{r}-\underline{R}) = \begin{cases} v(r_R) & \text{for} \quad r_R \leq s_R \qquad r_R = |\underline{r}-\underline{R}| \\ -v_0 & \text{for} \quad r_R > s_R \end{cases}$$

and the Schrödinger equation for the single electron wave-function is given by :

$$\left[-\frac{\hbar^2}{2m} \nabla^2 + v(\underline{r}-\underline{R}) \right] \phi(\underline{r}-\underline{R},\varepsilon) \;=\; \varepsilon\, \phi(\underline{r}-\underline{R},\varepsilon)$$

We may immediately solve the above equation in the region $r_R \;\leq\; s_R$, in which the

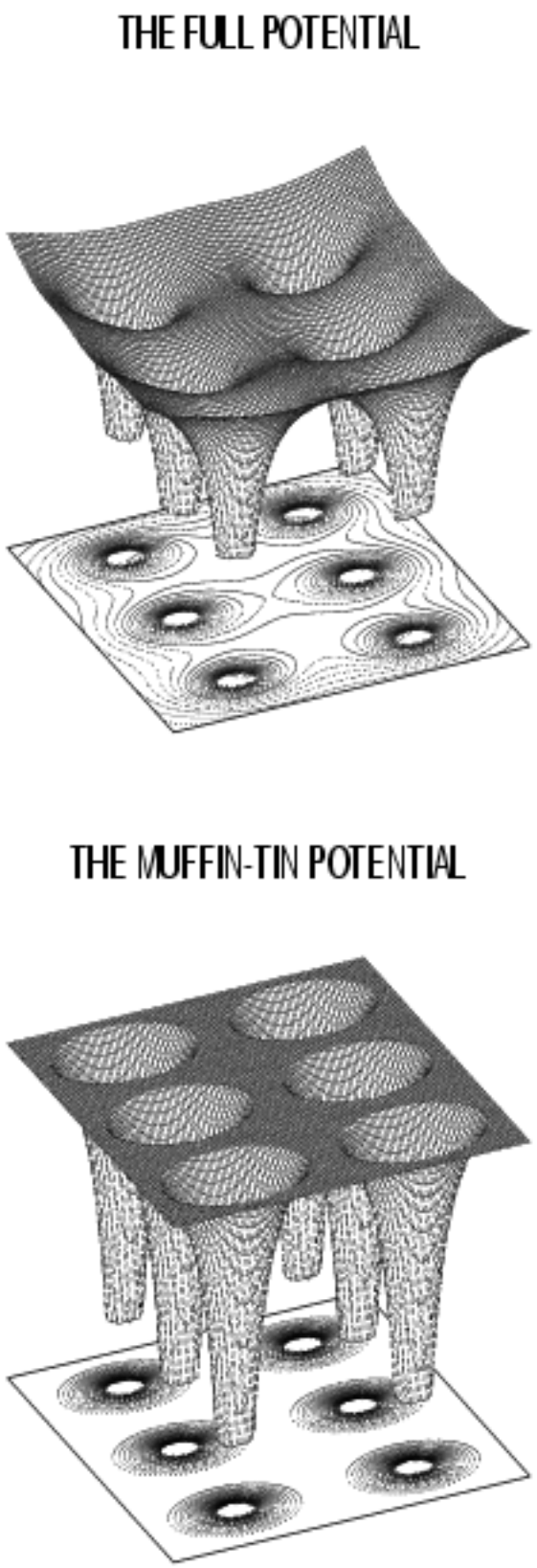

Figure 1.2: Comparison between a full- and a muffin-tin potential

potential is spherically symmetric and

$$\phi(\underline{r} - \underline{R}) \;=\; \varphi_{RL}(r_R, \varepsilon)\; Y_L(\hat{r}_R) \tag{1.7}$$

Here L denotes the angular momentum labels (ℓ, m), $Y_L(\hat{r})$ are the spherical harmonic functions and $\hat{r}_R$ are the angular variables associated with the unit vector $(\underline{r} - \underline{R})/r_R$. $\phi_{RL}(r_R, \varepsilon)$ are solutions of the radial equation :

$$\left[\frac{d^2}{dr_R^2} \;-\; v(r_R) \;+\; \frac{\ell(\ell+1)}{r_R^2} \;-\; \varepsilon\right] r_R \varphi_{RL}(r_R, \varepsilon) \;=\; 0 \tag{1.8}$$

This solution is regular at $\underline{r} = \underline{R}$ and behaves like r_R^{ℓ} as $r_R \to 0$. Outside the muffin-tin sphere the potential is a constant. Again the wave-function factorizes as in equation 1.7. The solution of the radial equation with a constant $v(r_R) = -v_0$

$$\left[\frac{d^2}{dr_R^2} \;+\; \frac{\ell(\ell+1)}{r_R^2} \;-\; \kappa^2\right] r_R \varphi_{RL}(r_R, \varepsilon) \;=\; 0$$

are the spherical Bessel and Neumann functions and $\kappa^2 \;=\; \varepsilon - v_0$. Since $\underline{r} = \underline{R}$ is not included in this region, both the solutions are allowed and the full solution in this region is the linear combination :

$$A_{R\ell}(\varepsilon, \kappa)\; j_\ell(\kappa r_R) \;+\; B_{R\ell}(\varepsilon, \kappa)\; n_\ell(\kappa r_R)$$

If we now invoke the boundary condition that on the muffin-tin sphere both the wave-function and its derivative are continuous, we get

$$\begin{aligned} A_{R\ell}(\varepsilon, \kappa) \;&=\; \frac{\{\varphi_{RL}(r_R, \varepsilon), n_\ell(\kappa r_R)\}}{\{j_\ell(\kappa r_R), n_\ell(\kappa r_R)\}} \\ B_{R\ell}(\varepsilon, \kappa) \;&=\; \frac{\{\varphi_{RL}(r_R, \varepsilon), j_\ell(\kappa r_R)\}}{\{n_\ell(\kappa r_R), j_\ell(\kappa r_R)\}} \end{aligned} \tag{1.9}$$

Here the Wronskian is defined as follows :

$$\{f(r), g(r)\} \;=\; f(r)\frac{\partial g(r)}{\partial r} \;-\; g(r)\frac{\partial f(r)}{\partial r}$$

The scattering phase shift is given by,

$$\cot \eta_{RL}(\varepsilon,\kappa) \;=\; \frac{A_{RL}(\varepsilon,\kappa)}{B_{RL}(\varepsilon,\kappa)} \;=\; -\left.\frac{\{\varphi_{RL}(\varepsilon,r_R),n_L(\kappa r_R)\}}{\{\varphi_{RL}(\varepsilon,r_R),j_L(\kappa,r_R)\}}\right|_{r_R=s_R}$$

The potential function is given by :

$$\begin{aligned} P^{o}_{RL}(\varepsilon,\kappa) \;&=\; -\cot \eta_{RL}(\varepsilon,\kappa) \\ &=\; \left.\frac{n_L(\kappa r_R)\Big[D[n_L(\kappa r_R)]-D[\varphi_{RL}(\varepsilon,r_R)]\Big]}{j_L(\kappa r_R)\Big[D[j_L(\kappa r_R)]-D[\varphi_{RL}(\varepsilon,r_R)]\Big]}\right|_{r_R=s_R} \end{aligned} \tag{1.10}$$

where $D[f(r)]$ is the scaled logarithmic derivative

$$D[f(r)] \;=\; \frac{r}{f(r)}\frac{\partial f(r)}{\partial r}$$

It follows immediately from equations (1.9) and (1.10) that the potential functions or the phase shifts are dependent on the muffin-tin potential. They, in fact, carry the signature of the potential. In inverse scattering problems, we actually experimentally measure the phase shifts and infer about the potential from them.

The *partial wave* solution in all space is then :

$$\varphi_{RL}(r_R,\varepsilon) \;=\; \begin{cases} N^{o}_{RL}(\varepsilon,\kappa)\;\varphi_{RL}(r_R,\varepsilon) & \text{if} \quad r_R \le s_R \\ n_L(\kappa r_R) \;-\; P^{o}_{RL}(\varepsilon,\kappa)\;j_L(\kappa r_R) & \text{if} \quad r_R > s_R \end{cases} \tag{1.11}$$

$N^{o}_{RL}(\varepsilon)$ is a normalization constant. In case we already ensure that the head of the partial wave is normalized within the muffin-tin sphere centred at R,

$$\int_0^{s} dr\; r^2\,\varphi_{RL}(r_R,\varepsilon) \;=\; 1$$

then, $N^{o}_{RL}(\varepsilon)=1$. However, we shall retain this factor for future reference.

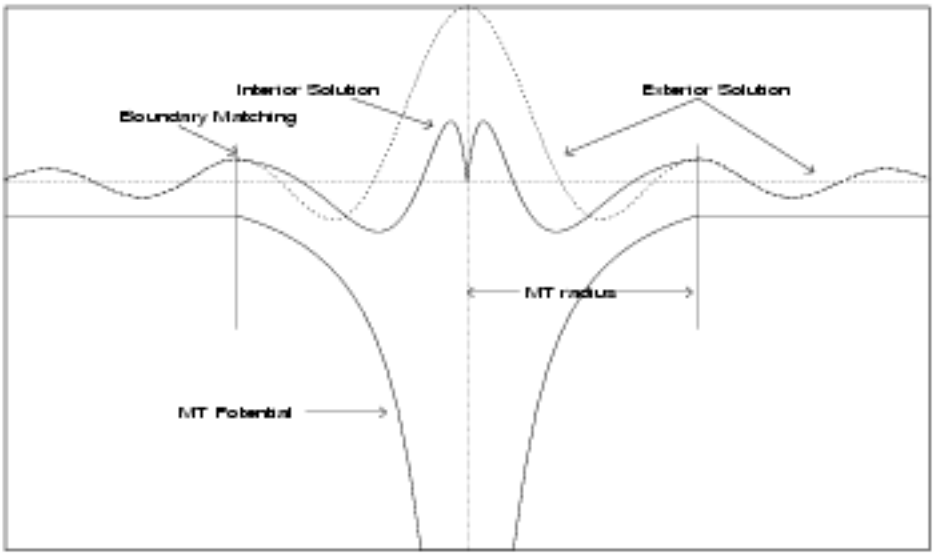

Figure 1.3: Construction of muffin-tin orbitals

The part of the partial wave within its muffin-tin sphere (that centred at $r = R$, often referred to as its *personal* sphere) is called its *head*, while the part outside its personal sphere is called its *tail*.

1.4.2 Muffin-tin orbitals and tail cancellation

The partial waves are not adequate as a basis for the following reason : we would like a basis to be such that its *head* contains all the information about the potential, while its *tail* contains information only about the constant potential outside the muffin-tin sphere. In addition, we would like the basis not to be a badly behaved function anywhere in space. A way of choosing such a basis is as follows :

$$\chi_{RL}(r_R,\varepsilon) \;=\; \begin{cases} \left[N^{o}_{RL}(\varepsilon,\kappa)\,\varphi_{RL}(r_R,\varepsilon) \;+\; P^{o}_{RL}(\varepsilon,\kappa)\,j_l(\kappa r_R)\right] & \text{if} \quad r_R \le s_R \\ n_l(\kappa r_R) & \text{if} \quad r_R > s_R \end{cases} \tag{1.12}$$

The equation (1.10) ensures that the head and the tails of the above function match continuously and differentiably at the muffin-tin boundary at s_R. These functions are called *Muffin-tin Orbitals* (MTO) and qualify as suitable basis for representation of the wave function in the solid.

We can think about the construction of the muffin-tin orbitals as follows : We start from the Neumann function $n_L(\kappa r_R)$ defined in *all* space. We now retain the part in its *tail* and replace the *head* by the function $N^o_{RL}(\varepsilon)\,\varphi_{RL}(r_R,\varepsilon) \;+\; P^o_{RL}(\varepsilon,\kappa)\,j_L(\kappa r_R)$ which joins smoothly and differentiably with the tail. This is illustrated in the figure (1.3).

So far we have been discussing the partial waves and muffin-tin orbitals associated with a single muffin-tin potential. Let us now introduce the wave-function solution of the solid muffin-tin potential of the type shown in figure (1.1). We shall expand this wave-function as a linear combination of the muffin-tin orbitals associated with individual muffin-tin potentials centred at different sites $\{R\}$:

$$\Psi(r,\varepsilon) \;=\; \sum_R \sum_L c_{RL}(\varepsilon)\,\chi_{RL}(r-R,\varepsilon) \tag{1.13}$$

In what follows we shall also use the expression for the tail of the Neumann function $n_L(\kappa r_R)$ outside its *personal* sphere :

$$n_L(\kappa r_R) \;=\; -\sum_{L'} S^o_{RL,R'L'}(\kappa)\; j_{L'}(\kappa r_{R'}) \tag{1.14}$$

Here $S^o_{RL,R'L'}(\kappa)$ are the canonical structure constants which depend upon the relative position of R' with respect to R and have nothing to do with the ion-core potentials that sit at those sites.

Now, if we refer to figure (1.4), we note that the MTO can be written as :

$$\chi_{RL}(r-R,\varepsilon) \;=\; \begin{cases} \left[N^o_{RL}(\varepsilon,\kappa)\,\varphi_{RL}(r_R,\varepsilon) \;+\; P^o_{RL}(\varepsilon,\kappa)\,j_L(\kappa r_R)\right] Y_L(\hat{r}_R) & \text{if} \quad r_R \le s_R \\ -\;\sum_{L'} j_{L'}(\kappa r_{R'})\; S^o_{R'L',RL}(\kappa)\; Y_L(\hat{r}_R) & \text{if} \quad r_{R'} \le s_{R'} \\ -\;\sum_{L'} j_{L'}(\kappa r_{R''})\; S^o_{R''L',RL}(\kappa)\; Y_L(\hat{r}_R) & \text{if} \quad r_{R''} \le s_{R''} \\ \cdots\cdots \quad \cdots\cdots \quad \cdots\cdots \quad \cdots\cdots & \\ n_L(\kappa r_R)\; Y_L(\hat{r}_R) & \text{if} \quad r_R \in \text{interst.} \end{cases} \tag{1.15}$$

We shall now introduce a convenient notation :

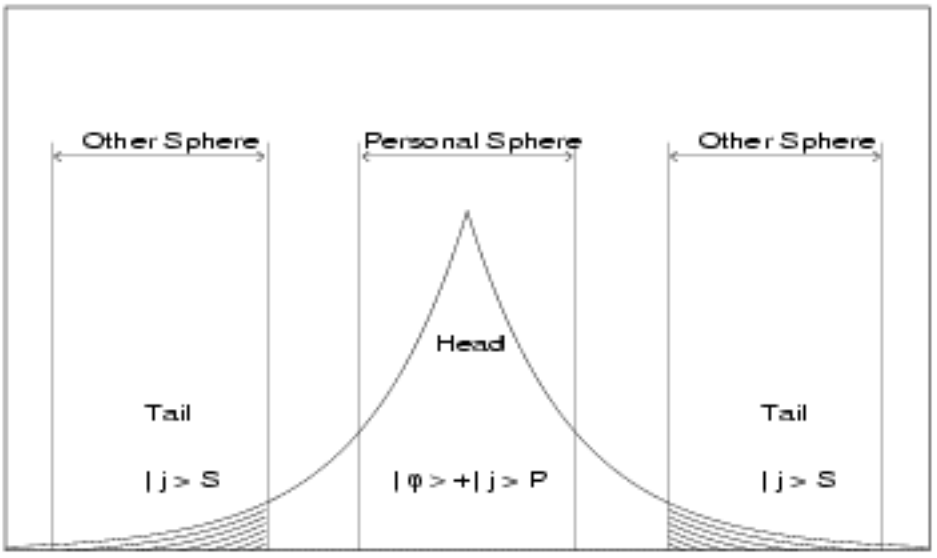

Figure 1.4: A MTO centred at R with its tails inside other spheres and its head in its personal sphere. The MTO is shown schematically only by its envelope.

$$\| \psi_R) \implies \begin{pmatrix} \psi_{L_1}(r-R) \\ \psi_{L_2}(r-R) \\ \cdots \\ \psi_{L_k}(r-R) \\ \cdots \end{pmatrix} = \begin{pmatrix} \phi_{L_1}(r_R)\, Y_{L_1}(\hat{r}_R) \\ \phi_{L_2}(r_R)\, Y_{L_2}(\hat{r}_R) \\ \cdots \\ \phi_{L_k}(r_R)\, Y_{L_k}(\hat{r}_R) \\ \cdots \end{pmatrix}$$

$$\implies \text{functions } \psi_L(r-R) \text{ are defined in all space}$$

$$| \psi_R) \implies \begin{pmatrix} \phi_{L_1}(r_R)\, Y_{L_1}(\hat{r}_R) \\ \phi_{L_2}(r_R)\, Y_{L_2}(\hat{r}_R) \\ \cdots \\ \phi_{L_k}(r_R)\, Y_{L_k}(\hat{r}_R) \\ \cdots \end{pmatrix} \Theta(r_R)$$

$$\implies \text{functions are all zero outside their personal spheres}$$

$$\#\,\psi_R) \implies \begin{pmatrix} \phi_{L_1}(r_R)\,Y_{L_1}(\hat{r}_R) \\ \phi_{L_2}(r_R)\,Y_{L_2}(\hat{r}_R) \\ \cdots \\ \phi_{L_k}(r_R)\,Y_{L_k}(\hat{r}_R) \\ \cdots \end{pmatrix} \prod_{R'} \Big(1 - \Theta(r_{R'})\Big)$$

$$\implies \text{functions are all non-zero only in the interstitial space}$$

The expression in equation (1.15) can then be written concisely as follows :

$$\|\,\chi_R(\varepsilon)) \;=\; \mathrm{N}^{\circ}_R(\varepsilon)\;|\varphi_R(\varepsilon)) + \mathbf{P}^{\circ}_R(\varepsilon,\kappa)\;|j_R(\kappa)) \;-\; \sum_{R'} \mathbf{S}^{\circ}_{RR'}(\kappa)\,|j_{R'}(\kappa)) \;+\; \#\,n_R(\kappa)) \tag{1.16}$$

Here,

$$\mathrm{N}^{\circ}_R \;=\; \begin{pmatrix} N^{\circ}_{RL_1} & 0 & 0 \\ 0 & N^{\circ}_{RL_2} & 0 \\ 0 & 0 & \ddots \end{pmatrix} \quad \mathbf{P}^{\circ}_R \;=\; \begin{pmatrix} P^{\circ}_{RL_1} & 0 & 0 \\ 0 & P^{\circ}_{RL_2} & 0 \\ 0 & 0 & \ddots \end{pmatrix}$$

$$\text{and} \quad \mathbf{S}^{\circ}_{RR'} \;=\; \begin{pmatrix} S^{\circ}_{RL_1,RL_1} & S^{\circ}_{RL_1,RL_2} & S^{\circ}_{RL_1,RL_3} \\ S^{\circ}_{RL_2,RL_1} & S^{\circ}_{RL_2,RL_2} & S^{\circ}_{RL_2,RL_3} \\ S^{\circ}_{RL_3,RL_1} & S^{\circ}_{RL_3,RL_2} & \ddots \end{pmatrix}$$

The construction of the MTO from the Neumann function (as shown in figure 1.3) can be written as :

$$\|\,\chi_R(\varepsilon)) \;=\; \|\,n_R) + \mathrm{N}^{\circ}_R(\varepsilon)\;|\varphi_R(\varepsilon)) + \mathbf{P}^{\circ}_R(\varepsilon,\kappa)\;|j_R(\kappa)) \;-\; |n_R(\kappa))$$

The equation (1.13) can also be rewritten as :

$$\|\,\Psi(\varepsilon)) \;=\; \sum_R c^{\dagger}_R(\varepsilon)\,\|\,\chi_R(\varepsilon)) \tag{1.17}$$

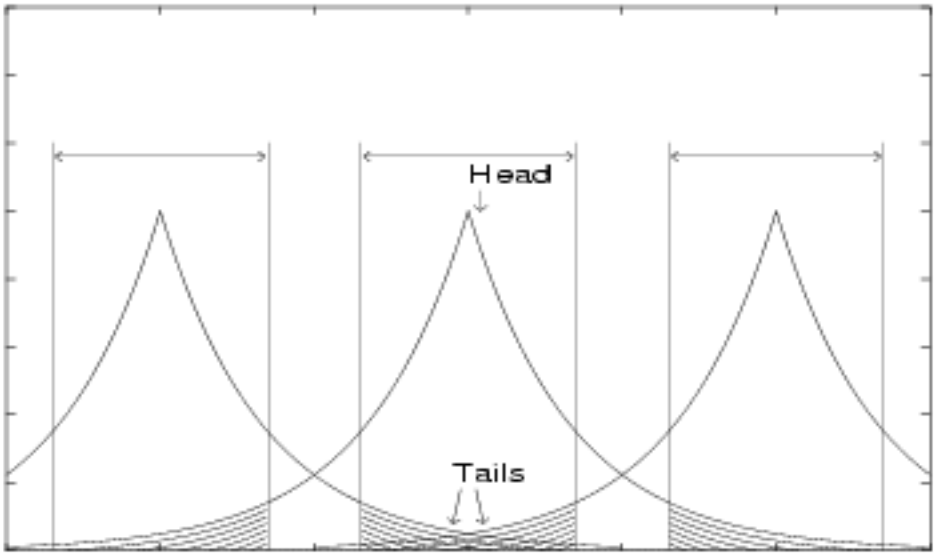

Figure 1.5: The tail cancellation theorem illustrated

where,

$$c_R(\varepsilon) \;=\; \begin{pmatrix} c_{RL_1}(\varepsilon) \\ c_{RL_2}(\varepsilon) \\ \cdots \\ c_{RL_k}(\varepsilon) \\ \cdots \end{pmatrix}$$

We shall now argue as follows : note first that if we confine ourselves to a given muffin-tin sphere centred at R_o, the potential seen by the electron in the *solid* is identical to that in the *single* muffin-tin potential at R_o. The boundary conditions (smooth,differentiable joining onto the tails) are also the same. Consequently, the solution of the Schrödinger equation of the electron in the *solid* within the muffin-tin sphere is a linear combination of the partial waves :

For $r_{R_o} \leq s_{R_o}$, i.e. within a muffin-tin sphere centred at R_o

$$|\Psi(\varepsilon)) \;=\; c^{\dagger}_{R_o}(\varepsilon)\; \mathrm{N}^{o}_{R_o}(\varepsilon)\; |\varphi_{R_o}(\epsilon)) \tag{1.18}$$

Now substituting (1.16) into (1.17), we obtain

$$
\begin{aligned}
|\Psi(\varepsilon)) \quad &= \quad c^{\dagger}_{R_o}(\varepsilon)\left[\mathrm{N}^{o}_{R_o}(\varepsilon)|\varphi_{R_o}(\varepsilon)) \;+\; \mathbf{P}^{o}_{R_o}(\varepsilon,\kappa)\;|j_{R_o}(\kappa))\right] \\
&\quad - \sum_{R\neq R_o} c^{\dagger}_{R}(\varepsilon)\;\mathrm{S}^{o}_{R_oR}(\kappa)|j_R(\kappa))
\end{aligned}
$$

Let us define $\mathrm{N}^{o}_{RR'}$ as $\mathrm{N}^{o}_{R}\;\delta_{RR'}$, $\mathbf{P}^{o}_{RR'}$ as $\mathbf{P}^{o}_{R}\;\delta_{RR'}$ and $\mathrm{S}^{o}_{RR'}=0$ if $R=R'$. We may rewrite the above as :

$$
|\Psi(\varepsilon)) \;=\; \sum_{R} c^{\dagger}_{R}(\varepsilon)\left[\mathrm{N}^{o}_{R_oR}(\varepsilon)\,|\varphi_R(\varepsilon)) \;+\; \left\{\mathbf{P}^{o}_{R_oR}(\varepsilon,\kappa) \;-\; \mathrm{S}^{o}_{R_oR}(\kappa)\right\}\;|j_R(\kappa))\right] \tag{1.19}
$$

If we now compare (1.19) with (1.18) and refer to figure (1.5), we note that the extra term $\mathbf{P}^{o}_{R_o}(\varepsilon)\;|j_{R_o}(\kappa))$ which we added to the partial wave inside its *personal* sphere (or to its head) is exactly cancelled by the contributions of the tails $\mathrm{S}^{o}_{R_oR}(\kappa)|j_R(\kappa))$ coming from all the other muffin-tin spheres :

$$
\sum_{R} c^{\dagger}_{R}(\varepsilon)\left(\mathrm{N}^{o}_{R_oR}(\varepsilon)\right)^{-1}\left[\mathbf{P}^{o}_{R_oR}(\varepsilon,\kappa) \;-\; \mathrm{S}^{o}_{R_oR}(\kappa)\right]|j_R(\kappa)) \;=\; 0
$$

$$
c^{\dagger}\;\mathrm{N}^{o}(\varepsilon)^{-1}\left[\mathbf{P}^{o}(\varepsilon,\kappa) \;-\; \mathrm{S}^{o}(\kappa)\right]=0 \tag{1.20}
$$

Here $\mathbf{A}^{o}$ is a super-matrix $A_{RL,R'L'}$, i.e. a matrix in R,R' labels, each component of which is itself a matrix labelled by L,L'.

This is true for *every* muffin-tin centred at *any* R_0, so (1.20) is a set of linear equations in the unknowns $\{c_{RL}(\varepsilon)\}$. A complete solution of these equations will give us the wave-functions through the equation (1.13). The condition for such solutions to exist is :

$$
\det\Big|\;\mathbf{P}^{o}(\varepsilon,\kappa) \;-\; \mathrm{S}^{o}(\kappa)\;\Big| \;=\; 0 \tag{1.21}
$$

This is the **KKR** Secular **E**quation which provides an equation for determination of the eigenvalues ε.

1.4.3 Energy linearization and the linear muffin-tin orbitals (LMTO)

The KKR secular equation is an implicit equation for ε. We have no *a priori* idea how many roots we expect, nor whether all roots are physically permissible. The equation is not of the eigenproblem type, so that we have no proof of the reality of the roots. Further, the implicit equation is computationally expensive and the full KKR is difficult to implement for solids with many atoms per unit cell. It is therefore desirable to bypass this energy dependence. Andersen *et al* 1987 devised a clever way of achieving just this.

The first step towards linearizing the KKR is to examine the energy dependence of the structure matrix $S^{\kappa}_{RR'}(\kappa)$. This energy dependence is inessential if the sphere packing is close. The typical wavelength of the partial waves or the muffin-tin orbitals is of the order $2\pi/\kappa$. If this is much larger than the distance between neighbouring muffin-tin spheres, then the structure matrix has a very weak energy dependence. We choose κ to be energy independent. In the interstitial region the potential is almost flat and the kinetic energy of the electrons is very small. In most of the LMTO methods we take $\kappa = 0$, although non-zero and multiple κ calculations are also available these days. In the $\kappa = 0$ methods we have :

$$\begin{aligned} \lim_{\kappa \to 0} \; j_\ell(\kappa r) &= \frac{(r/w)^\ell}{2(2\ell+1)} \\ \lim_{\kappa \to 0} \; n_\ell(\kappa r) &= \frac{1}{(r/w)^{\ell+1}} \end{aligned}$$

The next step is to note that the energy dependent solution of the Schödinger equation inside a muffin-tin sphere can be expanded as a Taylor series about some energy E^{ν}_{RL} in our range of interest :

$$\varphi_{RL}(r_R, \epsilon) \;=\; \varphi_{RL}(r_R, \varepsilon^{\nu}_{RL}) + (\varepsilon \;-\; \varepsilon^{\nu}_{RL})\, \dot{\varphi}_{RL}(r_R, \varepsilon^{\nu}_{RL}) \;+\; O\left((\varepsilon \;-\; \varepsilon^{\nu}_{RL})^2\right)$$

In our concise notation :

$$|\varphi(\varepsilon)) \;=\; |\varphi(E_\nu)) \;+\; \Delta(\varepsilon - E_\nu)\, |\dot{\varphi}(E_\nu)) \;+\; O\left((\varepsilon \;-\; \varepsilon^{\nu}_{RL})^2\right)$$

Here $\dot{\varphi}_{RL}(r_R, \varepsilon) \;=\; \partial \varphi_{RL}(r_R, \varepsilon)/\partial \varepsilon$ and the super-matrix $\Delta(\varepsilon - E_\nu)$ has elements $(\varepsilon - E_{\nu,RL})\, \delta_{RR'} \delta_{LL'}$.

In what follows, if we do not explicitly write energy dependence in a function, it will mean the function evaluated at one of the ε^{ν}_{RL}. Consider the two functions :

$$\begin{aligned} |\phi(\varepsilon)) &= \mathrm{N}^{\alpha}(\varepsilon)\,(\mathrm{N}^{\alpha})^{-1}\ |\varphi(\varepsilon)) \\ |\dot{\phi}(\varepsilon)) &= \mathrm{N}^{\alpha}(\varepsilon)\,(\mathrm{N}^{\alpha})^{-1}\ |\dot{\varphi}(\varepsilon)) + \dot{\mathrm{N}}^{\alpha}(\varepsilon)\,(\mathrm{N}^{\alpha})^{-1}\ |\varphi(\varepsilon)) \end{aligned}$$

If we define

$$\mathrm{o} \;=\; \dot{\mathrm{N}}^{\alpha}\ (\mathrm{N}^{\alpha})^{-1}$$

we note that o is a completely diagonal super-matrix and at $\varepsilon = \varepsilon^{\nu}_{RL}$ we have :

$$|\phi) \;=\; |\varphi) \qquad \text{and} \qquad |\dot{\phi}) \;=\; |\dot{\varphi}) + \mathrm{o}\,|\phi_R)$$

In the KKR method we had built up the muffin-tin orbitals by starting from a Neumann function and replacing its *head* by a partial wave such that it is smoothly and differentiably joined with the *tail* part on the muffin-tin sphere surface. Andersen's idea was to build up linearized muffin-tin orbitals by again taking a Neumann function at a fixed value of κ (say, $\kappa = 0$) and replacing its *head* by a linear combination of the functions $|\phi_R)$ and $|\dot{\phi}_R)$. In addition, the tails of the LMTO in the other spheres is also replaced by $|\dot{\phi}_{R'})$ associated with these spheres centred at R

$$\begin{aligned} \|\,\chi_R) &= \|\,n_R) \;+\; |\phi_R) + \sum_{R'} \mathrm{h}_{RR'}\,|\dot{\phi}_{R'}) - |n_R) \\ &= |\phi_R) \;+\; \sum_{R'} \mathrm{h}_{RR'}\,|\dot{\phi}_{R'}) \;+\; \sharp\, n_R) \\ &= \sum_{R'} \Big\{\, \mathbf{\Pi}_{RR'}|\varphi_{R'}) \;+\; \mathrm{h}_{RR'}\,|\dot{\varphi}_{R'})\Big\} \;+\; \sharp\, n_R) \end{aligned}$$

In our concise notation,

$$\|\,\chi) \;=\; \mathbf{\Pi}\,|\varphi) \;+\; \mathrm{h}\,|\dot{\varphi}) \;+\; \sharp\, n)$$

where

$$\mathbf{\Pi} \;=\; \mathbf{I} \;+\; \mathrm{h}\;\mathrm{o} \tag{1.22}$$

Since $|\varphi(\varepsilon)\rangle$ are solutions of the Schrödinger equation within the muffin-tin spheres, taking energy derivative of the equation and putting $\varepsilon = \varepsilon^{\nu}_{RL}$ we get :

$$\begin{aligned}(H \;-\; \varepsilon^{\nu}_{R})\,|\varphi_{R}\rangle &= 0\\ (H \;-\; \varepsilon^{\nu}_{R})\,|\dot{\varphi}_{R}\rangle &= |\varphi_{R}\rangle\end{aligned}$$

Let us again introduce the following notation :

$$\langle\,\phi\,|\,\psi\,\rangle \;=\; \psi\cdot\phi^{\dagger} \;=\; \mathbf{A}$$

where

$$A_{RL,R'L'} \;=\; \delta_{LL'}\int_{0}^{s_R} dr\; r^{2}\,\phi^{*}_{RL}(r_{R})\;\psi_{R'L'}(r_{R})$$

Using this notation, we get

$$\begin{aligned}\langle\,\phi\,|\,\phi\,\rangle &= \mathbf{I} \;\;;\;\; \langle\,\phi\,|\,\dot{\phi}\,\rangle &&= 0\\ \langle\,\dot{\varphi}\,|\,\dot{\varphi}\,\rangle &= \mathrm{p} \;\;;\;\; \langle\,\dot{\phi}\,|\,\dot{\phi}\,\rangle &&= (\mathrm{p}+\mathrm{o}^{2})\end{aligned}$$

We can now calculate the overlap matrix and the Hamiltonian representation in the LMTO basis :

$$\begin{aligned}\mathbf{O} &= \langle\,\chi\;\|\;\chi\,\rangle\\ &= \mathbf{\Pi}^{\dagger}\,\mathbf{\Pi} \;+\; \mathrm{h}^{\dagger}\,\mathrm{p}\,\mathrm{h} \;+\; \langle n\,\#\,n\rangle\end{aligned}$$

$$\begin{aligned} \mathbf{H} &= \langle\, \chi \,\|\, H \,\|\, \chi \,\rangle \\ &= \mathbf{\Pi}^{\dagger}\, \mathrm{h} \;+\; \mathbf{\Pi}^{\dagger}\, \varepsilon^{\nu}\, \mathbf{\Pi} \;+\; \mathrm{h}^{\dagger}\, \varepsilon^{\nu}\, \mathrm{p}\, \mathrm{h} \;+\; \langle n \,\#\, H \,\#\, n \rangle \end{aligned} \tag{1.23}$$

The basis we have chosen is not orthogonal. Let us change the basis to a nearly orthogonal set labelled by γ :

$$\|\, \chi^{\gamma} \rangle \;=\; \mathbf{\Pi}^{-1} \;\|\, \chi \rangle$$

In this basis :

$$\mathbf{O}^{\gamma} \;=\; \mathbf{I} \;+\; \mathrm{h}^{\gamma}\, \mathrm{p}\, \mathrm{h}^{\gamma} \;+\; \langle n \,\#\, n \rangle$$

$$\mathbf{H}^{\gamma} \;=\; \varepsilon^{\nu} \;+\; \mathrm{h}^{\gamma} \;+\; \mathrm{h}^{\gamma}\, \varepsilon^{\nu}\, \mathrm{p}\, \mathrm{h} \;+\; \langle n \,\#\, H \,\#\, n \rangle \tag{1.24}$$

where

$$\mathrm{h}^{\gamma} \;=\; \mathrm{h}\, (\mathbf{I} \;+\; \mathrm{h}\, \mathrm{o})^{-1} \tag{1.25}$$

If we neglect terms of the order of p and o^2, an approximation which is called in the LMTO literature as "the second order approximation", then in this nearly orthogonal representation

$$\begin{aligned} \mathbf{O}^{(2)} &= \mathbf{I} \\ \mathbf{H}^{(2)} &= \mathbf{E}_{\nu} + \mathrm{h} \;-\; \mathrm{h}\, \mathrm{o}\, \mathrm{h} \end{aligned} \tag{1.26}$$

The secular equation follows directly from a variational treatment of the Hamiltonian representation as in any *fixed* basis set method :

$$\left| \varepsilon \mathbf{I} \; - \; \mathbf{H} \right| \; = \; 0 \tag{1.27}$$

If we now start from the KKR secular equation (1.20) and expand the potential term about the reference energies :

$$\mathbf{P}^{\circ}(\varepsilon) \; = \; \mathbf{P}^{\circ} \; + \; (\varepsilon \mathbf{I} - \varepsilon^{\nu}) \; \dot{\mathbf{P}}^{\circ}$$

Since the super-matrix $\dot{\mathbf{P}}$ is totally diagonal, we may define the matrix $\dot{\mathbf{P}}^{\circ \; 1/2}$ as the totally diagonal super-matrix with diagonal matrix elements $\dot{P}^{1/2}_{RL}$. Substituting the expansion in (1.20) we get :

$$\det\left[\mathbf{P}^{\circ \; 1/2} \right] \; \det \left| \mathbf{P}^{\circ} \dot{\mathbf{P}}^{\circ \; -1} \; + \; \varepsilon \mathbf{I} \; - \; \varepsilon^{\nu} \; - \; \dot{\mathbf{P}}^{\circ^{-1/2}} \; \mathbf{S}^{\circ} \; \dot{\mathbf{P}}^{\circ^{-1/2}} \right\| \; \det\left[\mathbf{P}^{\circ 1/2} \right] \; = \; 0$$

$$\Longrightarrow$$

$$\det \left| \mathbf{P}^{\circ} \dot{\mathbf{P}}^{\circ \; -1} \; + \; \varepsilon \mathbf{I} \; - \; \mathbf{E}_{\nu} \; - \; \dot{\mathbf{P}}^{\circ \; -1/2} \; \mathbf{S}^{\circ} \; \dot{\mathbf{P}}^{\circ \; -1/2} \right| \; = \; 0 \tag{1.28}$$

$$\text{if} \quad \det\left[\mathbf{P}^{\circ \; 1/2} \right] \neq 0$$

If we define the *potential parameters* as :

$$\mathbf{C}^{\nu} \; = \; -\mathbf{P}^{\circ} \; \dot{\mathbf{P}}^{\circ \; -1} \qquad \text{and} \qquad \mathbf{\Delta} \; = \; \dot{\mathbf{P}}^{\circ \; -1} \tag{1.29}$$

then, comparing (1.28) with (1.27) we note that :

$$\mathbf{H}^{(1)} \; = \; \mathbf{C} \; + \; \mathbf{\Delta}^{1/2} \; \mathbf{S} \; \mathbf{\Delta}^{1/2}$$

In expanded notation :

$$\mathrm{H}^{(1)}_{RL,R'L'} \; = \; \mathrm{C}_{RL} \; \delta_{RR'} \delta_{LL'} \; + \; \Delta^{1/2}_{RL} \; \mathrm{S}^{\circ}_{RL,R'L'} \; \Delta^{1/2}_{R'L'} \tag{1.30}$$

1.4.4 The screened or tight-binding KKR formalism

One of the difficulties with the KKR method (or the linearized version of it), described in the previous sections, is that any attempt to develop a real-space technique for the solution of the secular equation is hampered by the fact that the structure matrix described above, called *canonical* in the literature, is long-ranged. For example, if we choose our z-axis along the direction of $R - R'$ then for $\kappa = 0$ and $d = |R - R'|$

$$S^{\alpha}_{ss\sigma} \sim d^{-1} \quad ; \quad S^{\alpha}_{sp\sigma} \sim d^{-2} \quad ; \quad S^{\alpha}_{pp(\sigma/\pi)} \sim d^{-3}$$
$$S^{\alpha}_{sd\sigma} \sim d^{-3} \quad ; \quad S^{\alpha}_{pd(\sigma/\pi)} \sim d^{-4} \quad ; \quad S^{\alpha}_{dd(\sigma/\pi/\delta)} \sim d^{-5}$$

Different methodologies have been proposed to obtain a new representation in which the structure matrix is short-ranged or tight-binding like. We shall follow the proposition by Andersen *et al* (Andersen *et al* 1987). The method is basically a change of basis from the canonical MTOs to the so-called *screened* MTOs. Construction of the MTOs begins with a choice of an *envelope* function, whose *head* is then replaced by an augmentation function. In the canonical formalism ,described above, the envelope function in all the other muffin-tin spheres (other than its *personal* one) is replaced by its own one-centre expansion in that sphere. We require the envelope to be a solution only in the interstitial region and hence chose it to a Neumann function. Our new choice of the envelope function will be

$$\| n^{\alpha}_{R}(\kappa r_{R})\rangle \;=\; |n_{R}(\kappa r_{R})\rangle \;-\; \sum_{R'} \mathrm{S}^{\alpha}_{RR'}\; |j^{\alpha}_{R'}(\kappa r_{R'}) \;+\; \#\, n_{R}(\kappa r_{R})\rangle$$

In its *personal sphere* the modified envelope has an extra part coming from the possible diagonal contribution from S^{α}_{RR}. In the other spheres the envelope is now different from the one-centre expansion of the Neumann function centred at R. We define,

$$|j^{\alpha}_{R}(\kappa r_{R})\rangle \;=\; |j_{R}(\kappa r_{R})\rangle \;-\; a_{R}|n_{R}(\kappa r_{R})\rangle$$

The *screening functions* are diagonal in both R and L, so we can still talk about the *personal sphere* of the modified Bessel functions. The modified Bessel's functions are ill-behaved in their *personal* spheres. We now adjust our new structure matrices such that the new envelopes are linear combinations of the unscreened ones :

We shall revert to our concise notation :

$$\begin{aligned} \| n^{\alpha}(\kappa)) &= |n) - \mathbf{S}^{\alpha}(\kappa)|j) + \mathbf{S}^{\alpha}(\kappa)\, a\, |n) \\ &= (\mathbf{I} + \mathbf{S}^{\alpha}(\kappa)\, a) \Big\{ |n) - (\mathbf{I} + \mathbf{S}^{\alpha}(\kappa)\, a)^{-1}\ \mathbf{S}^{\alpha}(\kappa)|j) i \Big\} \\ &= (\mathbf{I} + \mathbf{S}^{\alpha}(\kappa)\, a) \,\| n) \end{aligned}$$

only if

$$(\mathbf{I} + \mathbf{S}^{\alpha}(\kappa)\, a)\ \mathbf{S}^{\alpha}(\kappa) = \mathbf{S}^{\sigma}(\kappa)$$

or,

$$(\mathbf{S}^{\sigma}(\kappa))^{-1} = (\mathbf{S}^{\alpha}(\kappa))^{-1} + a \tag{1.31}$$

We now build the *screened* MTO basis, as before, by replacing the head of the envelope by a combination of the partial wave in that sphere and a modified Bessel function centred at that sphere :

$$\| \chi^{\alpha}) = \mathbf{N}^{\alpha}(\varepsilon)|\nu\varphi(\varepsilon)) + \mathbf{P}^{\alpha}(\varepsilon,\kappa)|j^{\alpha}(\kappa) - \mathbf{S}^{\alpha}(\kappa)|j^{\alpha}(\kappa)) + \sharp\, n_R)$$

The tail cancellation theorem now yields a secular equation :

$$c^{\dagger}\, \mathbf{N}^{\alpha}(\varepsilon)^{-1} \Big[\mathbf{P}^{\alpha}(\varepsilon,\kappa) - \mathbf{S}^{\alpha}(\kappa) \Big] = 0 \tag{1.32}$$

The two secular equations (1.20) and (1.32) must give identical solutions, since all we have done is to change the basis of representation. Let us impose the following :

$$\mathbf{P}^{\sigma}(\varepsilon,\kappa)\ (\mathbf{P}^{\alpha}(\varepsilon,\kappa))^{-1} = \mathbf{N}^{\sigma}(\varepsilon)\ (\mathbf{N}^{\alpha}(\varepsilon))^{-1}$$

$$(\mathbf{P}^{\alpha}(\varepsilon,\kappa))^{-1} = (\mathbf{P}^{\sigma}(\varepsilon,\kappa))^{-1} - a \tag{1.33}$$

Since $\det \left| \mathbf{P}^{\alpha}(\varepsilon,\kappa) - \mathrm{S}^{\alpha}(\kappa) \right| = 0$, the following equations are consistent :

$$\alpha \left(\mathbf{P}^{0}(\varepsilon,\kappa) - \mathrm{S}^{\alpha}(\kappa) \right) = 0$$

We now proceed as follows :

$$\mathbf{I} - \alpha \mathbf{P}^{\alpha} = \mathbf{I} + \mathrm{S}^{\alpha} \implies \mathbf{P}^{\alpha} \left((\mathbf{P}^{\alpha})^{-1} - \alpha \right) = \mathrm{S}^{\alpha} \left((\mathrm{S}^{\alpha})^{-1} + \alpha \right)$$

$$\implies \mathbf{P}^{\alpha} \, (\mathbf{P}^{\alpha})^{-1} = \mathrm{S}^{\alpha} \, (\mathrm{S}^{\alpha})^{-1} \implies \mathbf{P}^{\alpha} \, (\mathbf{P}^{\alpha})^{-1} \, \mathrm{S}^{\alpha} = \mathrm{S}^{\alpha}$$

We may now start from the canonical secular equation :

$$\begin{aligned}
& c^{\dagger} \, \mathrm{N}^{\alpha -1} \left[\mathbf{P}^{\alpha} - \mathrm{S}^{\alpha} \right] = 0 \\
\implies & c^{\dagger} \, \mathrm{N}^{\alpha -1} \, \mathrm{N}^{\alpha} \, \mathrm{N}^{\alpha -1} \left[\mathbf{P}^{\alpha} - \mathrm{S}^{\alpha} \right] = 0 \\
\implies & c^{\dagger} \, \mathrm{N}^{\alpha -1} \, \mathbf{P}^{\alpha} \, \mathbf{P}^{\alpha -1} \left[\mathbf{P}^{\alpha} - \mathrm{S}^{\alpha} \right] = 0 \\
\implies & c^{\dagger} \mathrm{N}^{\alpha -1} \left[\mathbf{P}^{\alpha} - \mathbf{P}^{\alpha} \, \mathbf{P}^{\alpha -1} \mathrm{S}^{\alpha} \right] = 0 \\
\implies & c^{\dagger} \mathrm{N}^{\alpha -1} \left[\mathbf{P}^{\alpha} - \mathrm{S}^{\alpha} \right] = 0
\end{aligned}$$

The two secular equations are thus identical. The two equations (1.31) and (1.33) then describe the transformations of the structure matrix and the potential function.

1.4.5 The tight-binding linear muffin-tin orbitals method : TB-LMTO

In this subsection, we shall discuss the linear muffin-tin orbitals (LMTO) method which not only establishes connection with both LCAO and KKR-ASA methods, but also combines the desirable features of both. Here basically one derives an energy independent basis set $\chi_{R\ell}(r)$ from the energy dependent partial waves $\phi_{R\ell}(\varepsilon, r)$ in the form of MTOs $\chi_{R\ell}(\varepsilon, r)$, and then comes out with a fast, efficient and reasonably accurate prescription for computing one-electron energies and wave-functions for all the elements in periodic table.

The KKR method essentially leads to the solutions of the secular equations of the type which can be recast in a general form M(ε) c(ε)=0, where the secular matrix M(ε) has a non-linear energy dependence. And the crux of the problem lies in finding out the roots etc. By invoking ASA, the energy dependence of the structure matrix has been removed. The remaining energy dependence now occurs only along the diagonal of the KKR-ASA matrix where it enters through the radial logarithmic derivative (or equivalently the potential function $P_{Rl}(\varepsilon)$) evaluated at atomic spheres. It is always desirable to somehow bypass this energy dependence in the KKR method, so that the entire band structure problem can be simplified. Andersen and Jepsen 1984 expressed the energy dependent solution $\phi_{Rl}(\varepsilon, r)$ of the Schrödinger equation within a sphere in terms of a well converged Taylor series about some arbitrarily chosen energy $\varepsilon = E_\nu$ at the centre of interest

$$\phi_{Rl}(\varepsilon, r_R) = \varphi_{Rl}(r_R) + (\varepsilon - E_\nu)\, \dot{\varphi}_{Rl}(r_R) + \mathbf{O}(\varepsilon - E_\nu)^2 \tag{1.34}$$

where $\varphi_{Rl}(r) \equiv \phi(E_\nu, r)$ and $\dot{\varphi}_{Rl}(r) \equiv \partial\phi(\varepsilon, r)/\partial\varepsilon \mid_{\varepsilon=\varepsilon_\nu}$ are the solutions of the Schrödinger equation and its energy derivative

$$\begin{aligned} (-\nabla^2 + V - E_\nu)\, \varphi(r) &= 0 \\ (-\nabla^2 + V - E_\nu)\, \dot{\varphi}(r) &= \varphi(r) \end{aligned}$$

Truncating the Taylor series (Equation (1.34)) after the term linear in energy, one gets the so-called linear basis set which describes fairly well the change of the radial wave function throughout the atomic sphere (r$\leq$s). The errors involved in such a ϕ-truncation, which is second order in $\varepsilon - E_\nu$, merely gives rise to fourth order errors for the energy bands, and these are usually small over an energy range of $\sim$ 2 Ryd. It was in fact demonstrated by Andersen 1984 that the term $\mathbf{O}\ (\varepsilon - E_\nu)^2 \simeq \frac{1}{2}(\varepsilon - E_\nu)^2 \ddot{\varphi}(r)$ is two to three orders of magnitude smaller than $\varphi(r)$. At this point it is worth specifying the normalizations of φ and $\dot{\varphi}$. The partial waves $\phi_{Rl}(\varepsilon, r)$ are assumed to be normalized to unity in its sphere, i.e.

$$\langle \varphi^{\cdot}_{Rl} \mid \varphi^{\cdot}_{Rl} \rangle = \int_0^{sR} \left[\phi^{\cdot}_{Rl}(\varepsilon, r)\right]^2\ r^2 dr = 1$$

The superscript γ is purposely inserted here to imply that the radial solutions of the Schröidinger equation are normalized as above, and also the radial solution and its energy derivatives are orthogonal to each other within the sphere i.e.

$$\langle \varphi^{\gamma}_{\pi l} \mid \dot{\varphi}^{\gamma}_{\pi l} \rangle = \int_0^{s_\pi} \left[\phi^{\gamma}_{\pi l}(\varepsilon, r) \dot{\phi}^{\gamma}_{\pi l}(\varepsilon, r) \right] r^2 dr = 0$$

In the general α-representation, the partial waves and its energy derivatives can be expressed, after incorporating some ε-dependent normalization $N^{\alpha}(\varepsilon)$, as

$$\begin{aligned} \phi^{\alpha}_{\pi l}(\varepsilon, r) &= \phi^{\gamma}_{\pi l}(\varepsilon, r) [N^{\alpha}_{Rl}(\varepsilon) / N^{\alpha}_{Rl}] \\ \dot{\phi}^{\alpha}_{\pi l}(\varepsilon, r) &= \dot{\phi}^{\gamma}_{\pi l}(\varepsilon, r) [N^{\alpha}_{Rl}(\varepsilon) / N^{\alpha}_{Rl}] + \phi^{\gamma}_{\pi l}(\varepsilon, r) \left[\dot{N}^{\alpha}_{Rl}(\varepsilon) / N^{\alpha}_{Rl} \right] \end{aligned}$$

Therefore, at $\varepsilon = E_{\nu}$, $\varphi^{\alpha}_{\pi l} = \varphi^{\gamma}_{\pi l} = \varphi_{\pi l}$ (say) and the *general energy derivative function* $\dot{\varphi}^{\alpha}$ becomes a linear combination of the orthogonal $\varphi - \dot{\varphi}$ pair

$$\dot{\varphi}^{\alpha}_{Rl}(r) = \dot{\varphi}^{\gamma}_{\pi l}(r) + \varphi_{\pi l}(r)\, o^{\alpha}_{Rl}$$

where $o^{\alpha}_{Rl} = \langle \varphi_{\pi l} \mid \dot{\varphi}^{\alpha}_{\pi l} \rangle$ or $\mathrm{o}^{\alpha} = \dot{\mathrm{N}}^{\alpha} (\mathrm{N}^{\alpha})^{-1} = \ddot{\mathbf{P}}^{\alpha} \left(2\dot{\mathbf{P}}^{\alpha} \right)^{-1}$ is, in general, a *non-diagonal* overlap matrix which has to be determined such that the intra-sphere linear combination of φ and $\dot{\varphi}$ can be matched in both amplitude and slope at the boundary $r = s$, with the interstitial envelope function (viz. plane waves or spherical waves). This is the so-called φ - $\dot{\varphi}$ augmentation, which is at the heart of most of the linearized methods. Using the bra-ket notation one can rewrite the above equation as

$$| \dot{\varphi}^{\alpha} \rangle = | \dot{\varphi}^{\gamma} \rangle + | \varphi \rangle \, \mathrm{o}^{\alpha} \tag{1.35}$$

where $| \varphi \rangle$, $| \dot{\varphi}^{\alpha} \rangle$ and $| \dot{\varphi}^{\gamma} \rangle$ obey the following set of relations,

$$\begin{aligned} \langle \varphi \mid \varphi \rangle &= \mathbf{I} \qquad \langle \varphi \mid \dot{\varphi}^{\gamma} \rangle = 0 \\ \langle \varphi \mid \dot{\varphi}^{\alpha} \rangle &= \mathrm{o}^{\alpha} \quad \langle \dot{\varphi}^{\alpha} \mid \dot{\varphi}^{\alpha} \rangle = \mathrm{p}^{\alpha} = \mathrm{o}^{\alpha^2} + \mathrm{p}^{\gamma} \end{aligned}$$

Here, the diagonal matrix p^{α} with elements $p^{\alpha}_{\pi l} = \langle \dot{\varphi}^{\alpha^2}_{\pi l} \rangle = -\langle \varphi_{\pi l} | \ddot{\varphi}^{\alpha}_{\pi l} \rangle$ is known as the '*small parameter*' (small but positive). The general LMTO basis can therefore be written in an energy independent form

$$\chi^{\alpha}_{RL}(r_R) = \varphi_{RL}(r_R) + \sum \dot{\varphi}^{\alpha}_{R'L'}(r_{R'})\ h^{\alpha}_{R'L',RL} + \chi^{\alpha,i}_{RL}$$

or equivalently in matrix notation,

$$|\chi^{\alpha}) = |\varphi^{\alpha}) + |\dot{\varphi}^{\alpha})\ \mathrm{h}^{\alpha} + |\chi^{\alpha})^{i} \tag{1.36}$$

where the expression for the Hermitian matrix h^{α} can be derived starting from the KKR-ASA secular Equation as

$$\begin{aligned} \mathrm{h}^{\alpha} &= -\mathbf{P}^{\alpha}(\dot{\mathbf{P}}^{\alpha})^{-1} + (\dot{\mathbf{P}}^{\alpha})^{-1/2}\ \mathbf{S}^{\alpha}\ (\dot{\mathbf{P}}^{\alpha})^{-1/2} \\ &= (\mathbf{C}^{\alpha} - \mathbf{E}_{\nu}) + \sqrt{\Delta^{\alpha}}\ \mathbf{S}^{\alpha}\ \sqrt{\Delta^{\alpha}} \end{aligned} \tag{1.37}$$

In this expression for h^{α}, the first term $\mathbf{C}^{\alpha} - \mathbf{E}_{\nu}$ is diagonal and ensures the boundary condition at 'home sphere', while the second (hopping) term $\sqrt{\Delta^{\alpha}}\ \mathbf{S}^{\alpha}\sqrt{\Delta^{\alpha}}$ is the off-diagonal term which ensures the boundary conditions at 'foreign spheres'. In the most tight-binding α-representation the structure matrix S^{α} also has a non-zero diagonal matrix element. Note that some standard potential parameters viz. the *band-centre parameter* (C^{α}) and the *band-width parameter* (Δ^{α}) have been defined here in terms of the slope and amplitude of the potential function as

$$\mathbf{C}^{\alpha} = \mathbf{E}_{\nu} - \mathbf{P}^{\alpha}\left(\dot{\mathbf{P}}^{\alpha}\right)^{-1} \qquad \text{and} \qquad \Delta^{\alpha} = \left(\dot{\mathbf{P}}^{\alpha}\right)^{-1}$$

Thus we find that within ASA, the expansion coefficients h^{α} in the expression (Equation (1.36)) for $|\chi^{\alpha})$ and the orbital overlap $o^{\alpha}_{RL} = \langle\varphi_{RL}|\dot{\varphi}^{\alpha}_{RL}\rangle$ in the expression (Equation (1.35)) for $|\dot{\varphi}^{\alpha})$ are the only two independent adjustable quantities, which can be chosen is such a way that the augmentations are continuous as well as differentiable at the sphere boundary.

The conventional LMTO method ($\kappa^2 = 0$) emanates from the replacement of the KKR-ASA secular problem by an algebraic eigenvalue problem , by taking recourse to

linearization and φ - $\dot{\varphi}$ augmentation. Of course, this replacement is only approximate in the sense that while the KKR method describes the entire spectrum, the LMTO method yields the same states and energies only over a limited energy range around E_ν, the characteristic energy of linearization. The generalized α-representation provides us with certain computational advantages, as has already been discussed. We have just seen in section 5.1 that the diagonal matrix σ^α guarantees to give $\phi^\alpha(\equiv\phi)$ the same logarithmic derivative at the sphere boundary s_R as the tail of the envelope function χ^i; and the Hermitian matrix h^α makes the augmentation of the envelope function χ^i continuous at the sphere boundary. Knowing these two quantities, and combining Equations (1.35) and (1.36), we get the LMTO basis set

$$|\chi^\alpha) = |\phi)(\mathbf{I} + o^\alpha h^\alpha) + |\dot{\phi}^\gamma)\ h^\alpha + |\chi^\alpha)^i \ \equiv\ |\phi)\ \mathbf{\Pi} + |\dot{\phi}^\gamma)\ \Omega + |\chi^\alpha)^i$$

which is in the same form as above with $\mathbf{\Pi} = \mathbf{I} + o^\alpha h^\alpha$ and $\Omega = h^\alpha$. The overlap and the Hamiltonian matrices are

$$\mathbf{O}^\alpha = (\mathbf{I} + o^\alpha h^\alpha)^\dagger(\mathbf{I} + o^\alpha h^\alpha) + h^{\alpha\dagger} p h^\alpha + {}^i\langle\chi^\alpha|\chi^\alpha)^i \tag{1.38}$$

$$\begin{aligned}\mathbf{H}^\alpha &= (\mathbf{I} + o^\alpha h^\alpha)^\dagger h^\alpha \ +\ (\mathbf{I} + o^\alpha h^\alpha)^\dagger\ E_\nu\ + \ldots \\ &\quad + h^{\alpha\dagger}\mathbf{E}_\nu p h^\alpha \ +\ \langle\chi^\alpha|[-\nabla^2 + V_{ns}(r)]|\chi^\alpha)^i\end{aligned} \tag{1.39}$$

Here, $V_{ns}(r) = V(r) - \sum_R V_R(r_R)$ is the interstitial non-spherical part of the solid state potential. By invoking ASA the interstitial integrals can be made to vanish (their contributions can be included via the "combined correction" terms), and one needs only two matrices viz σ^α and h^α in order to describe the overlap and Hamiltonian.

Now let us transform $|\chi^\alpha)^\infty$ as follows, to a new basis set $|\chi)^\infty$ which will turn out to be the orthogonal basis set, (where the superscript γ is henceforth dropped)

$$|\chi)^\infty = |\chi^\alpha)^\infty(\mathbf{I} + \mathbf{O}^\alpha h^\alpha)^{-1} = |\varphi) + |\dot{\varphi})h + |\chi)^i$$

where we have defined

$$h = h^\alpha(\mathbf{I} + o^\alpha h^\alpha)^{-1} = h^\alpha - h^\alpha o^\alpha h^\alpha + h^\alpha o^\alpha h^\alpha o^\alpha h^\alpha - \ldots \tag{1.40}$$

and

$$|\chi)^i = |\chi^\alpha)^i(\mathbf{I} + o^\alpha h^\alpha)^{-1}$$

In this new basis, the overlap and Hamiltonian expressions become simpler viz.

$$\mathbf{O} = \mathbf{I} + h\ p\ h \qquad \mathbf{H} = \mathbf{E}_\nu + h + h\ \mathbf{E}_\nu\ p\ h$$

and then one can proceed to solve the eigenvalue equation. Neglecting terms second order in h, (both involving the small parameter p), we can write

$$\mathbf{O}^{(2)} \simeq \mathbf{I} \qquad \mathbf{H}^{(2)} \simeq \mathbf{E}_\nu + h^\alpha - h^\alpha o^\alpha h^\alpha$$

Two facts clearly emerge out of the above transformation viz.

(a) The new LMTO basis set $|\chi)^\infty$ is nearly orthogonal (to first order in h) and hence can be called the orthogonal (or γ-) representation. Note that unlike the corresponding localized quantities which are represented with the superscript α, the superscripts γ in $|\chi^\gamma)^\infty$, $|\chi^\gamma)^i$, $|\varphi^\gamma)$, $|\dot{\varphi}^\gamma)$ and h^γ are usually omitted; and in the present paper all these quantities without the superscript γ will correspond to orthogonal representation. The notable features of this γ-representation is that here $|\varphi)$ and $|\dot{\varphi})$ are orthogonal i.e. $o \equiv \langle\varphi|\dot{\varphi}) = 0$.

(b) The Hermitian matrix $\mathbf{H}^{(2)}$ itself is the second order Hamiltonian. This reveals the most important feature of the new basis set $|\chi)^\infty$, viz. that under this basis the KKR-ASA secular equation becomes equivalent to the LMTO-ASA eigenvalue equation

$$(\mathbf{H}^{(2)} - \varepsilon_j^{(2)}\mathbf{I})\, c_j = 0 \tag{1.41}$$

In terms of the eigenvectors c_j, one can express the wave functions as

$$\begin{aligned} \psi_j(r) = |\chi)^\infty c_j &= [\,|\varphi) + |\dot{\varphi})h + |\chi)^i\,]c_j \\ &= [\,|\varphi) + |\dot{\varphi})h\,]\,c_j + |\chi^\alpha)^i\ b_j \end{aligned}$$

where the new vector $b_j = (\mathbf{I} + \mathrm{oh})^{-1} c_j = [1 - \mathrm{o}(\varepsilon_j i - E_\nu)]\ c_j$. In component form ψ_j looks like

$$\begin{aligned} \psi_j(r) &= \sum_{RL} \left[\{\varphi_{Rl}(r) + \dot{\varphi}_{Rl}(r)(\varepsilon_j^{(2)} - E_\nu)\} Y_L(\hat{r}_R)\ c_{RL,j} \right] + \sum_{RL} \chi_{Rl}^{\alpha,i}(r) b_{RL,j} \\ &= \sum_{RL} \phi_{Rl}(\varepsilon_j^{(2)}, r_R) Y_L(\hat{r}_R)\ c_{RL,j} + \sum_{RL} \chi_{RL}^{\alpha,i}(r) b_{RL,j} \end{aligned} \tag{1.42}$$

Thus the wave function turns out to be a one-centre expansion in terms of the radial solution $\phi_{Rl}(\varepsilon_j, r_R)$ expanded in Taylor series to first order in $(\varepsilon_j - E_\nu)$.

At this stage, a further simplification may be introduced viz. an effective two-centre TB Hamiltonian $\mathbf{H}^{(1)}$ may be defined, by truncating the series representation (Equation (1.40)) of h to first order in h^α which is given by Equation (1.37). Thus the first order (in $\varepsilon_j - E_\nu$) Hamiltonian within the ASA can be written as

$$\mathbf{H}^{(1)} \simeq \mathbf{E}_\nu + \mathrm{h}^\alpha = \mathbf{C}^\alpha + \sqrt{\mathbf{\Delta}^\alpha}\ \mathbf{S}^\alpha\ \sqrt{\mathbf{\Delta}^\alpha} \tag{1.43}$$

Since S^α is short ranged, $\mathbf{H}^{(1)}$ itself is short ranged. Also this expression for $\mathbf{H}^{(1)}$ does not contain α explicitly and hence is valid for any choice of α, provided the corresponding $\mathrm{S}^\alpha = \mathrm{S}^\circ(\mathbf{I} - \alpha \mathrm{S}^\circ)^{-1}$ has no poles. With the proper choice of α, the matrix elements of $\mathbf{H}^{(1)}$ connecting atoms beyond the second shell of neighbours in all close packed systems can be made to vanish. The resulting energy positions of the features in the density of states are, however, correct only to first order in $(\varepsilon_j - E_\nu)$, and gives reasonable energy bands in a range of half a Ryd. around E_ν. Twice this range can be covered if one uses $\mathbf{H}^{(2)}$, because then all potential functions are linear to second order in $(\varepsilon_j - E_\nu)$. Thus we now have three important observations,

(a) Within the LMTO formalism, the effect of truncating the range of the Hamiltonian h is well defined and can be controlled by truncating in the appropriate term in the power series (Equation (1.40)) in h^α. The more terms are included in this power series, the wider is the energy range around E_ν in which the eigenvalue match with the one-electron energies ε_j.

(b) Understanding the electronic structure of complicated systems like alloys or supercells is easier in terms of localized quantities. TB-LMTO therefore establishes a direct link to ideas which are based on the simpler but less accurate empirical TB methods. For structurally disordered solids for example, one can use this method in conjunction with Haydock's recursion method, or coherent potential approximation or augmented space recursion, which are discussed in other chapters of this volume.

(c) In localized basis, the computational effort in calculating Hamiltonian and overlap matrices or the full charge density, scales linearly with the number of atoms and is independent of the number of k-points. This should be compared to a typical cubic dependence on the number of atoms and a linear dependence on the number of k-points in most other methods with extended orbitals. Thus, for sufficiently large number of atoms in the unit cell, the computer time required for TB-LMTO calculation is dominated by matrix diagonalization.

Chapter 2

Electronic and magnetic properties of ordered thin films and surfaces

2.1 Introduction

Atoms on surfaces of transition metals show an enhancement in their magnetic moments. This is well established both from theory and experiment (Falicov and Morán-Lopez 1989, Wang and Freeman 1981, Ernst 2000, Wimmer *et al* 1984). Development in experimental techniques along with extremely accurate first-principles, self-consistent local spin-density (LSDA) based calculations have substantiated this fact. This enhancement is attributed to the reduced symmetry and coordination number at surfaces. This in turn results in band narrowing and hence enhancement of the paramagnetic density of state at the Fermi energy E_F (Alden *et al* 1992). Stoner-like arguments then lead to an enhancement of the local magnetic moment.

Let us discuss the Stoner's model in brief, and examine how it predicts enhancement of magnetic moments with reduction in coordination number. The electron has an intrinsic magnetic moment due to its spin, which can be either in the 'up' or 'down' state. All types of atoms with unfilled shells are magnetic. In $3d$-transition metal atoms with unfilled $3d$-orbitals, the alignment of the electron spin reduces the Coulomb energy that results from Pauli exclusion principle. This is because the average separation of the electrons will be larger in same spin state than that in opposite spin state. However in the bulk metallic form only a few of the $3d$-elements exhibit spontaneous magnetization. The reason is that the outer electrons are no longer bound to the individual ion-cores

and these free-electron form the conduction band. However electron spin alignment still results in reduction of exchange energy but at the cost of the kinetic energy (KE). The KE increases, if the electron spin aligns, because then the option of two electrons of opposite spin occupying the the same KE state is not being used. Whether or not a bulk metal will develop spontaneous magnetization, depends on this subtle interplay between the KE and exchange energy. The *Stoner criterion* for ferromagnetism depicts this interplay:

$$n(E_F)I \geq 1 \tag{2.1}$$

where, I, the exchange integral, is a measure of the Coulomb interaction between two electrons of same spin occupying the same site within the metal. $n(E_F)$ is the density of states at the Fermi energy E_F, which is a measure of increase in the total KE of the electrons if we allow a shift in the balance of the spin-up to spin-down electrons. Along the 3-d period of the periodic table from Ti to Ni, both I and $n(E_f)$ increase. Then we find, although the early 3-d transition metals do not exhibit ferromagnetism, the late transition metals Fe, Co and Ni show spontaneous magnetization in a descending order. The bandwidth in general and d-bandwidth in particular is a function of the coordination number (i.e., the number of nearest neighbours). If atoms are taken so far, that they can be considered free-atoms, their bandwidth will reduce to a delta function at the position of its atomic d-state. Again, when the atoms are brought closer together their atomic orbitals start overlapping and leads to a formation of bands. So at the surface where coordination numbers are reduced, the width of the d-band which holds the key to spontaneous magnetization, is less than that of bulk. This generally leads to increase in $n(E_F)$, if the E_F is not too close to the edge of the band. There are complications due to s-d hybridization but qualitatively this reduction in bandwidth leads to enhancement of magnetic moment of Fe, Co and Ni surfaces. But for (111) surface of Ni, local magnetization shows no enhancement. The amount also depends on the type of lattice symmetry and the number of nearest neighbours the surface is losing(Howson 1994).

Though it is in general true that band narrowing leads to enhancement of the surface magnetization, when we scanned the individual orbital components, we found not all of

them contribute to this enhancement. In fact few of the orbital (ℓ-m) resolved components were actually magnetically suppressed. In discussing surface enhancement the role of d-band is often emphasized. We found that the s and p bands also play a significant role, specially in fcc Ni (001) and hcp Co(001) surfaces , where the enhancement is feeble. The moment enhancement is largest in Fe bcc(001), among the ferromagnetic thin films, where the majority band (in bulk) is not saturated and less in Ni and Co where the majority band is almost saturated. Eriksson 1991 and Alden *et al* 1992 suggested that, less saturated the majority band in bulk, more the possibility of enhancement at the surface. For Ni thin films, almost the whole of the enhancement at the surface is due to the $d_{x^2-y^2}$ orbital, but for this state the majority band is more saturated than the three t_{2g} states in the bulk. It is therefore of importance that we carry out a detailed orbital decomposed study of magnetism at a surface before we can make statements with confidence. The anti-ferromagnetic Cr (001) thin film shows a mammoth surface enhancement in the absolute value of its surface magneization.

There have been numerous theoretical studies on thin films and surfaces, both for free standing thin films, as well as for those on substrates, using different methods. The theoretical approaches have been carried out in essentially three different approaches :

1. Single slab geometry with boundary matching Green functions (Wang and Freeman 1981, Wimmer *et al* 1981, Ma *et al* 1986, Wang and Freeman 1985, Jepsen *et al* 1982)

2. Slabs in a three-dimensional super-cell, well separated by *empty space* with charge but no atoms (Alldredge and Kleinman 1972, Kleinman and Carruthers 1972, Carruthers *et al* 1976, Schlüter *et al* 1975, Louie *et al* 1977, Louie 1978). The assumption is that the slabs separated by sufficiently wide empty spaces do not interact with one another.

3. A Green function technique making use of the two-dimensional periodicity on flat surfaces and treating the direction perpendicular to the surface by a real-space method. This was implemented within the tight-binding linearized muffin-tin orbitals method (TB-LMTO) by Skriver and Rosengaard (Skriver and Rosengaard 1991) and used to study Ni surfaces by Alden (Alden *et al* 1992).

By construction, the first and last of these approaches take proper account of broken symmetry at the surface. The second approach introduces artificial periodicity. However, it is believed that it does render accurate results when carried out to convergence (Ohnishi and Freeman 1981).

Haydock *et al* 1972 proposed a technique for the calculation of projected and integrated density of states which was based entirely on *real space* representations and therefore did not necessarily make any use of translational symmetry of any kind. This *recursion method* also yielded the energy moments of the projected density of states and most related physical quantities with *controlled accuracy*. Extensive work has been carried out to identify the errors in the recursive procedure and both analytical and numerical estimates of errors are available (Haydock 1980, Haydock and Te 1994, Ghosh *et al* 1977, Chakrabarti and Mookerjee 2002). Within this method the errors may be controlled. Earlier, we have applied this method to study the Ni thin films (Chakraborty *et al* 2003). One of the overriding advantage of the recursion method above others is the possibility of studying rough surfaces. We have developed a scheme, combining the recursion method with the TB-LMTO to study unsupported (001) thin films of transition metal elements Ni (fcc), Fe (bcc) (both planar and rough) , Cr (bcc), Co (fcc) and Co (hcp) (only planar). Other than these (001) thin films we have also studied the (110) and (111) thin film of Ni. They are surrounded by layers of *empty spheres* carrying the charge spilled out of the slabs. We have obtained the layer resolved local density of states and the local magnetic moment for these thin films. Our main interest was to see, how individual orbitals contributed to surface magnetism and how the bulk degeneracies are lifted for the surface states. All our thin films were nine layers thick surrounded by layers of empty spheres to mimic the spilled out charge. We had earlier seen that for a nine layer thick slab, the central layer local density of states is almost indistinguishable from the bulk(Chakraborty *et al* 2003).

2.2 Methodology

The recursion method can be combined with any electronic structure basis which yields a sparse representation of the Hamiltonian. The TB-LMTO based on the work by Andersen and his co-workers (Andersen 1975) is ideal in this respect as it yields both a *minimal*

basis set and an almost nearest-neighbour tight-binding like Hamiltonian.

The second order TB-LMTO Hamiltonian is written in terms of potential parameters and the screened structure matrix. It is given by,

$$\mathbf{H}^{(2)}_{\sigma} = \mathbf{E}^{\sigma}_{\nu} + \mathrm{h}^{\sigma} - \mathrm{h}^{\sigma}\ \mathrm{o}^{\sigma}\ \mathrm{h}^{\sigma}$$

$$\mathrm{h}^{\sigma} = \sum_{R_s L} \left(C^{\sigma}_{R_s L} - E^{\sigma}_{\nu R_s L} \right) \mathbf{P}_{R_s L} + \sum_{R_s L} \sum_{R'_t L'} \left(\Delta^{\sigma}_{R_s L} \right)^{1/2} S^{\beta}{}_{R_s L, R'_t L'} \left(\Delta^{\sigma}_{R'_t L'} \right)^{1/2} \mathbf{T}_{R_s L, R'_t L'} \tag{2.2}$$

- C, o and Δ are potential parameters of the TB-LMTO method. These are diagonal matrices in the angular momentum $L = (\ell, m)$, spin σ and layer s indices. In the absence of spin-orbit terms in the Hamiltonian, the representation is diagonal in the spin index. o^{-1} has the dimension of energy and is a measure of the energy window around E_{ν} around which the appreximate Hamiltonian $\mathbf{H}^{(2)}$ is reliable.

- R_s, R_t denote the positions of atomic spheres on a two-dimensional layer parallel to the surface layer. These layers are labeled by s and t.

- $\mathrm{S}^{\beta}_{R_s L, R'_t L'}$ is the TB-LMTO structure matrix in the most screened representation. This depends on the geometry of the underlying lattice. Its layer dependence describes surface relaxation.

- $\mathbf{P}_{R_s L}$ and $\mathbf{T}_{R_s L, R'_t L'}$ are the projection and transfer operators in Hilbert space $\mathbf{H}$ spanned by the TB-LMTO minimal basis $\{|R_s L\rangle\}$: $\mathbf{P}_{R_s L} = |R_s L\rangle\langle R_s L|$ and $\mathbf{T}_{R_s L, R'_t L'} = |R_s L\rangle\langle R'_t L'|$.

The recursion method uses a three term recurrence relation to change to a new basis in which the representation of the Hamiltonian is tri-diagonal:

$$\begin{aligned} |1\rangle &= |R_s L\rangle \qquad\qquad |0\rangle = 0 \\ |n+1\rangle &= \mathbf{H}^{(2)}_{\sigma}\,|n\rangle \ - \ a_n\,|n\rangle \ - \ b_n^2\,|n-1\rangle \end{aligned} \tag{2.3}$$

where, using the orthogonality of the new basis :

$$\alpha_n = \frac{\langle n|\mathbf{H}_\sigma^{(2)}|n\rangle}{\langle n|n\rangle} \qquad \beta_n^2 = \frac{\langle n|n\rangle}{\langle n-1|n-1\rangle}$$

Using the above equations and normalizing the new basis :

$$\begin{aligned} |n\} &= |n\}/[\{n|n\}]^{1/2} \quad \text{and} \\ \{n|\mathbf{H}_\sigma^{(2)}|n\} &= \alpha_n \qquad \{n-1|\mathbf{H}_\sigma^{(2)}|n\} = \beta_n \end{aligned} \tag{2.4}$$

Now,

$$G^\sigma_{R_sL,R_sL}(z) = \langle 1|\left(z\mathbf{I} - \mathbf{H}_\sigma^{(2)}\right)^{-1}|1\rangle$$

So we have to obtain the corner element of the inverse of the matrix :

$$\begin{pmatrix} z-\alpha_1 & -\beta_1 & 0 & 0 & \dots \\ -\beta_1 & z-\alpha_2 & -\beta_2 & 0 & \dots \\ 0 & -\beta_2 & z-\alpha_3 & -\beta_3 & \dots \\ \dots & \dots & \dots & \dots & \dots \end{pmatrix}$$

If $D_k(z)$ is the determinant of the matrix above with k of the rows and columns removed starting from the top and left, then :

$$D_k(z) = (z-\alpha_{k+1})\, D_{k+1}(z) - \beta_{k+1}^2\, D_{k+2}(z) \tag{2.5}$$

Now,

$$\begin{aligned} \langle 1|\left(z\mathbf{I} - \mathbf{H}_\sigma^{(2)}\right)^{-1}|1\rangle &= \frac{D_1(z)}{D_0(z)} = \frac{1}{D_0(z)/D_1(z)} \\ &= \frac{1}{z-\alpha_1 - \beta_1^2\, D_2(z)/D_1(z)} \end{aligned}$$

If we now go on applying Equation (2.5) repeatedly the diagonal element of Green function is obtained as a continued fraction :

$$G^{\sigma}_{R_sL,R_sL}(z) = \cfrac{1}{z-a_1-\cfrac{\beta_2^2}{z-a_2-\cfrac{\beta_3^2}{\ddots \cfrac{\beta_N^2}{z-a_N-T(z)}}}} \tag{2.6}$$

The continued fraction is terminated after $N = 40$ steps consistent with the error window allowed by us (Haydock and Te 1994, Chakrabarti and Mookerjee 2002) and the terminator suggested by Beer and Pettifor 1982 is used to replace the asymptotic part of the continued fraction. This terminator maintains the *Herglotz* analytic properties of the exact Green function :

- All singularities of $T(z)$ lie on the real z-axis.
- Sign of $\Im m\ T(z) =$ - Sign of $\Im m(z)$.
- $\Re e\ T(E) \sim (1/E)$ as $E \rightarrow \pm\infty$

The partial density of states, Fermi energy and energy moments are given by :

$$n^{\sigma}_{s,L}(E) = -\frac{1}{\pi}\,\Im m\ G^{\sigma}_{R_sL,R_sL}(E+i0^+)$$

$$\int_{-\infty}^{E_F} dE \left\{\frac{1}{S}\sum_{s,L,\sigma} n^{\sigma}_{s,L}(E)\right\} = n$$

$$m^{(q)}_{s,L,\sigma} = \int_{-\infty}^{E_F} dE\ n^{\sigma}_{s,L}(E)\left(E - E^{\sigma}_{vR_sL}\right)^q$$

The spin and layer resolved charge densities are given in terms of the energy moments and the solution of the Schrödinger equation within the atomic spheres :

$$\rho_s^\sigma(r) = \frac{1}{4\pi}\sum_L \Big[m^{(0)}_{s,L,\sigma}\phi^\sigma_{R_sL}(r)^2 + 2m^{(1)}_{s,L,\sigma}\phi^\sigma_{R_sL}(r)\dot{\phi}^\sigma_{R_sL}(r) + \ldots + m^{(2)}_{s,L,\sigma}\left\{\dot{\phi}^\sigma_{R_sL}(r)^2 + \phi^\sigma_{R_sL}(r)\ddot{\phi}^\sigma_{R_sL}(r)\right\}\Big] \tag{2.7}$$

The total energy per atom is expressed as :

$$E_{TOT} = \frac{1}{S}\sum_{s,L,\sigma}\int_{-\infty}^{E_F} dE\ E\ n^\sigma_{s,L}(E) + \sum_{R'}\sum_{LL'} M_{LL'}(R-R')\ Q_{RL}\ Q_{R'L'}\ldots - \frac{1}{\sqrt{4\pi}}\sum_{s,\sigma}\int_0^{r_A} d^3r\ \rho^\sigma_s(r)\left\{\frac{2Z}{r} - \epsilon_{xc}[\rho^\uparrow_s(r),\rho^\downarrow_s(r)]\right\} + E_{core} \tag{2.8}$$

S is the number of layers, $M_{LL'}(R-R')$ are the Madelung matrices given by Skriver and Rosengaard 1991 , Q_{RL} are the multi-pole moments of the surface charge densities, and these are obtained from the charges contained in the surface empty sphere layer and ϵ_{xc} is the parameterized exchange-correlation energy density. We have used the exchange energy density suggested by von Barth and Hedin 1972 for all the cases except anti-ferromagnetic Cr (001) thin film, where we have used the Vosko-Wilk-Nusair local exchange correlation potential along with Perdew-Wang non-local exchange correlation.

2.3 Results

We have studied thin films and their corresponding surfaces by decomposing information for their orbitals and comparing them with their bulk counterparts. At the surface the symmetry of the bulk is lost and orbitals of different direction starts behaving differently. Before applying our scheme on different thin films, we have cross-checked the convergence of our method for different layered thin films of (001) Ni. We found that the energy moments shows excellent convergence with the TB-LMTO supercell results. We also observed that to mimic a realistic surface (i.e., central layer of the thin film to emulate the bulk features), we should take at least seven to nine layered film. While checking the convergence, the surface enhancement were bit underestimated as we took a bigger

supercell without using the planar-symmetry. The supercell had 36 inequivalent sites, proper use of the remnant symmetry would make the supercell half (i.e., 18 sites) and will make the calculation more accurate.The details of this work was published in Chakraborty *et al* 2003.

The surface environment is different from that prevailing in bulk, and this difference has got a directional dependence. This directional dependence has a say in how the charge get redistributed amongst the different orbitals. There seem to be two competing effects which determine the way charge redistributes among the *d*-orbitals:

(i) For those orbitals whose lobes point away from the surface towards the empty spheres, there is increase in self-energy which favours depopulation

(ii) their band width decreases which should facilitate increase in population (Jepsen *et al* 1982).

Our results for layer, orbital and spin decomposed charges and magnetic moments are presented in the following subsections. Here all the calculations utilizes the planar symmetry of the thin films, where ever they are present.

2.3.1 The face centred cubic Ni (001) surface

Layer	Atomic sphere charges				Moments
	s	*p*	*d*	Total	(μ_B)
S+1	0.088	0.082	0.0405	0.211	-0.004
S	0.593	0.457	8.65	9.70	0.65
S-1	0.673	0.765	8.66	10.10	0.53
S-2	0.661	0.736	8.59	9.99	0.61
S-3	0.663	0.733	8.60	10.00	0.60
S-4	0.663	0.734	8.61	10.00	0.595

Table 2.1: Charges in the atomic spheres and magnetic moments in various layers of a nine-layer(001) Ni slab

Table 2.1 shows us the charge profile of the orbitals for different layers. We can also see how the charge and magnetic moment oscillates with layers. Figure 2.1 shows the

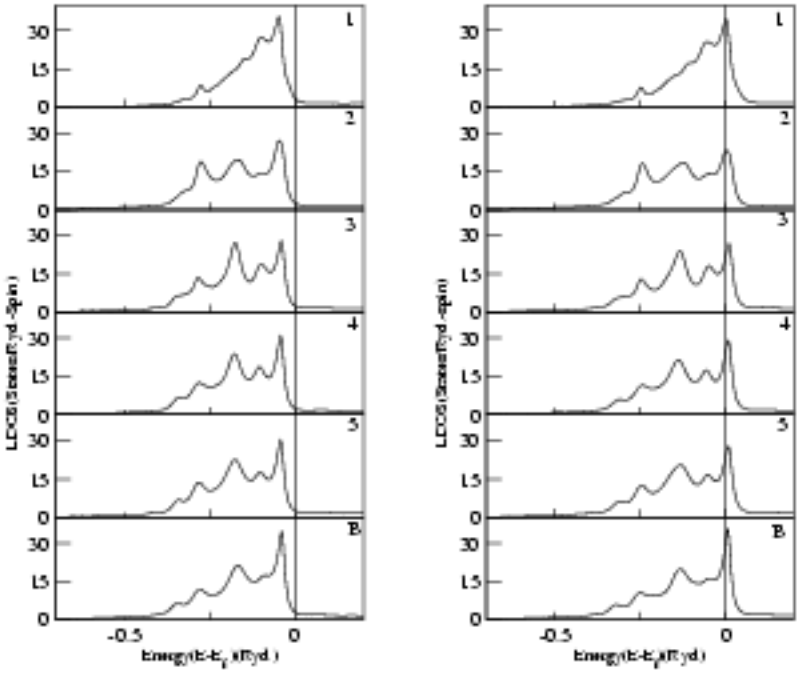

Figure 2.1: Layer resolved local density of states of a nine layer thick (001) Ni film . The majority bands are shown in the left column and the minority bands are shown in the right column. Energy is measured with respect to the Fermi Energy.

layer projected local density of states (LDOS). The surface layer shows the characteristic narrowing, while that of the central layer resembles that of the bulk. The magnetic moment of the central layer is also similar to that of the bulk. Our estimate of the enhancement of the surface magnetic moment agrees closely with the result of Alden *et al* 1992. It is slightly more than the full-potential LMTO (FP-LMTO) work of Eriksson 1991 and less than the full-potential linearized augmented plane wave (FPLAPW) of Wimmer *et al* 1984. The variation of d-charge for different layers is very small (Table 2.1). Table 2.2 shows the orbital-decomposed charge and magnetic moments for the surface layer and bulk. However, it is the manner in which the charge redistribution takes place among the five d-orbitals, that makes surface magnetization different from bulk. At the surface the d_{xz}, d_{yz} and d_{3z^2-1} orbitals have their lobes pointing perpendicular to the surface and toward the empty spheres, their LDOS become narrow and they gain charge. The

d_{xy} and $d_{x^2-y^2}$ orbitals have their lobes parallel to the surface and they lose charge. In the face-centred cubic Ni (001) surface , the second effect dominates. A similar effect at Ni(001) surface was seen by Jepsen *et al* 1982 for five layered film. It is the $d_{x^2-y^2}$ orbital which almost single handedly enhances the surface magnetic moment. The role of s and p orbitals is also significant. In bulk the s-p magnetic moment is polarized opposite to that of the d-magnetic moment and is about $\sim -0.035\ \mu_B$. At the surface though the polarization is still opposite, the magnitude decreases ~ -0.016 and facilitates enhancement.

	Surface Layer				Bulk			
Orbitals	Q ↑	Q ↓	Total Q	μ_B	Q ↑	Q ↓	Total Q	μ_B
s	0.295	0.297	0.593	-0.0019	0.34	0.347	0.688	-0.0074
p_x	0.085	0.091	0.177	-0.0056	0.122	0.132	0.254	-0.009
p_y	0.085	0.091	0.177	-0.0056	0.122	0.132	0.254	-0.009
p_z	0.051	0.053	0.104	-0.0026	0.122	0.132	0.254	-0.009
d_{xy}	0.897	0.73	1.627	0.167	0.905	0.74	1.65	0.160
d_{xz}	0.94	0.80	1.734	0.14	0.905	0.74	1.65	0.160
d_{yz}	0.94	0.80	1.734	0.14	0.905	0.74	1.65	0.160
$d_{x^2-y^2}$	0.94	0.80	1.74	0.144	0.94	0.86	1.8	0.079
d_{3z^2-1}	0.945	0.869	1.81	0.076	0.94	0.86	1.8	0.079

Table 2.2: Orbital projected Charge(Q) and magnetic moment of (001) surface and bulk of fcc Ni.

Figure 2.2 shows the m resolved LDOS for the surface d-orbitals and the e_g and t_{2g} levels for bulk Ni. The t_{2g} degeneracy has been lifted, but xz and yz orbitals are still degenerate due to the remnant planar symmetry of the (001) film. Figure 2.3 shows the magnetic enhancement(in %) for different layers. An interesting facet of this study is the steep suppression of the magnetic moment for the atoms below the surface layer. Jepsen *et al* 1982 also reported similar finding, although their suppression was bit less.

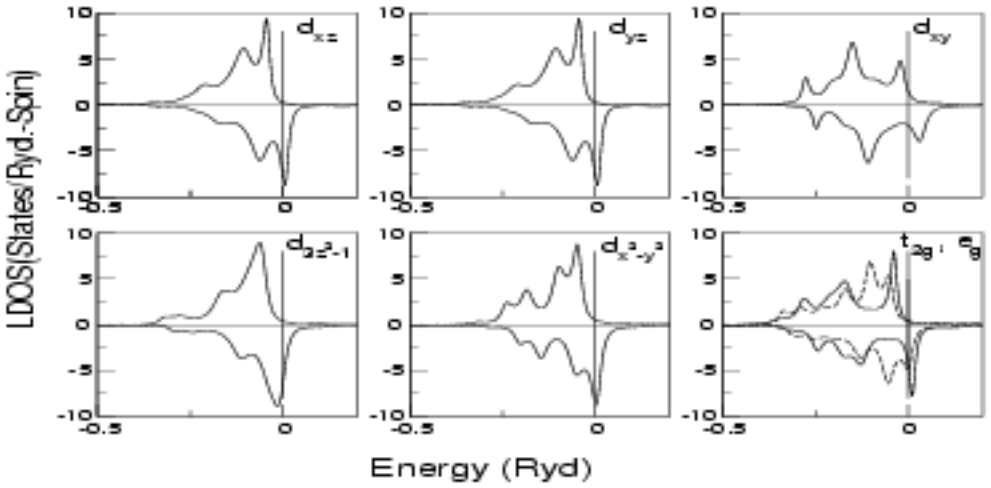

Figure 2.2: Orbital resolved LDOS for the d-states on a fcc Ni (001) surface . The right hand bottom corner panel shows the splitting of d-orbitals in bulk. Energy is measured with respect to the Fermi Energy.

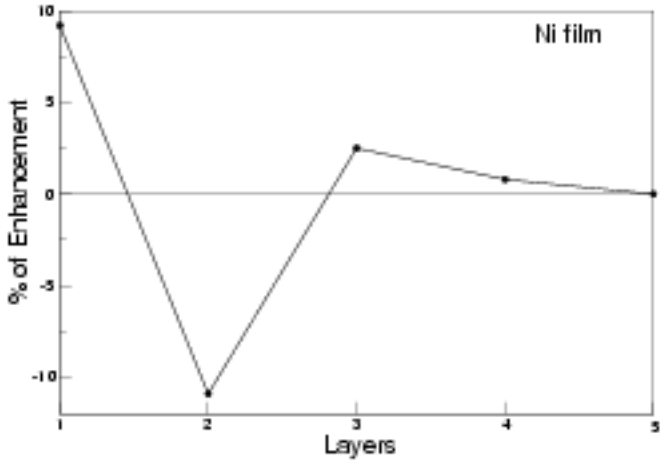

Figure 2.3: Magnetic enhancement(in %) of (001) Ni film

2.3.2 The face centred cubic Ni (110) surface

A face centred cubic (110)surface loses five of its nearest neighbour compared to four for (001) and three for (111) surface. Consequently, the surface sites for a face centred cubic

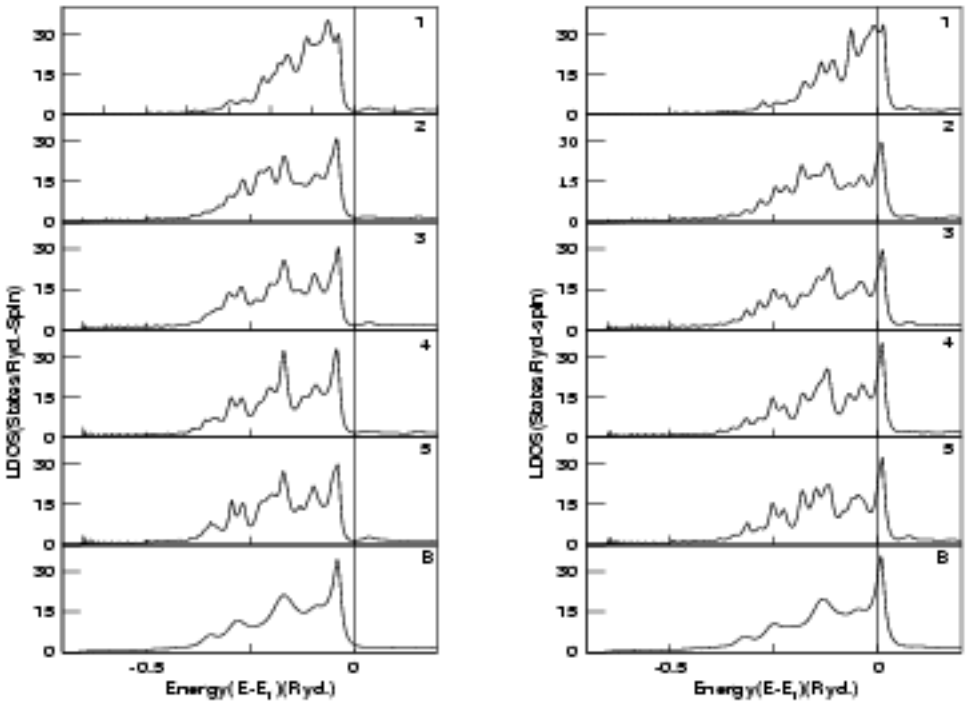

Figure 2.4: Layer resolved local density of states of a nine layer thick (110) Ni film . The majority bands are shown in the left column and the minority bands in the right. Energy is measured with respect to the Fermi Energy.

Layer	Atomic sphere charges				Moments
	s	p	d	Total	(μ_B)
S+1	0.134	0.115	0.0.054	0.304	-0.004
S	0.562	0.395	8.64	9.60	0.69
S-1	0.672	0.707	8.66	10.04	0.55
S-2	0.667	0.754	8.63	10.05	0.55
S-3	0.661	0.733	8.59	9.98	0.64
S-4	0.66	0.736	8.60	9.99	0.58

Table 2.3: Charges in the atomic spheres and magnetic moments in various layers of a nine-layer(110) Ni slab

(110) Ni loses maximum amount of charge and exhibits maximum enhancement in surface magnetization, compared to other surfaces of Ni we have studied. Here only d_{3z^2-1} has

its lobe parallel surface plane, all the the other orbitals do not stay parallel to the surface plane. Unlike the (001) surface where at least two of the orbitals were degenerate, here all the orbitals are rendered degenerate. Table-2.3 shows us the charges of different orbitals and layers. The local density of states of each layer for the majority and minority band is shown in Figure 2.4. The width of the surface states are reduced due to the surface effect and the minority surface states is significantly pushed right of E_F which results in charge loss from the minority state and hence a significant enhancement. Here the surface layer shows a magnetic enhancement of almost 19% which is almost double than that of the (001) surface. Another very interesting effect can be seen if we closely look at the layer resolved magnetic moment given in the Table-2.3, the magnetic moment of the second and third layer of the thin film is almost same and their LDOS is also similar.

	Surface Layer				Bulk			
Orbitals	Q ↑	Q ↓	Total Q	μ_B	Q ↑	Q ↓	Total Q	μ_B
s	0.281	0.280	0.561	0.0005	0.34	0.347	0.688	-0.0074
p_x	0.0466	0.0481	0.0947	-0.0015	0.122	0.132	0.254	-0.009
p_y	0.082	0.088	0.169	-0.0067	0.122	0.132	0.254	-0.009
p_z	0.063	0.068	0.131	-0.0056	0.122	0.132	0.254	-0.009
d_{xy}	0.96	0.87	1.823	0.0915	0.905	0.74	1.65	0.160
d_{xz}	0.93	0.86	1.78	0.073	0.905	0.74	1.65	0.160
d_{yz}	0.92	0.72	1.64	0.202	0.905	0.74	1.65	0.160
$d_{x^2-y^2}$	0.91	0.69	1.607	0.222	0.94	0.86	1.8	0.079
d_{3z^2-1}	0.95	0.83	1.77	0.114	0.94	0.86	1.8	0.079

Table 2.4: Orbital projected Charge(Q) and magnetic moment of (110) surface layer and bulk of fcc Ni.

The individual orbital and spin resolved charge and the corresponding magnetic moment of (110) surface and bulk Ni are given in Table-2.4. The Local density of states for each d-orbital of (110) surface is shown in Figure 2.5. Here the burden of the substantial enhancement is almost shouldered by the $d_{x^2-y^2}$ state which is mainly due to the significant depletion of charge from its minority state. This is reflected in the LDOS in Figure 2.5, which clearly shows that the minority state of $d_{x^2-y^2}$ has been pushed to the right of E_F. The d_{yz} and the d_{3z^2-1} states also contribute to the enhancement. The d_{xy} and the d_{xz} states shows reduction in their respective magnetic moment and that is mainly due to

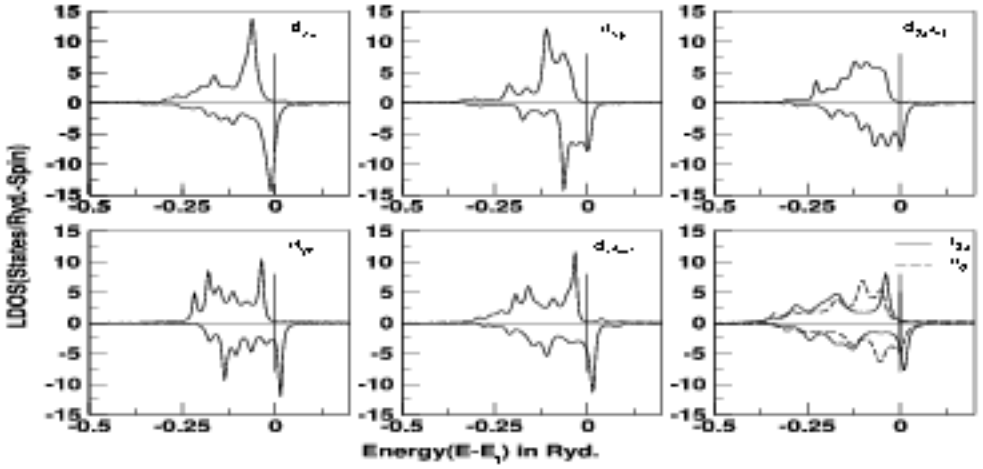

Figure 2.5: Orbital resolved LDOS for the d-states on a fcc Ni (110) surface . The right hand bottom corner panel shows the splitting of d-orbitals in bulk. Energy is measured with respect to the Fermi Energy.

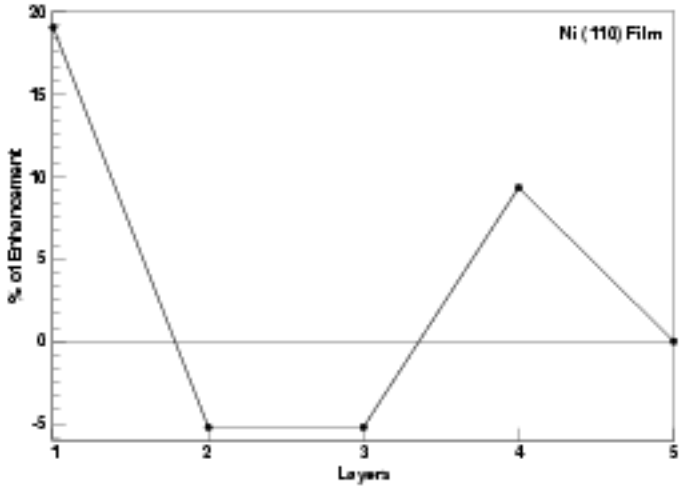

Figure 2.6: Magnetic enhancement(in %) of (110) Ni film

their minority state gaining more charge than their majority state. This is evident from their projected LDOS shown in Figure 2.5. Here also, the two effects which determine whether a surface loses or gains charges, act differently for different d-states.

The layer dependent charge and magnetic moments exhibit oscillations. The nature of these oscillations is different as compared to that of the (001) thin film of Ni. The percentage(%) variation of magnetic moment with respect to the central layer is shown in Figure 2.6.

2.3.3 The face centred cubic Ni (111) surface

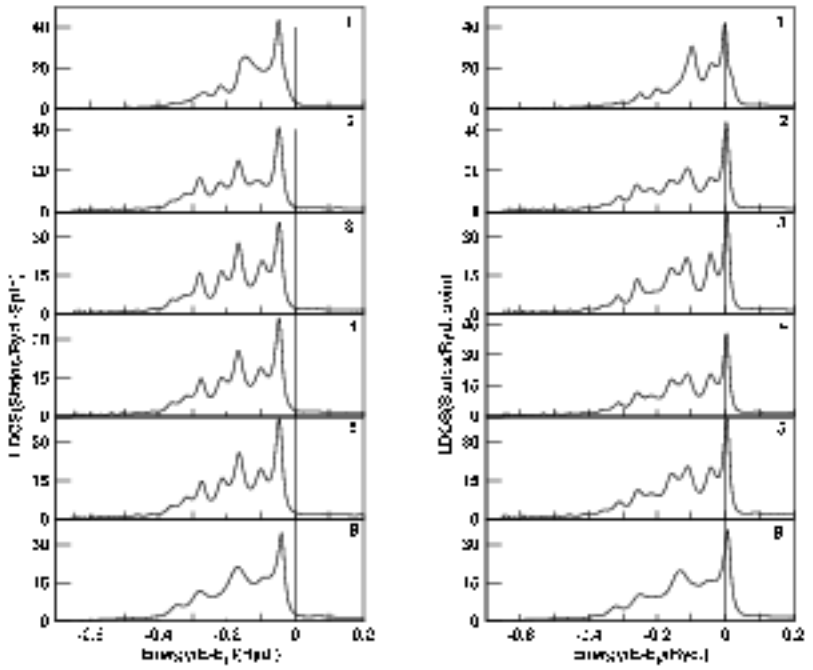

Figure 2.7: Layer resolved local density of states of a nine layer thick (111) Ni film : The majority bands are shown in the left colomn and the minority bands are shown in the right. Energy is measured with respect to the Fermi Energy.

The magnetism of the (111) surface of Ni is unique, in the sense, it does not exhibit any enhancement in surface magnetization. Table-2.5 shows the orbital dependent charge profile and the magnetic moment for different layers of the thin film. The magnetic moment of different layers hardly show any significant variation. Apart from the surface atom losing a small amount of charge, same can be said about the charges of various

Layer	Atomic sphere charges				Moments
	s	p	d	Total	(μ_B)
S+1	0.060	0.062	0.0303	0.153	-0.004
S	0.650	0.546	8.57	9.77	0.606
S-1	0.689	0.776	8.60	10.06	0.600
S-2	0.684	0.755	8.57	10.01	0.603
S-3	0.685	0.756	8.57	10.01	0.595
S-4	0.684	0.754	8.55	9.99	0.607

Table 2.5: Charges in the atomic spheres and magnetic moments in various layers of a nine-layer(111) Ni slab.

layers. The charge lost by the surface atom is entirely from the p-state. The LDOS for different layers of (111) Ni thin film and bulk Ni is shown in Figure 2.7. The surface LDOS shows the characteristic narrowing both for majority and minority states. But it is interesting to note, that there is hardly any major shift near E_F for any of the LDOS. But when we scan individual (ℓ-m) resolved components, they are not that featureless. Here none of the d-orbitals is in the (111) plane. Therefore more or less every d-component has some part of it pointing towards the vacuum.

	Surface Layer				Bulk			
Orbitals	Q ↑	Q ↓	Total Q	μ_B	Q ↑	Q ↓	Total Q	μ_B
s	0.323	0.328	0.650	-0.005	0.34	0.347	0.688	-0.0074
p_x	0.104	0.112	0.216	-0.0084	0.122	0.132	0.254	-0.009
p_y	0.105	0.113	0.218	-0.0085	0.122	0.132	0.254	-0.009
p_z	0.054	0.058	0.113	-0.0041	0.122	0.132	0.254	-0.009
d_{xy}	0.901	0.736	1.637	0.165	0.905	0.74	1.65	0.160
d_{xz}	0.947	0.843	1.79	0.104	0.905	0.74	1.65	0.160
d_{yz}	0.945	0.896	1.846	0.054	0.905	0.74	1.65	0.160
$d_{x^2-y^2}$	0.892	0.705	1.597	0.188	0.94	0.86	1.8	0.079
d_{3z^2-1}	0.91	0.789	1.7	0.121	0.94	0.86	1.8	0.079

Table 2.6: Orbital projected Charge (Q) and magnetic moment of the (111) surface layer and bulk of face centred cubic Ni.

If we see Figure 2.8, which shows the individual d-orbitals, we can see that, for the minority state of d_{xz} and d_{yz} states, there is a significant shift of the main peak towards

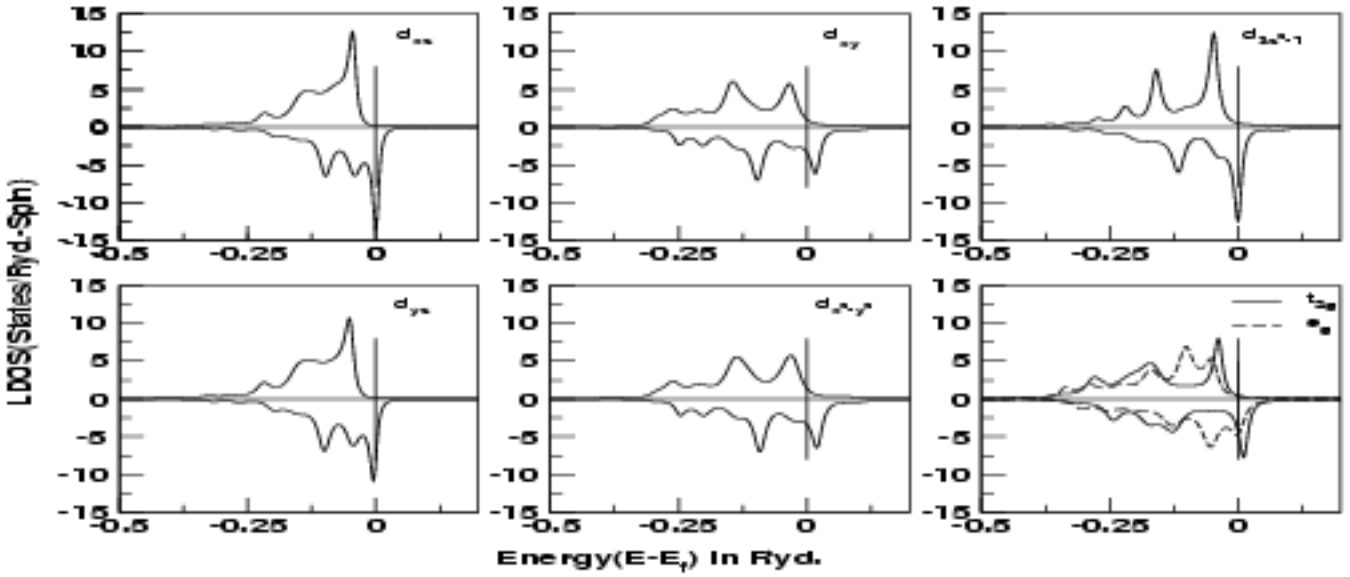

Figure 2.8: Orbital resolved LDOS for the d-states on a fcc Ni (111) surface . The right hand bottom corner panel shows the splitting of d-orbitals in bulk. Energy is measured with respect to the Fermi Energy.

left near E_F. This is aptly reflected in Table-2.6, which shows big gain in charge for the minority states of d_{xz} and d_{yz} and as a consequence the magnetic moment of these states are suppressed with respect to that of the t_{2g} states in bulk. It is due to the significant enhancement in the magnetic moment of $d_{x^2-y^2}$ and d_{3z^2-1} that the Ni(111) surface retains the bulk magnetic moment. Their minority surface states losing significant amount of charge results in such a scenario. Here also the suggestion of Eriksson 1991

and Alden *et al* 1992 does not seem to hold, because the majority e_g levels were almost saturated in bulk. The charge and magnetization of the d_{xy} state hardly shows any change. Another noticeable fact is that the combined s-p moments which were less negatively polarized in (001) surface and contributed to the surface enhancement of that surface, do not significantly help in enhancing the surface magnetization.

2.3.4 The face centred cubic Ni(001) rough surface

We have considered six different structures that may arise in a rough surface. First, we may roughen the surface layer by randomly removing atoms from it and replacing them by empty spheres carrying charge but no ion-core. The first four environments are those in which one to four of the nearest neighbours of a surface atom are missing. The fifth structure is one in which a single Ni atom sits atop the surface and the last is the top atom on a pyramidal structure sitting on the surface. The Figure 2.9 shows the local density of states (both for the majority and for the minority bands) in the six different environments.

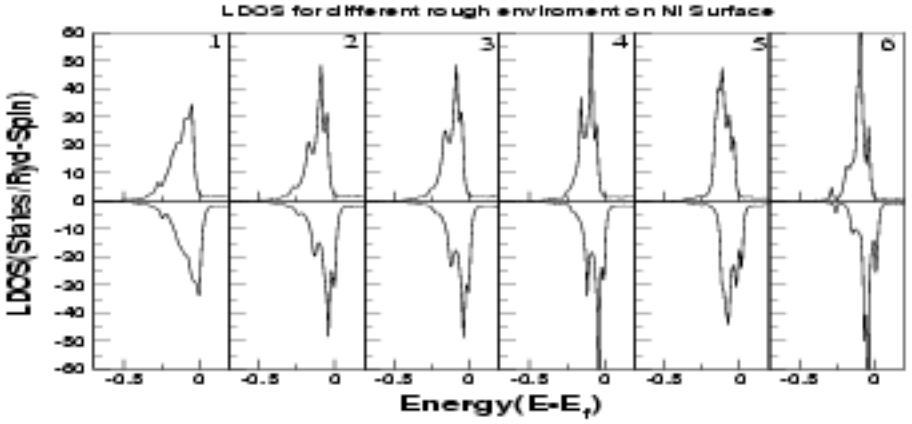

Figure 2.9: Majority and minority local density of states in the six local environments on a rough Ni (001) surface

The Table-2.7 summarizes the local magnetic moments at the six different rough environments. It is known that the local moment on Ni is fragile. In alloys, with a non-

magnetic partner, for example, Ni needs other Ni atoms in its neighbourhood to bolster its magnetic moment. If it has less than eight Ni neighbours in a face-centred cubic lattice it loses its magnetic moment completely. The same effect is seen here when we replace Ni by empty spheres from the neighbourhood of the Ni atom under study. It is also clear from the table that in a rough surface there is considerable fluctuation in the magnetic moment as we encompass the surface. In an earlier communication Huda and Mookerjee 2003 studied this fluctuation and introduced the idea of a magnetic roughness which was closely related to structural roughness of the surface.

Environment	Envir1	Envir2	Envir3	Envir4	Envir5	Envir6
Mag.mom.(μ_B)	0.56	0.46	0.355	0.25	0.56	0.53

Table 2.7: Magnetic moment of Ni atoms for different environment.

2.3.5 The body centred cubic Fe (001) surface

Layer	Atomic sphere charges				Moments
	s	*p*	*d*	Total	(μ_B)
S+1	0.154	0.115	0.052	0.322	0.054
S	0.576	0.42	6.51	7.50	2.95
S-1	0.67	0.796	6.7	8.163	2.2
S-2	0.654	0.787	6.565	8.006	2.387
S-3	0.647	0.772	6.59	8.005	2.28
S-4	0.65	0.775	6.568	8.00	2.28

Table 2.8: Charges in the atomic spheres and magnetic moments in various layers of a nine-layer slab (001) of Fe.

Table-2.8 shows us the charge profile of the orbitals for different layers of a nine layered bcc (001) Fe film. We also see that the magnetic moment oscillates as we go down the layers from the surface . There is magnetic enhancement at the surface layer, but a magnetic depression in the next lower layer, exactly as in the Ni film.

Figure 2.10 shows the layer projected LDOS. The surface LDOS exhibits the characteristic narrowing because of the lower bonding environment. Our magnetic enhancement is similar to the Green's function technique result of Alden *et al* 1992 as well as that of the

	Surface Layer				Bulk			
Orbitals	Q ↑	Q ↓	Total Q	μ_B	Q ↑	Q ↓	Total Q	μ_B
s	0.293	0.283	0.576	0.01	0.32	0.334	0.654	-0.014
p_x	0.082	0.075	0.157	0.007	0.12	0.14	0.26	-0.02
p_y	0.082	0.075	0.157	0.007	0.12	0.14	0.26	-0.02
p_z	0.055	0.050	0.105	0.005	0.12	0.14	0.26	-0.02
d_{xy}	0.92	0.49	1.41	0.43	0.85	0.50	1.35	0.35
d_{xz}	0.93	0.36	1.3	0.57	0.85	0.50	1.35	0.35
d_{yz}	0.93	0.36	1.3	0.57	0.85	0.50	1.35	0.35
$d_{x^2-y^2}$	0.955	0.30	1.25	0.66	0.94	0.31	1.25	0.63
d_{3z^2-1}	0.971	0.281	1.25	0.69	0.94	0.31	1.25	0.63

Table 2.9: Orbital projected Charge and magnetic moment of (001) surface layer and bulk of bcc Fe.

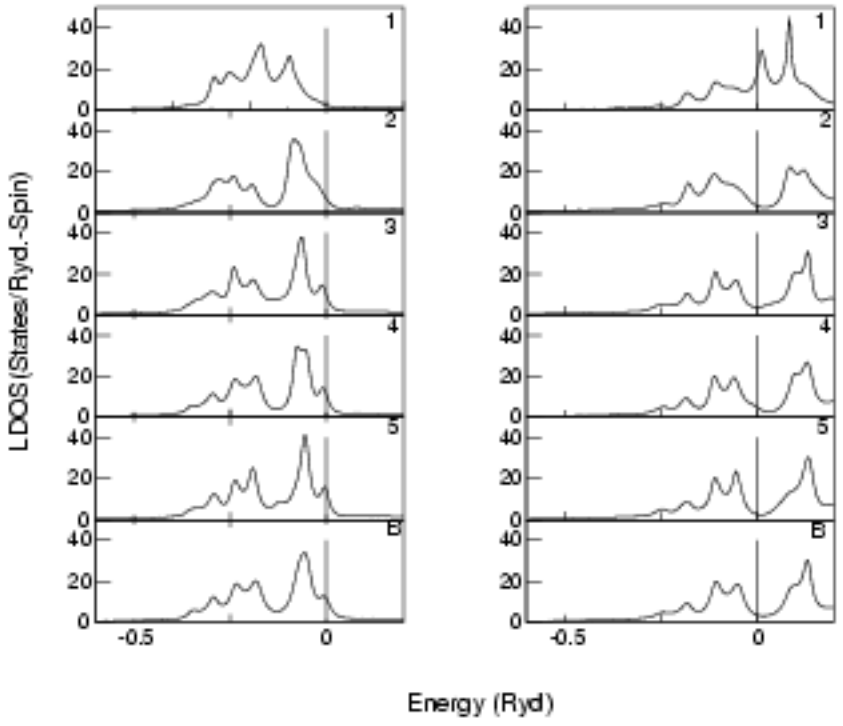

Figure 2.10: Layer resolved local density of states of a nine layer thick (001) bcc Fe film. The majority bands are shown in the left column and the minority bands are shown in right. Energy is measured with respect to the Fermi Energy.

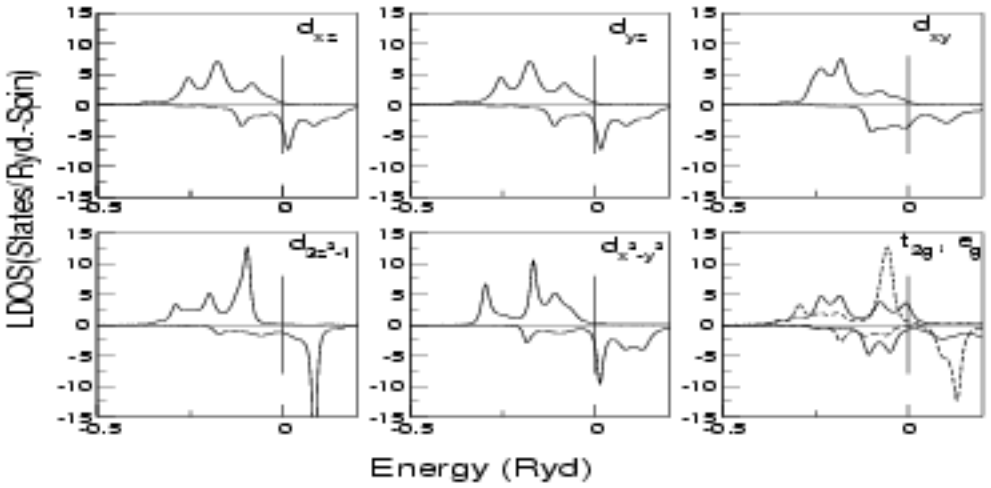

Figure 2.11: Orbital resolved LDOS for the d-states of the bcc Fe surface . The right hand bottom corner panel shows the splitting of d-orbitals in bulk. Energy is measured with respect to the Fermi Energy.

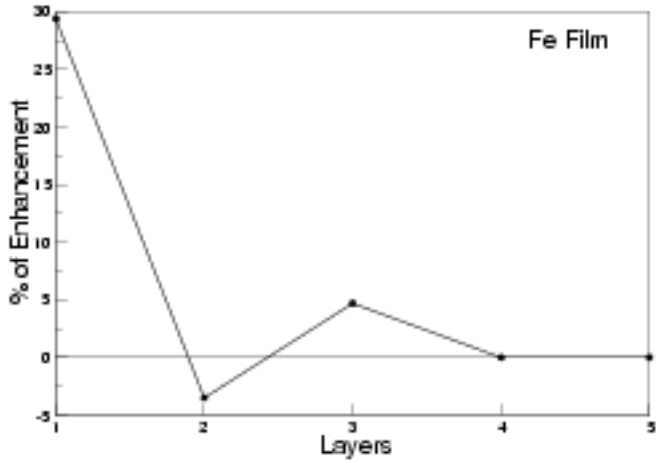

Figure 2.12: Magnetic enhancement (in %) of bcc (001) Fe thin film.

FPLMTO + SO (Eriksson 1991) and FPLAPW (Ohnishi and Freeman 1981). Not all of the approaches, however, show magnetic suppression in the penultimate layer. Table-2.9 shows the orbital decomposed charge and magnetic moments for the surface layer and

bulk. The magnetic moment of none of the orbital components are suppressed compared to bulk. Out of the two competing effects, described earlier, which determine the way charge redistributes among the *d*-orbitals (Jepsen *et al* 1982), it seems that the first effect is dominant, which results in depopulation of the d_{xz} and d_{yz} components. But for the d_{3z^2-1} orbital, there is no change in the population as compared to the bulk. The enhancement is mostly due to the three t_{2g} orbitals. The majority band for the t_{2g} orbitals was less saturated than the e_g ones in bulk, this perhaps facilitates their surface enhancement(Alden *et al* 1992). Again, the *s*-*p* orbitals play a significant role in the enhancement. The magnetic moment due to the *s*-*p* orbitals changes polarization. Figure 2.11 shows the orbital decomposed surface *d*-states and e_g and t_{2g} levels of bulk Fe. The lifting of the *d*-orbital degeneracies at the surface, is same as in Ni(001) thin films. This is expected as both are in a cubic structure and the cubic symmetry is broken at a (001) surface. Figure 2.12 shows the magnetic enhancement (in %) for different layers w.r.t bulk.

2.3.6 The body-centred cubic Fe (001) rough surface

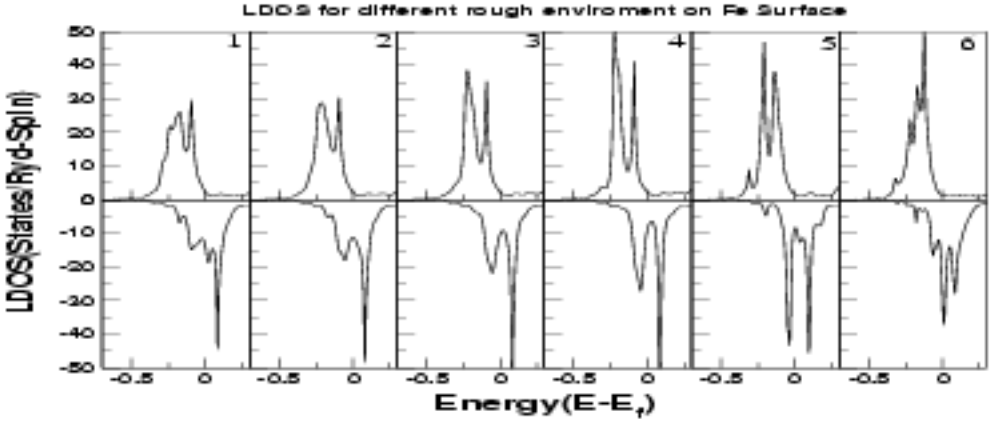

Figure 2.13: Majority and minority local density of states in the six local environments on a rough Fe bcc (001) surface

We have carried out the same analysis for a rough bcc Fe (001) surface as for Ni. The corresponding local densities of states are shown in Figure 2.13. The accompanying Table-2.10 shows the local moment. The magnetic moment of Fe is robust and the analysis of

Environment	Envir1	Envir2	Envir3	Envir4	Envir5	Envir6
Mag.mom.(μ_B)	3.16	2.86	2.78	2.68	2.64	2.57

Table 2.10: Magnetic moment of the Fe atoms for different environments with decreasing local curvature.

the magnetic roughness is different from that of Ni. Here, the environments are arranged in decreasing order of local curvature. As found in the earlier paper (Huda and Mookerjee 2003), the atoms on large curvatures on mounds have the largest moments. The moment of the Fe atom in environment 1 is nearest to the moment of an isolated Fe atom. Rough surfaces of Fe show the magnetic roughness as proportional to the curvature roughness as measured by the correlation functions of the two quantities. It should be noted that the recursion method, described in this paper, is one of the most powerful techniques which we can use for the study of rough surfaces where the two-dimensional translation symmetry still available on planar surfaces is also violated and the usual lower-dimensional Bloch theorem techniques are no longer feasible.

2.3.7 The body-centred cubic Cr (001) surface

Layer	Atomic sphere charges				Moments
	s	*p*	*d*	Total	(μ_B)
S+1	0.182	0.126	0.057	0.366	0.12
S	0.565	0.44	4.53	5.54	2.81
S-1	0.655	0.854	4.63	6.142	-1.38
S-2	0.657	0.848	4.49	5.99	1.00
S-3	0.634	0.843	4.48	5.95	-0.96
S-4	0.645	0.846	4.49	5.98	0.95

Table 2.11: Charges in the atomic spheres and magnetic moments in various layers of a nine-layer (001) slab of Cr

Barring Cr, all the thin films we have studied exhibit a ferromagnetic ground state. The ground state of Cr is anti-ferromagnetic with a Neel Temperature of 312^oC. The alternate Cr layers are anti-ferromagnetically aligned. The Cr surface magnetization is spectacularly enhanced. It shows an enhancement of almost 200%. The charge and

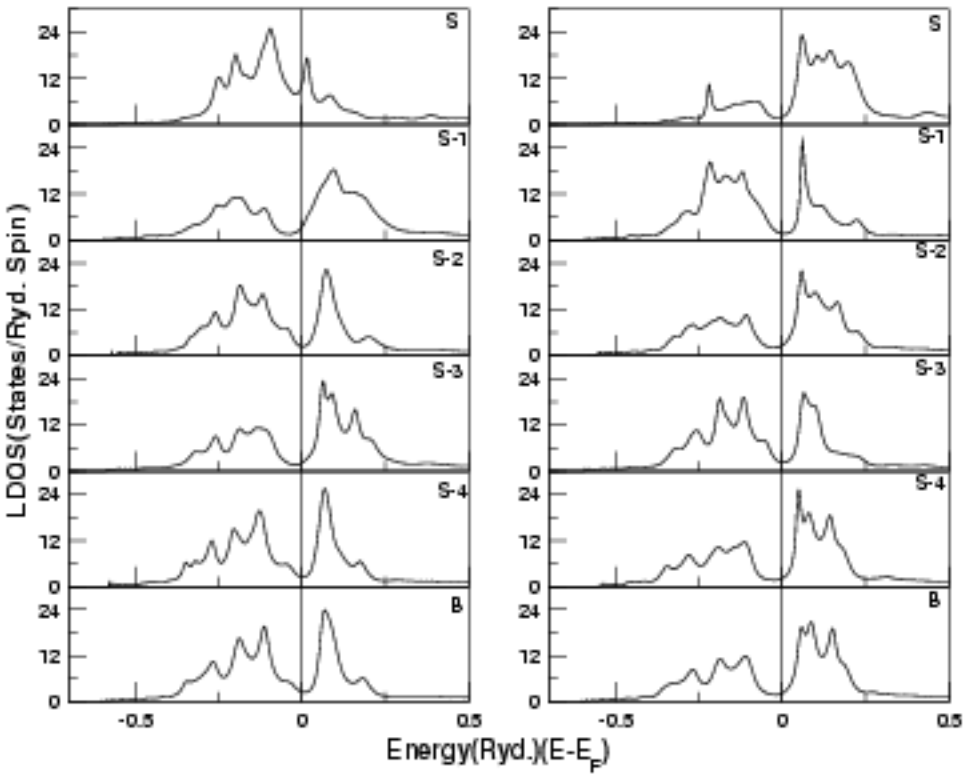

Figure 2.14: Majority and minority local density of states of bulk and different layers of Cr bcc (001) thin film.

magnetic moments of different layers of thin film is shown in Table-2.11. Figure 2.14 displays the layer and spin resolved LDOS. There is a significant dip near E_F for all the LDOS except the majority surface state. The disposition of the dip about E_F exhibits an interesting oscillation for the alternating layer, which can be attributed to the anti-ferromagnetic coupling. All the major features of the minority surface LDOS below E_F are subdued, but features in the majority surface state are much more developed compared to layers below it resulting in a mammoth magnetization gain.

Now if we delve a bit deeper into the orbital picture, more engrossing facts comes to light. Table-2.12 individual orbital projected charge and magnetic moment for the surface

	Surface Layer				Bulk			
Orbitals	Q ↑	Q ↓	Total Q	μ_B	Q ↑	Q ↓	Total Q	μ_B
s	0.306	0.259	0.565	0.048	0.332	0.331	0.653	0.011
p_x	0.088	0.078	0.166	0.01	0.141	0.141	0.282	-0.00083
p_y	0.088	0.078	0.166	0.01	0.141	0.141	0.282	-0.00083
p_z	0.059	0.049	0.108	0.01	0.141	0.141	0.282	-0.00083
d_{xy}	0.778	0.271	1.04	0.51	0.635	0.418	1.052	0.217
d_{xz}	0.751	0.18	0.931	0.57	0.635	0.418	1.052	0.217
d_{xz}	0.751	0.18	0.931	0.57	0.635	0.418	1.052	0.217
$d_{x^2-y^2}$	0.694	0.13	0.825	0.563	0.405	0.267	0.672	0.138
d_{3z^2-1}	0.661	0.135	0.796	0.525	0.405	0.267	0.672	0.138

Table 2.12: Orbital projected Charge and magnetic moment of surface layer and bulk of bcc (001) Cr.

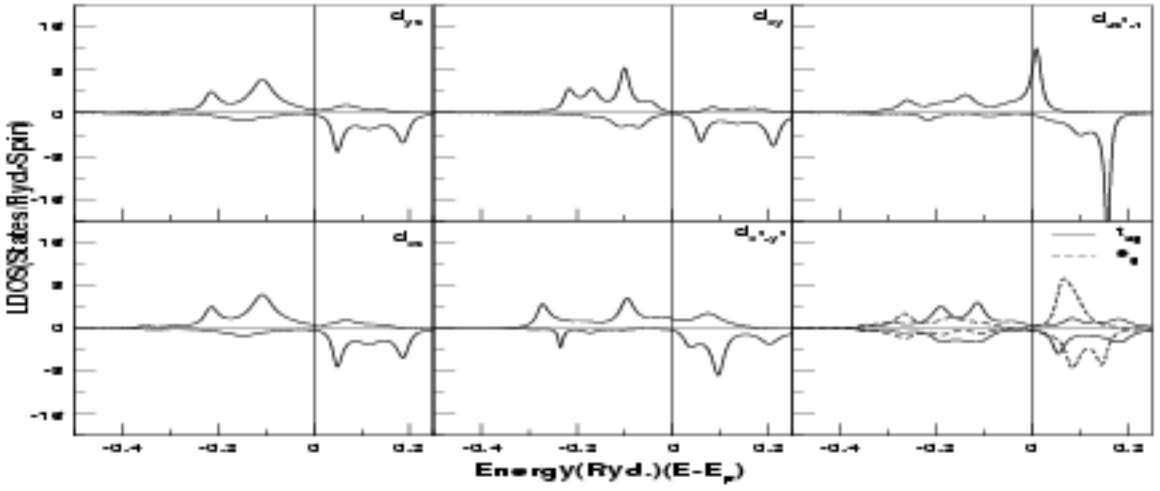

Figure 2.15: Orbital resolved LDOS for the d-states of the bcc Cr surface . The right hand bottom corner panel shows the splitting of d-orbitals in bulk. Energy is measured with respect to the Fermi Energy.

and bulk states of Cr.The p-states have changed their magnetic polarization at the surface. The each minority d-states which were already sparsely filled in bulk has undergone further depletion in their charges and each majority d-states has gained significantly. Though each

d-state contributes significantly to the surface enhancement, but contribution of $d_{x^2-y^2}$ is the most robust of all. Figure 2.15 shows the orbital resolved LDOS of d-states of surface and bulk Cr. In case of Cr as in Fe the argument put forward by Eriksson 1991 and Alden *et al* 1992 holds true.

2.3.8 The hexagonal closed-packed Co (001) surface

Layer	Atomic sphere charges				Moments
	s	p	d	Total	(μ_B)
S+1	0.062	0.063	0.032	0.16	0.007
S	0.623	0.551	7.61	8.78	1.66
S-1	0.662	0.788	7.62	9.07	1.57
S-2	0.654	0.766	7.57	8.99	1.58
S-3	0.658	0.768	7.59	9.01	1.57
S-4	0.657	0.767	7.57	9.00	1.58

Table 2.13: Charges in the atomic spheres and magnetic moments in various layers of a nine-layer slab of hcp (001) Co.

	Surface Layer				Bulk			
Orbitals	Q ↑	Q ↓	Total Q	μ_B	Q ↑	Q ↓	Total Q	μ_B
s	0.306	0.316	0.623	-0.01	0.317	0.333	0.65	-0.016
p_x	0.103	0.117	0.22	-0.014	0.118	0.138	0.256	-0.02
p_y	0.103	0.117	0.22	-0.014	0.118	0.138	0.256	-0.02
p_z	0.054	0.058	0.111	-0.003	0.118	0.141	0.259	-0.023
d_{xy}	0.914	0.606	1.52	0.309	0.92	0.593	1.51	0.326
d_{xz}	0.95	0.61	1.56	0.34	0.93	0.596	1.53	0.337
d_{yz}	0.95	0.61	1.56	0.34	0.93	0.596	1.53	0.337
$d_{x^2-y^2}$	0.91	0.60	1.52	0.31	0.919	0.593	1.51	0.326
d_{3z^2-1}	0.92	0.51	1.44	0.41	0.908	0.587	1.496	0.32

Table 2.14: Orbital projected Charge and magnetic moment of (001) surface layer and bulk of hcp Co.

The stable structure of Co is hexagonal closed packed (hcp). Table-2.13 shows the charge profile of the orbitals for different layers of nine layered hcp (001) Co thin film.

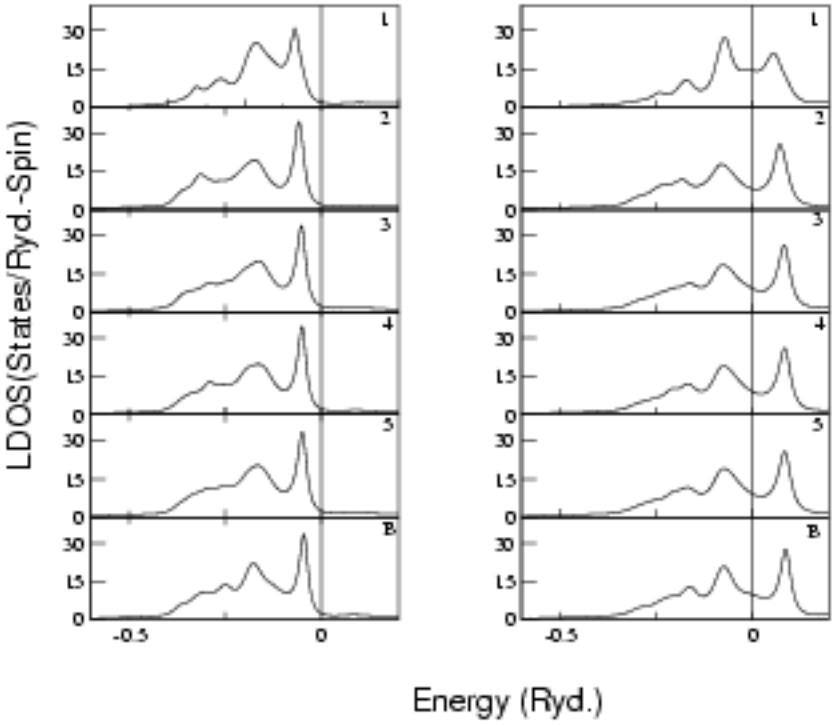

Figure 2.16: Layer resolved local density of states of a nine layer thick (001) hcp Co film. The majority bands are shown in the left column and the minority bands are shown in the right. Energy is measured with respect to the Fermi Energy.

The table shows variation of charge and magnetic moment with layers. Figure 2.16 shows the layer projected LDOS. Our magnetic enhancement for the surface layer is similar to Green's function result of Alden *et al* 1992 but substantially less than the FLMTO +SO results of Eriksson 1991 . The variation in the *d*-charge for different layers is very small. Here out of the two competing effects which determine the way charge redistributes among the *d*-orbitals (Jepsen *et al* 1982) , it seems that the second effect is dominant in case of d_{xz} and d_{yz} orbitals which results in increase of their population, compared to bulk. But for the d_{3z^2-1} orbital it is other way round, and there is a decrease in population. Here, among the *d*-orbitals, only this d_{3z^2-1} contributes significantly to the enhancement. The majority band of d_{3z^2-1} has the least saturation among all the *d*-orbitals of hcp bulk Co, which can be one of the reasons for the enhancement. Again *s*-*p*-bands play a significant role in the enhancement. We find significant enhancement due to *s*-*p*-bands. The magnetic moment

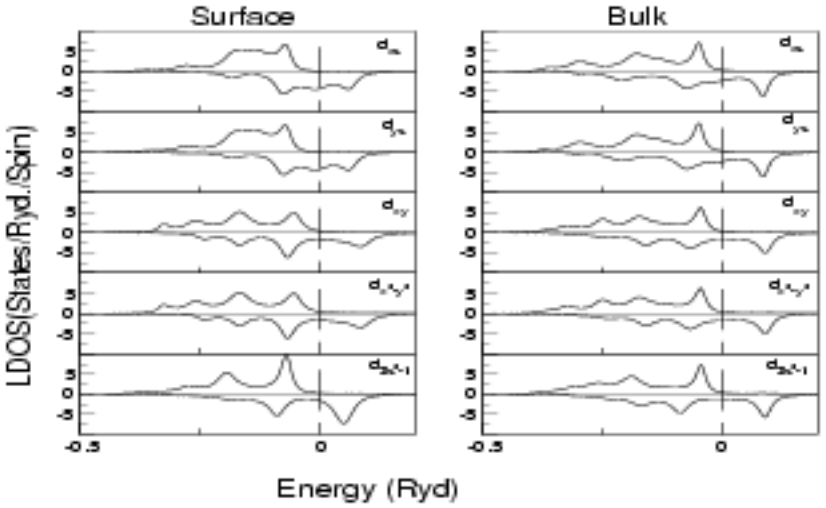

Figure 2.17: Orbital resolved LDOS for the *d*-states of the hcp Co (001) surface is shown in the left column. The right hand column show the splitting of *d*-states in bulk. Energy is measured with respect to the Fermi Energy.

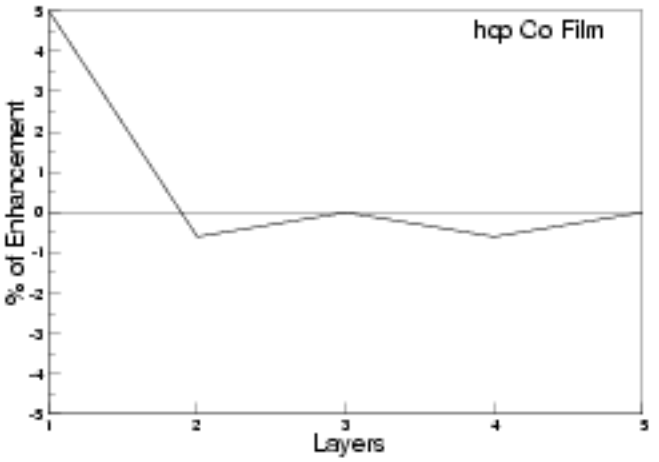

Figure 2.18: Magnetic enhancement(in %) of hcp (001) Co film

due to the s-p-band does not change polarization. The degeneracies for the surface states and bulk states are same. This is because in (001) surfaces the z-direction is rendered inequivalent, thus breaking the cubic symmetry in face-centred cubic and body centred

cubic films (Ni and Fe) but in case of hexagonal closed-packed, there is no additional symmetry breaking at the surface. Figure 2.17 shows the density of states of orbital decomposed d-bands for surface and bulk of hexagonal closed-packed Co. Both in bulk and surface $\{ d_{xz} , d_{yz}\}$ and $\{d_{x^2-y^2} , d_{xy}\}$ occur in degenerate pairs. Figure 2.18 shows the magnetic enhancement (in %) for different layers.

2.3.9 The face centred cubic Co (001) surface

Layer	Atomic sphere charges				Moments
	s	p	d	Total	(μ_B)
S+1	0.105	0.088	0.041	0.234	0.012
S	0.591	0.486	7.581	8.66	1.76
S-1	0.667	0.811	7.66	9.14	1.46
S-2	0.654	0.783	7.55	9.00	1.58
S-3	0.656	0.777	7.58	9.00	1.56
S-4	0.654	0.783	7.55	9.00	1.58

Table 2.15: Charges in the atomic spheres and magnetic moments in various layers of a nine-layer (001) slab of fcc Co.

Table-2.15 shows us the charge profile of the orbitals for different layers of nine layered fcc (001) Co film. We can see that the charge and magnetic moment oscillates with layers. Figure2.19 shows the layer projected LDOS. Narrowing of the surface state is seen. Our magnetic enhancement is similar to the Green's function results of Alden *et al* 1992 and the FLAPW results of Li and Freeman 1988. But, here also the magnetization is substantially suppressed for the layer below the surface layer. The % enhancement for both fcc(001) Ni and Co surfaces are of similar magnitude and similar amount of charge lealage is seen in both cases. Table-2.16 shows the orbital decomposed charge and magnetic moment for the surface layer and bulk. Here magnetic moment of d_{xy} is suppressed compared to bulk. Out of the two competing effects which determine the way charge redistributes among the d-orbitals (Jepsen *et al* 1982) , it seems that the second effect is dominant, which results in increase in population of the d_{xz} and d_{yz} components. But in case of d_{3z^2-1} state, the effect is reverse, and consequent depopulation is seen. Here all the other four d-orbitals (barring d_{xy}), contribute to the surface enhancement.The s-p-bands have a

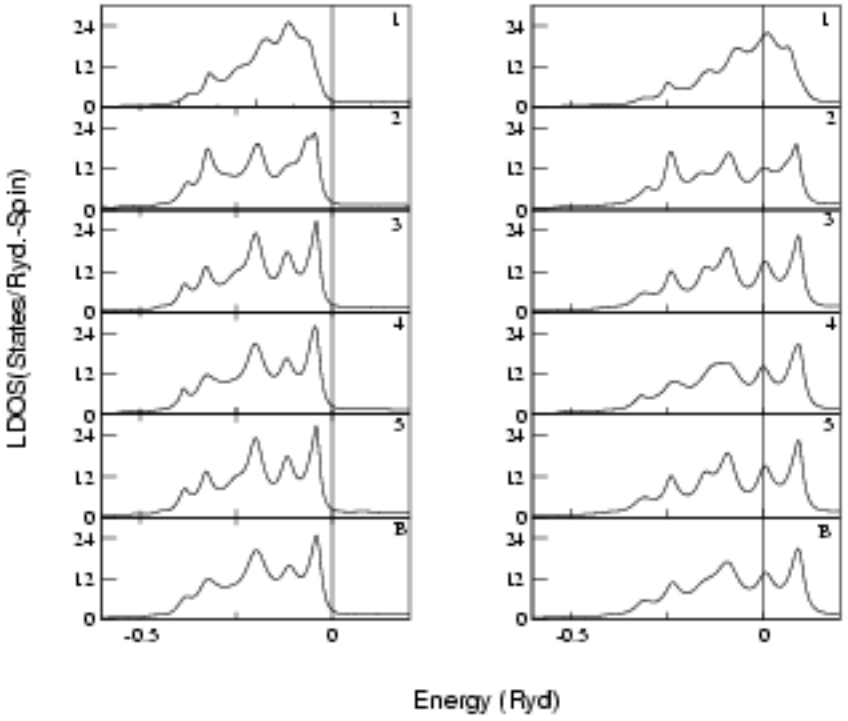

Figure 2.19: Layer resolved local density of states of a nine layer thick (001) fcc Co film. The majority bands are shown in the left column and the minority bands in the right. Energy is measured with respect to the Fermi Energy.

significant role in the enhancement. The magnetic moment due to the s-p-band does not change polarization. But the s and p_z band have almost equally populated majority and minority band. The lifting of the d-orbital degeneracies at the surface, is same as Ni and Fe thin films, because of its cubic structure. Figure 2.20 shows the orbital decomposed density of states of the surface d states and e_g and t_{2g} levels of bulk for fcc Cobalt. Figure 2.21 shows the magnetic enhancement (in %) for different layers.

2.4 Remarks and Conclusions

We have carried out an orbital decomposed study of the charge redistribution and magnetic moment in thin films of (001), (110) and (111) Ni (fcc), (001) Fe (bcc), (001) Cr(bcc) and (001) Co (both fcc and hcp). The blanket statements made earlier that the d states

	Surface Layer				Bulk			
Orbitals	Q ↑	Q ↓	Total Q	μ_B	Q ↑	Q ↓	Total Q	μ_B
s	0.295	0.295	0.59	0.000	0.322	0.337	0.659	-0.015
p_x	0.092	0.096	0.187	-0.004	0.122	0.141	0.263	-0.019
p_y	0.092	0.096	0.187	-0.004	0.122	0.141	0.263	-0.019
p_z	0.055	0.055	0.11	0.000	0.122	0.141	0.263	-0.019
d_{xy}	0.908	0.641	1.55	0.267	0.905	0.601	1.506	0.304
d_{xz}	0.935	0.599	1.535	0.34	0.905	0.601	1.506	0.304
d_{yz}	0.935	0.599	1.535	0.34	0.905	0.601	1.506	0.304
$d_{x^2-y^2}$	0.946	0.519	1.465	0.427	0.94	0.577	1.52	0.363
d_{3z^2-1}	0.95	0.547	1.497	0.403	0.94	0.577	1.52	0.363

Table 2.16: Orbital projected Charge and magnetic moment of (001) surface layer and bulk of fcc Co.

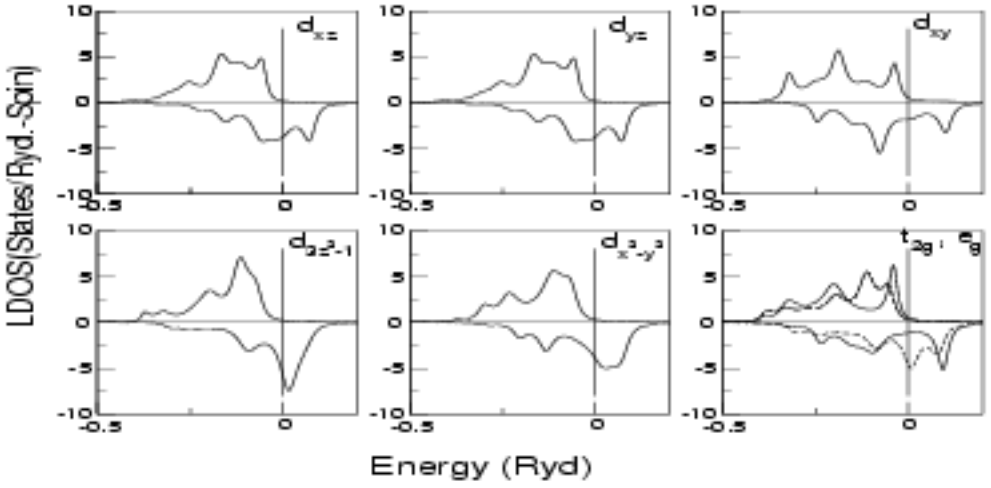

Figure 2.20: Orbital resolved LDOS for the *d*-states of the fcc Co surface . The right hand bottom corner panel shows the splitting of *d*-orbitals in bulk. Energy is measured with respect to the Fermi Energy.

are alone responsible for magnetism enhancement on surfaces do not seem to be totally correct. Firstly, not all *d*-components contribute to the surface enhancement. On the contrary, few of them have their magnetic moments suppressed for some surfaces . Classic example in this regard is Ni (111) surface where there is enhancement in few m-states,

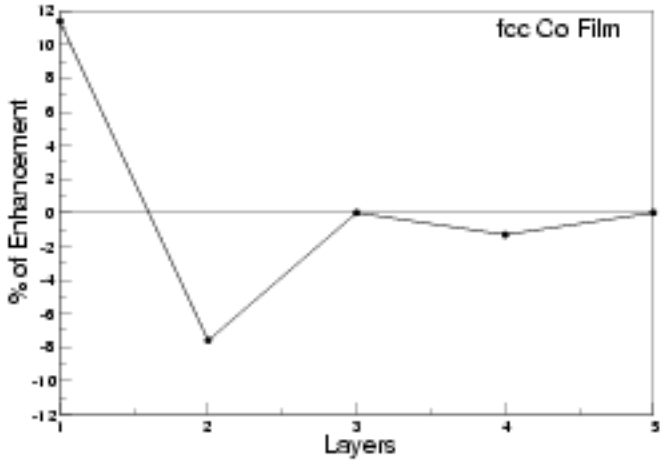

Figure 2.21: Magnetic enhancement(in %) of fcc (001) Co film

suppression in few, the net result being a surface moment similar to bulk. Secondly dominant effect which decides how charge distributes among its m-components is different for different surfaces. It is true that the majority band of Fe is less saturated than Nickel and Cobalt and this could be the reason for its huge surface enhancement (Alden *et al* 1992, Eriksson 1991), but when viewed from our orbital decomposed study, the most saturated m-components yields the maximum enhancement (like the Ni surface). But again their contention holds true for anti-ferromagnetic Cr surface. It seems that the conjecture of Alden *et al* 1992 and Eriksson 1991 holds true for more open structured body-centred cubic surfaces than surfaces of closed packed structures like face-centred cubic and hexagonal closed-packed . A Friedel-like oscillation in magnetic moment and charge is found in all the cases except the (111) Ni thin film. We conclude that magnetism at a surface is sensitively dependent on the charge transfers and redistribution among the orbital components as well as between the various layers and such a detailed study is required to get a clear picture of the phenomenon.

Chapter 3

Electronic and magnetic properties of the partially disordered systems : $Co_2Fe_{0.4}Cr_{0.6}Al$ a quaternary Heusler alloy

3.1 Introduction

Disordered alloys are of great technological importance and involve rich physics as well. During the last few decades considerable effort has gone into devising methods for carrying out averages of physical observables over different configurations realized by disordered systems. We will try to illustrate the importance of configuration averaging with the following example. Suppose a experimentalist is carrying out energy resolved photoemmission studies on a disordered metallic alloy. Varying the frequency of his incident photon and keeping the energy window of the excited outgoing electrons reasonably narrow, he can map out the density of states of the valence electrons of the alloy. If he carries out the experiment on ten different samples of the same alloy he should obtain slightly different results. The alloy is random and different samples will have different atomic arrangement of its constituents. Yet, the variation the experimenter sees in the different samples is well within his experimental error bars. What he observes is an average result, averaged over different realizable configurations of atomic arrangements in the alloy. The interesting fact is that he sees the averaged result in a single sample. The same is true for all global properties of the system like the specific heat, conductivity and different response functions.

People adopt different approaches to do configuration averaging in materials. The

mostly used methods are the coherent potential approximation (CPA) and the augmented space formalism (ASF). The supercell method is also used to study disorder effects but here the artifacts of the artificial supercell symmetry shows up. The augmented space is a direct product space of the underlying lattice space and the configuration space. This formalism carries out configuration averaging over all the important configurations and the magnitude of errors in the calculation are known and can be controlled. The self-consistent augmented space recursion in conjunction with TB-LMTO has been successfully developed and applied to different totally disordered systems (Chakrabarti and Mookerjee 2005). The formalism is robust enough to include subtle phenomena of disorder like short range effects into its scheme of things. In this chapter we will describe how the utility of augmented space theorem has been used to study the very important phenomena of partial-disorder. This had already been applied to model systems (Chakrabarti and Mookerjee 2002), here we have developed it further to study real systems. Many systems in nature exhibit partial-disorder, specially alloy of different metals at off-stoichiometry. Here we have chosen a system which is of great technological importance. Now we will try to understand the system as well as its importance.

The field of spintronics holds out a promise for the future as it could play a pioneering role in further integration of data storage, processing and transfer (Prinz 1998, Johnson 2000, Hirohata *et al* 2005). Datta and Das 1990 has proposed spin-polarized field-effect transistor (FET) as one of the major application of spintronics, which requires both injection and detection of spin across the ferromagnet/semiconductor interfaces with a very high efficiency. Two theoretical approaches have been proposed to meet this requirement: spin injection from the ferromagnet with nearly 100% spin polarization in a diffusive regime (Schmidt *et al* 2000), and insertion of a tunnel barrier into the ferromagnet/semiconductor interface to utilize ballistic electrons (Rashba 2000). The first of the two proposed approaches can meet the requirement using dilute magnetic semiconductors and half-metallic ferromagnets (HMF). The HMF are those materials, whose minority band exhibits a gap at the Fermi Level (E_F) whereas its majority band is perfectly metallic in nature, thus achieving 100% spin polarization at the E_F. Till date four types of HMF have been theoretically predicted: oxide compounds, e.g. , rutile CrO_2 (Schwarz 1986), prevoskites e.g., $La_{0.7}Sr_{0.3}MnO_3$ (Pickett and Singh 1996), zinc-blende

compounds e.g., MnAs, CrAs, CrSb (Shirai *et al* 1998, Shirai 2003) and Heusler alloys. The advantage of Heusler alloys over the other HMFs is its high Curie temperature, which lets one avail its half metallicity even at room temperature. Heusler alloys are called half-Heusler alloy if they have a general formula XYZ and full-Huesler alloy if they have general formula X_2YZ, where X and Y are d-block elements and Z is a p-block element. The crystal structure of Huesler alloy consists of four inter-penetrating fcc lattices. In a conventional unit cell Y and Z occupy the sub-lattices with origin at (0,0,0) and $(\frac{1}{2},\frac{1}{2},\frac{1}{2})$, while X and either a vacancy or another X atom occupy the sub-lattices with origins at $(\frac{1}{4},\frac{1}{4},\frac{1}{4})$ and $(\frac{3}{4},\frac{3}{4},\frac{3}{4})$.

We focus our attention on the doped quaternary Heusler alloy $Co_2Fe_{0.4}Cr_{0.6}Al$. This is a not a perfect HMF because unlike HMF it does not show a true gap at E_F in the minority band. This is an important material because of its ferromagnetic character at room temperature. Here it is worth mentioning that, though Co_2CrAl exhibits a HMF character, its Curie temperature is below the room temperature, but there are experimental reports that on substituting Cr atom with Fe there is an enhancement in Curie temperature. Also at this particular concentration polycrystalline $Co_2Fe_{0.4}Cr_{0.6}Al$ shows a high magneto-resistance ratio of up to 30% at a relatively low field of 0.1T (Wurmehl *et al* 2006, Felser *et al* 2003) though a similarly prepared samples of Co_2CrAl shows a negligible magnetoresistance. This property is ascribed to spin-polarized tunneling between grains(Kelekar and Clemens 2004). In addition it shows phase separation (Kobayashi *et al* 2004) and tunnel magneto-resistance (Inomata *et al* 2003, Kubota *et al* 2004) at room temperature for the magnetic tunnel junction which utilizes $Co_2Fe_{0.4}Cr_{0.6}Al$ and Co_2MnAl as an electrode. These exotic features of this compound has motivated experimental groups to study the thin films of this compound as well as its parent compounds(Hirohata *et al* 2005, Kelekar and Clemens 2004).

There have been several theoretical attempts in understanding the electronic and magnetic behaviour of Heusler alloys. Among them is the full-potential screened Korringa-Kohn-Rostocker(KKR) method in conjunction with either coherent potential approximation or super cell construction to account for the random distribution of Cr and Fe atoms. Results using fully relativistic version of the KKR-CPA formalism has been reported by Wurmehl *et al* 2006 for $Co_2Fe_xCr_{1-x}Al$ for different doping, to study the magnetic nature

of the alloy at different doping. They have studied the $L2_1$, B2 and A2 phases and their combinations separately. For the $L2_1$ phase and for x = 0.4 their site projected magnetic moment for Co, Cr and Fe were $0.94\mu_B$, $1.42\mu_B$ and $2.92\mu_B$ respectively, whereas their experimental values were $1.11\mu_B$, $0.36\mu_B$ and $2.64\mu_B$ respectively. Reference Antonov *et al* 2005 reported super cell based fully relativistic LMTO calculation of $Co_2Fe_xCr_{1-x}Al$ varying the concentration of Fe and Cr. Their observation was that, the concentration and arrangement of Fe played a decisive role in determining the magnetic properties of the alloy and its constituents. Their theoretically calculated magnetic moments for Fe and Co were quite near to their experimental values, but that for Cr was highly overestimated. The large overestimation of the Cr moment is common to all the theoretical approaches. For all other phases their results also show higher magnetic moment than the experimental observations. Miura *et al* 2004 theoretically studied the $Co_2Fe_{0.4}Cr_{0.6}Al$ using KKR-CPA formalism. Their findings indicate that spin polarization of $Co_2Fe_xCr_{1-x}Al$ at E_F, decreases with increasing Fe concentration in both the $L2_1$ and B2 phases and disorder effect plays a significant role on the spin polarization(at E_F) at low Fe concentration. Elmers *et al* 2003 used magnetic circular dichroism (MCD) and X-ray absorption spectroscopy (XAS) to study the $Co_2Fe_{0.4}Cr_{0.6}Al$ experimentally. From these data they have also obtained site projected magnetic moments using magneto-optical sum rules and have compared them with band structure calculations. Recently there has been a spurt in experimental activity on thin films of Co_2CrAl and Co_2FeAl . Hirohata *et al* 2005 reported magnetic properties of both $L2_1$ polycrystalline Co_2CrAl and epitaxial $L2_1$- structured Co_2FeAl films on GaAs(001) substrate. Their observations showed the existence of uniaxial magnetic anisotropy along the [1-10] for Co_2FeAl . On the other hand Co_2CrAl showed an isotropic M-H loop. In an another work Kelekar and Clemens 2004 reported a method of development of single-phase epitaxial thin films for $Co_2Fe_xCr_{1-x}Al$ and observed large Hall resistivity in the range $(4-5)\times10^{-8}$ Ω m at 5 K for x=0.4.

In this chapter we have investigated the magnetic and electronic properties of the bulk and (001) thin film of HMF $Co_2Fe_{0.4}Cr_{0.6}Al$ alloy, using TB-LMTO and ASR formalism. Here we have taken $L2_1$ unit cell with $Fm\bar{3}m$ symmetry, with experimental lattice parameter $a = 5.727$ A (Wurmehl *et al* 2006). The Co site is at $8c(\frac{1}{4},\frac{1}{4},\frac{1}{4})$ and the Al site is situated at $4a(0,0,0)$. The Fe and Cr occupy the $4b(\frac{1}{2},\frac{1}{2},\frac{1}{2})$ site with probability 0.4

and 0.6, respectively. Figure 3.1 shows the unit cell of a Heusler alloy.

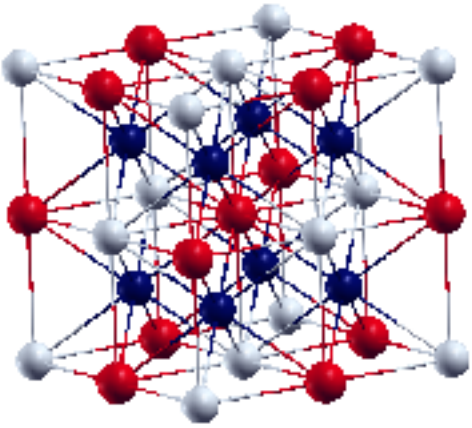

Figure 3.1: The unit cell of a full-Heusler alloy X_2YZ where X and Y are transition metal atoms and Z a sp-metal atom. The light coloured spheres represent Al, the red spheres represent Fe or Cr and the dark blue spheres represent Co.

This is an ideal case for the study of partial disorder (PD) in the $L2_1$ phase. Here the 8*c* and 4*a* sites are occupied by the respective atoms with probability 1, and disorder shows up in the 4*b* sites only. This consideration is of prime importance in order to account for the occupancy of the sub lattice positions in $L2_1$ when we are away from the stoichiometric case (Co_2FeAl or Co_2CrAl). To mimic a free standing Fe/Cr and Al terminated partially disordered thin film of $Co_2Fe_{0.4}Cr_{0.6}Al$, we have considered a nine layer thick films separated by seven layers of empty sphere.

3.2 Methodology

In this section we generalize the TB-LMTO-ASR formalism to many atoms per unit cell, which is required to study systems having different disorder in different sub lattices. Since the recursion method needs a localized, short-ranged basis for its operation, one can implement augmented space recursion in the framework of the TB-LMTO formalism.

The second order TB-LMTO Hamiltonian in the most localized representation is given by,

$$\mathbf{H}^{(2)}_{\sigma} = \mathbf{E}^{\sigma}_{\nu} + \mathrm{h}^{\sigma} - \mathrm{h}^{\sigma}\ \mathrm{o}^{\sigma}\ \mathrm{h}^{\sigma} \tag{3.1}$$

where,

$$\mathrm{h}^{\sigma} = \sum_{RL\alpha} (C^{\sigma}_{RL\alpha} - E^{\sigma}_{\nu RL\alpha})\ \mathbf{P}_{RL\alpha} + \sum_{RL\alpha}\sum_{R'L'\alpha'} \Delta^{\sigma\ 1/2}_{RL\alpha}\ S_{RL\alpha,R'L'\alpha'}\ \Delta^{\sigma\ 1/2}_{R'L'\alpha'}\ \mathbf{T}_{RL\alpha,R'L'\alpha'} \tag{3.2}$$

- R denotes a *cell position* label associated with a TB-LMTO basis and $L = (\ell m)$ is the composite angular momentum index.
- σ is the spin index and α denotes an atom in the R-th cell whose position is $R + \xi^{\alpha}$.
- C, o and Δ are potential parameters of the TB-LMTO method, these are diagonal matrices in the angular momentum indices. Also o^{-1} has the dimension of energy and is a measure of the energy window around $\bar{E}$ in which the approximate Hamiltonian $\mathbf{H}^{(2)}$ is reliable.
- $\mathbf{P}_{RL\alpha}$ and $\mathbf{T}_{RL\alpha,R'L'\alpha'}$ are the projection and transfer operators in Hilbert space H spanned by tight-binding basis $\{|RL\alpha\sigma\rangle\}$.

To incorporate disorder in the system, we consider C, o and Δ to be random, while the structure matrix is non random. The justification for the non randomness of the structure matrix is that, we calculate properties of those alloys, where the effect due to individual component size mismatch is negligible. We introduce a site-occupation variable n^{α}_{R} which takes values 0 or 1 depending upon whether site α in the R-th cell is occupied by an A or a B atom. In the absence of short-range ordering, the probability density of these variables are given by :

$$\Pr(n^{\alpha}_{R}) \ = \ x^{\alpha}\ \delta(n^{\alpha}_{R}) \ + \ y^{\alpha}\ \delta(n^{\alpha}_{R} - 1)$$

x^a and y^a are the concentrations of A and B components occupying the a labelled atom in the unit cell.

For *partial disorder* this is a random variable whose probability density depends upon which sub lattice it belongs to, hence the label a is associated with it. In terms of n_R^a the random site and angular momentum diagonal potential parameters take the following form:

$$\begin{aligned} V_{RLa}^{\sigma} &= V_L^{A\sigma}\ n_R^a + V_L^{B\sigma}\ (1 - n_R^a) = V_L^{B\sigma} + \delta V_L^{\sigma}\ n_R^a \\ \delta V_L^{\sigma} &= V_L^{A\sigma} - V_L^{B\sigma} \end{aligned}$$

where, V_{RLa}^{σ} can be any one of C_{RLa}^{σ}, $\Delta_{RLa}^{\sigma\ 1/2}$, o_{RLa}^{σ} and $E_{\nu RLa}^{\sigma}$.

We now obtain the Hamiltonian $\mathbf{H}^{(2)}$ as a function of the random occupation variables by inserting above expressions in h and finally inserting h in expression (1). To set up the effective Hamiltonian from which we may obtain the configuration averaged Green function, we follow the prescription of the Augmented space theorem Mookerjee 1973. With each random variable n_R^a we associate an operator M_R^a whose spectral density is the probability density of n_R. The theorem tells us that :

$$\ll G^{\sigma}(\{n_R^a\}, z) \gg = \langle\{\emptyset\}_f| \left(z\hat{\mathbf{I}} - \widehat{\mathbf{H}}_{\sigma}^{(2)}(\{\widehat{\mathrm{M}}_R^a\})\right)^{-1} |\{\emptyset\}_f\rangle \tag{3.3}$$

The augmented Hamiltonian $\widehat{\mathbf{H}}^{(2)}$ is constructed by replacing the random site occupation variables n_R^a by their corresponding operators $\widehat{\mathrm{M}}_R^a$. The eigenstates $|0^{Ra}\rangle$ and $|1^{Ra}\rangle$ of $\widehat{\mathrm{M}}_R^a$ span the *configuration space* ϕ^{Ra}. The effective Hamiltonian $\widehat{\mathbf{H}}^{(2)}$ is an operator in the augmented space $\Psi = H \otimes \prod^{\otimes}\ \phi^{Ra}$, where H is the space spanned by the TB-LMTO basis. A representation of $\widehat{\mathrm{M}}_R^a$ is given by

$$\begin{aligned} \mathrm{M}_R^a &= x^a \mathbf{P}_{Ra}^{\downarrow} + y^a \mathbf{P}_{Ra}^{\uparrow} + \sqrt{x^a y^a}\ \mathbf{T}_{Ra}^{\downarrow\uparrow}\ \epsilon\ \phi^{Ra} \\ \widehat{\mathrm{M}}_R^a &= \mathbf{I} \otimes \ldots \mathrm{M}_R^a \otimes \ldots \mathbf{I} \otimes \ldots\ \epsilon\ \prod^{\otimes} \phi^{Ra} = \Phi \end{aligned} \tag{3.4}$$

The representation is in a basis $|\uparrow^{Rα}\rangle = \sqrt{x^α}|0^{Rα}\rangle + \sqrt{y^α}|1^{Rα}\rangle$ and $|\downarrow^{Rα}\rangle = \sqrt{y^α}|0\rangle - \sqrt{x^α}|1^{Rα}\rangle$. $P^{\downarrow}_{Rα} = |\downarrow^{Rα}\rangle\langle\downarrow^{Rα}|$ and $T^{\uparrow\downarrow}_{Rα} = |\uparrow^{Rα}\rangle\langle\downarrow^{Rα}| + |\downarrow^{Rα}\rangle\langle\uparrow^{Rα}|$ are the projection and transfer operators in the configuration space Φ. A general configuration state is of the type $|\downarrow\uparrow\uparrow\downarrow\ldots\rangle$. The sequence of sites $\{C\}$ where the configuration is $\downarrow$ uniquely describes a configuration. This is called the *cardinality* sequence. The *average* configuration is one which has $\uparrow$ everywhere : or the null cardinality sequence $|\{\emptyset\}^{\downarrow}_{\uparrow}\rangle$.

A little algebra yields the following : If $V^{σ}_{RLα}$ is a random potential parameter, diagonal in real and angular momentum space (as defined earlier) then we may define the following operators in configuration space :

$$\begin{aligned}
\bar{\mathbf{A}}(V^{σ}_{RLα}) &= (x^α\ V^{σ}_{AL} + y^α\ V^{σ}_{BL})\ \bar{\mathbf{I}}\otimes\ldots\mathbf{I}\otimes\ldots\mathbf{I}\ldots \\
\bar{\mathbf{B}}(V^{σ}_{RLα}) &= (y^α - x^α)\,(V^{σ}_{AL} - V^{σ}_{BL})\ \mathbf{I}\otimes\ldots\mathbf{P}^{\downarrow}_{Rα}\otimes\ldots\mathbf{I}\otimes\ldots \\
\bar{\mathbf{F}}(V^{σ}_{RLα}) &= \sqrt{y^α x^α}\,(V^{σ}_{AL} - V^{σ}_{BL})\ \mathbf{I}\otimes\ldots\mathbf{T}^{\uparrow\downarrow}_{Rα}\otimes\ldots\mathbf{I}\otimes\ldots \\
&\text{and} \\
\bar{\mathbf{D}}(V^{σ}_{Rα}) &= \bar{\mathbf{A}}(V^{σ}_{Rα}) + \bar{\mathbf{B}}(V^{σ}_{Rα}) + \bar{\mathbf{F}}(V^{σ}_{Rα})
\end{aligned}$$

The augmented space Hamiltonian then has the following compact form :

$$\begin{aligned}
\widehat{\mathbf{H}}^{(1)}_{σ} &= \sum_{RLα}\bar{\mathbf{D}}(C^{σ}_{Rα})\otimes\mathbf{P}_{RLα}\ldots \\
&\quad + \sum_{RLα}\sum_{R'L'α'}\bar{\mathbf{D}}(\Delta^{σ\ 1/2}_{RLα})S_{RLα,R'L'α'}\bar{\mathbf{D}}(\Delta^{σ\ 1/2}_{R'L'α'})\otimes\mathbf{T}_{RLα,R'L'α'} \\
\hat{\mathrm{h}}^{σ} &= \sum_{RLα}\bar{\mathbf{D}}(C^{σ}_{Rα} - E^{α}_{νRLα})\otimes\mathbf{P}_{RLα}\ldots \\
&\quad + \sum_{RLα}\sum_{R'L'α'}\bar{\mathbf{D}}(\Delta^{σ\ 1/2}_{RLα})\ S_{RLα,R'L'α'}\ \bar{\mathbf{D}}(\Delta^{σ\ 1/2}_{R'L'α'})\otimes\mathbf{T}_{RLα,R'L'α'} \\
\hat{\mathrm{o}}^{σ} &= \sum_{RLα}\bar{\mathbf{D}}(\mathcal{O}^{σ}_{Rα})\otimes\mathbf{P}_{RLα}
\end{aligned}$$

Thus :

$$\widehat{\mathbf{H}}^{(2)}_{σ} = \widehat{\mathbf{H}}^{(1)}_{σ} - \hat{\mathrm{h}}^{σ}\ \hat{\mathrm{o}}^{σ}\ \hat{\mathrm{h}}^{σ} \tag{3.5}$$

Using the augmented space theorem, we can write the expression of configuration averaged Green function as,

$$\ll G^{\sigma}_{RL\alpha,RL\alpha}(z) \gg = \langle 1| \left(z\hat{\mathbf{I}} - \widehat{\mathbf{H}}^{(2)}_{\sigma} \right)^{-1} |1\rangle$$

where,

$$|1\rangle \;=\; |R \otimes L \otimes \alpha \otimes \{\emptyset\}\rangle$$

In order to obtain the Green function we shall use the recursion method of Haydock *et al* 1972. This technique transforms the sparse representation of the TB-LMTO Augmented space Hamiltonian to a tridiagonal form. This is done by constructing a new orthonormal basis set $|n\}$ from the older one $|n)$ by the following three term recursion formula :

$$|n+1\} = H|n\} + a_n|n\} + \beta^2_{n-1}|n-1\} \tag{3.6}$$

with the initial choice $|1\}$=$|1)$, and $\beta^2_0 = 1$. The coefficients a_n and β_n are obtained by imposing the Otho-normalizability condition of the new basis set. They are given by :

$$\frac{\{n|H|n\}}{\{n|n\}} = a_n; \qquad \frac{\{n|H|n-1\}}{[\{n|n\}\{n-1|n-1\}]^{1/2}} = \beta^2_n; \qquad \{n|H|m\} = 0 \quad (m < n-1) \tag{3.7}$$

Now the diagonal elements of the Green function can be calculated from the following expression:

$$G^{\sigma}_{RL\alpha,RL\alpha}(z) = \cfrac{1}{z - a_1 - \cfrac{\beta^2_1}{z - a_2 - \cfrac{\beta^2_2}{z - a_3 - \cfrac{\beta^2_3}{\ddots \cfrac{}{z - a_N - \beta^2_N T(z)}}}}} \tag{3.8}$$

The above infinite continued fraction is terminated after a finite $n = N$(say) and the asymptotic part is replaced by a *terminator* calculated from the first N coefficients as suggested by Beer and Pettifor 1982.

The basis site, angular momentum projected density of states (LDOS) is related to the configuration averaged Green function :

$$n^{\sigma}_{L\alpha}(E) = -\frac{1}{\pi}\,\Im m \lim_{\delta \to 0} \ll G^{\sigma}_{RL\alpha,RL\alpha}(E - i\delta^{+}) \gg \tag{3.9}$$

The Fermi energy E_F is obtained from :

$$\int_{-\infty}^{E_F} dE \sum_{L\alpha\sigma} n^{\sigma}_{L\alpha}(E) = \ll n \gg$$

where, $\ll n \gg$ is the average valence electrons per cell.

The basis site, angular momentum projected magnetic moment is obtained from :

$$m_{L\alpha} = \int_{-\infty}^{E_F} dE \left(n^{\uparrow}_{L\alpha}(E) - n^{\downarrow}_{L\alpha}(E) \right) \tag{3.10}$$

3.3 Results for Bulk $Co_2Fe_{0.4}Cr_{0.6}Al$

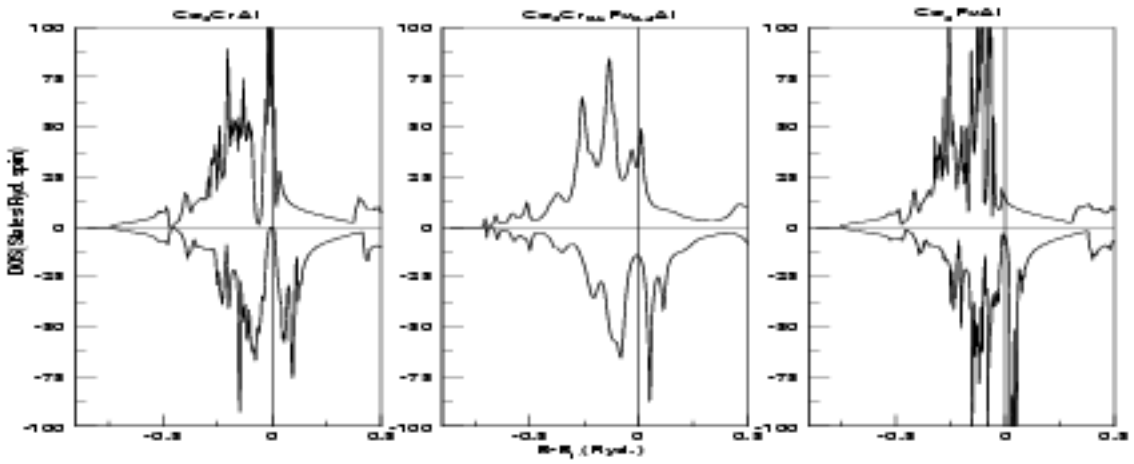

Figure 3.2: Total spin resolved DOS of $Co_2Fe_xCr_{1-x}Al$ (x = 0,0.4,1). $Co_2Fe_{0.4}Cr_{0.6}Al$ (centre panel) compared with those of Co_2CrAl (left panel) and Co_2FeAl (right panel). Minority states are shown on a negative scale

First, the electronic structure and magnetic properties of pure compounds is compared with the $L2_1$ partially disordered alloy. The spin resolved total DOS for the three cases

x = 0,0.4 and 1 are displayed in Figure 3.2. It shows that the Fermi level is situated in a valley in the minority spin density of states. It is seen that for x = 0, spin minority band shows a gap which is a hall mark of HMF, but with increase in the Fe concentration first the gap disappears and then for x = 1 it exhibits a sharp dip forming a pseudo gap. This can be understood from the fact, that with the introduction of disorder in the 4*b* site, the Van Hove singularities are washed away and consequently the band gap in the minority state is filled up. Yet, vestiges of the kink singularities remain in the DOS as a signature of partial disorder. The contribution from majority density of states at E_F decreases with increase in Fe concentration. This decrease is monotonic in nature and maximum for Co_2FeAl . A more detailed study of the spin resolved site projected DOS (Figure 3.3) reveals that in Co_2CrAl the bonding states in the minority band is more Co like, where the anti-bonding state is dominated by Cr . The same feature has also been reported by earlier studies. For Co_2FeAl the structures below the Fermi level are dominated by the Co majority band. But above E_F it has contribution from both Co and Fe. In the majority band we see that the two distinct peaks of Fe reinforces the sharp peaks of Co. In the $Co_2Fe_{0.4}Cr_{0.6}Al$ the feature is little different. We see from Figure 3.3 that both Fe and Cr retain the structures of their respective parent compound, except for the peak in majority band of Cr at the E_F, which has been shifted slightly towards right. This has major significance in the magnetic moment of Cr which we will discuss later.

The effect of alloying is very prominent in Al and Co. First we observe that the HMF like behaviour is lost due to filling up of gap at the E_F in the minority states in these two constituents. Now we discuss the effect of charge transfer on magnetism of $Co_2Fe_{0.4}Cr_{0.6}Al$ alloy. Table-3.1 displays the element specific spin resolved charges and total magnetic moment. For Co and Fe our calculated values are closest to the experimental observations although the Cr moment is over-estimated. This over-estimation of the Cr moment has been a recurrent feature of all earlier work. We shall examine whether this is due to the inaccuracy of the electronic structure calculations used or due to the way we decide to treat the partial disorder in the system.

From table-3.1 we see that the magnetic moment of Cr in the $Co_2Fe_{0.4}Cr_{0.6}Al$ has decreased by an amount 0.576 with respect to Co_2CrAl . This is due to the fact that it has lost 0.392 amount of charge (with respect to pure compound) from majority band.

$Co_2Fe_{0.4}Cr_{0.6}Al$

	Charge									Mag.Mom
	$s\uparrow$	$p\uparrow$	$d\uparrow$	$s\downarrow$	$p\downarrow$	$d\downarrow$	$\uparrow$	$\downarrow$	Tot.	(μ_B)
Co	0.346	0.402	4.38	0.345	0.429	3.282	5.127	4.052	9.179	1.075(1.11*)
Cr	0.294	0.370	2.544	0.299	0.397	1.542	3.209	2.237	5.446	0.972(0.36*)
Fe	0.348	0.437	4.591	0.345	0.459	1.958	5.38	2.763	8.143	2.617(2.64*)
Al	0.490	0.692	0.213	0.503	0.764	0.244	1.394	1.511	2.905	-0.117

Co_2CrAl

	Charge									Mag.Mom
	$s\uparrow$	$p\uparrow$	$d\uparrow$	$s\downarrow$	$p\downarrow$	$d\downarrow$	$\uparrow$	$\downarrow$	Tot.	(μ_B)
Co	0.332	0.402	4.253	0.320	0.415	3.492	4.987	4.227	9.214	0.760 (0.55*)
Cr	0.284	0.369	3.037	0.284	0.376	1.482	3.69	2.142	5.832	1.548(0.19*)
Al	0.454	0.675	0.205	0.466	0.718	0.221	1.334	1.405	2.739	-0.071

Co_2FeAl

	Charge									Mag.Mom
	$s\uparrow$	$p\uparrow$	$d\uparrow$	$s\downarrow$	$p\downarrow$	$d\downarrow$	$\uparrow$	$\downarrow$	Tot.	(μ_B)
Co	0.306	0.377	4.440	0.312	0.409	3.283	5.123	4.004	9.127	1.119(1.57*)
Fe	0.333	0.411	4.634	0.326	0.432	1.911	5.378	2.669	8.047	2.709(2.15*)
Al	0.458	0.646	0.194	0.464	0.713	0.222	1.298	1.399	2.697	-0.101

Table 3.1: The orbital resolved charges in Fe and Cr atomic spheres in $Co_2Fe_xCr_{1-x}Al$ alloy. Tot. is site projected total charge. * are the corresponding experimental values from Wurmehl *et al* 2006.

A more careful study reveals that major portion of the charge is lost from majority d band. This is also evident in the Cr projected DOS shown in Figure 3.3 where we see that the sharp peak at E_F has been pushed towards right wards from the Fermi level which accounts for the charge loss. Since the DOS of Fe is almost same with respect to Co_2FeAl , it also retains the value of its magnetic moment. Al shows a small but noncero magnetic moment and it is oppositely polarized with respect to the other constituents in the $Co_2Fe_{0.4}Cr_{0.6}Al$.

We have also studied the variation of the site-projected magnetic moments as a function of the Fe-Cr disorder, which is shown in Figure 3.4. The trends are very similar to

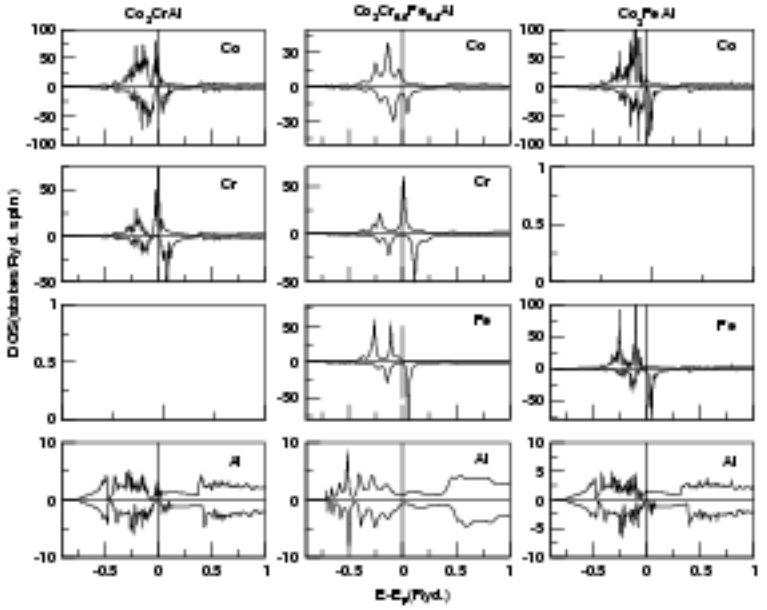

Figure 3.3: Site projected spin resolved DOS of $Co_2Fe_xCr_{1-x}Al$ (x = 0,0.4,1). Minority states are shown on a negative scale

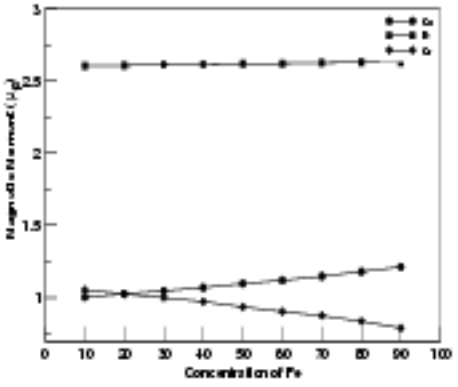

Figure 3.4: Variation of site-projected magnetic moments in $Co_2Fe_{0.4}Cr_{0.6}Al$ with the variation in Fe/Cr concentration

those reported earlier (Wurmehl *et al* 2006). The overestimation of the Cr moment, in comparison with experiment, is consistent for all concentrations and of the same order of magnitude as earlier work using different theoretical techniques. We shall comment on

this in our concluding section.

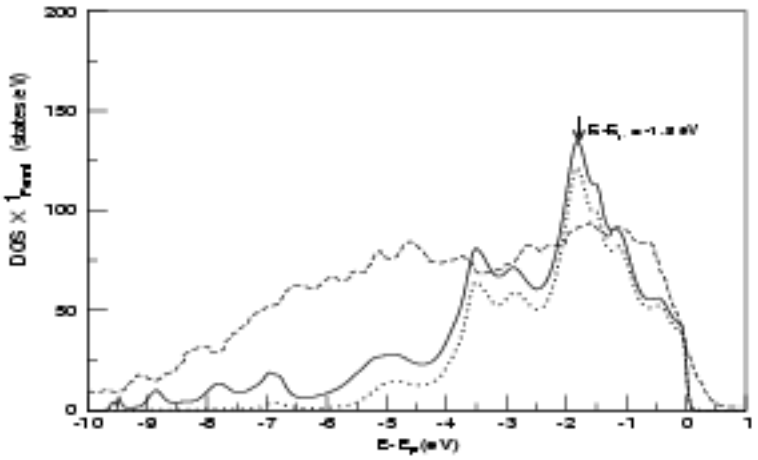

Figure 3.5: Comparison between the VB-XPS data of Wurmehl *et al* 2006 and the Fermi function convoluted total density of states for $Co_2Fe_{0.4}Cr_{0.6}Al$. The dotted lines show the total *d*-projected DOS

It would be interesting to compare our density of states results with experimental photoemmission spectra for $Co_2Fe_{0.4}Cr_{0.6}Al$ excited by hard X-rays as reported by Wurmehl *et al* 2006. The experimental data (Figure 3.5) indicate a broad feature of width about 2 eV is seen just below the Fermi energy. A second feature is seen between 4 eV and 7 eV below the Fermi energy. The Figure 3.5 shows the comparison between the VB-XPS data and the total density of states convoluted with the Fermi function corresponding to the experimental temperature. The density of states show two distinct features. First, the structure due to the *d*-states around and just below the Fermi energy going down almost 5 eV below it. Below this are the features due to the *s*-*p* states down to 10 eV below the Fermi energy. The Figure shows that the total width of the structures due to the *d*-states has a width of about 7 eV, which is also the conclusion from the high-resolution, high-energy spectra. The disagreement between the emission spectrum and the total DOS is qualitatively similar to the work of Wurmehl *et al* 2006. The DOS shows a maximum at around 1.8 eV below the Fermi energy, which is reproduced in the XPS. However, the spectral feature lying from 4 to 7 eV below the Fermi energy is not reproduced at all by the local spin-density approximation based theoretical calculations. This disagreement is

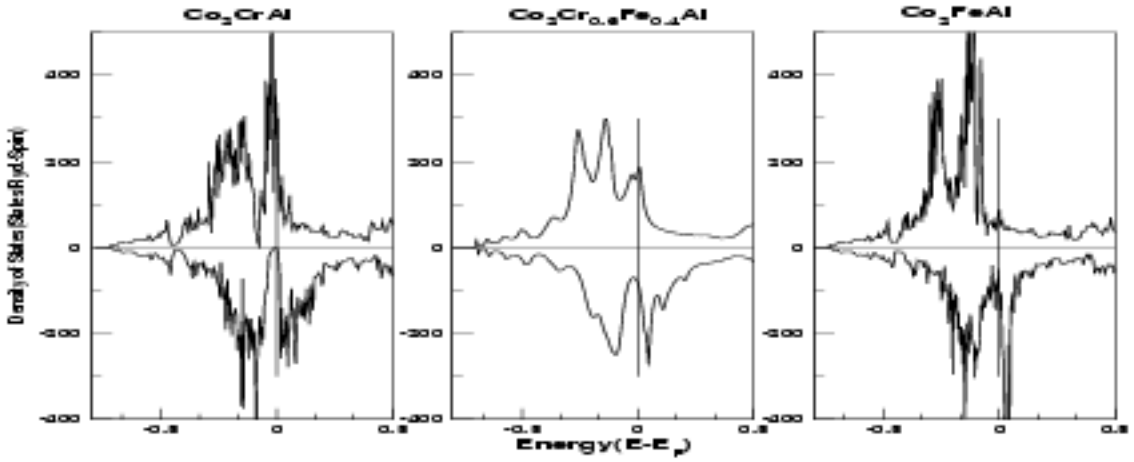

Figure 3.6: Total spin resolved DOS of thin films of Co_2CrAl (left),$Co_2Fe_{0.4}Cr_{0.6}Al$ (centre)and Co_2FeAl (right) . Minority states are shown on a negative scale

qualitatively similar to the earlier work referenced. Earlier works which ignored disorder suggested that disorder could be a factor, however, our work which includes disorder rules this out. We may speculate, with Wurmehl *et al* 2006 that this may point to some deficiencies of the local spin-density approximation.

3.4 Thin film and surface of $Co_2Fe_{0.4}Cr_{0.6}Al$

The methodology we have used to study a (001) nine layered thin film of $Co_2Fe_{0.4}Cr_{0.6}Al$ is same as that of bulk. Here we have carried out a TB-LMTO ASR calculation, to obtain the layer, site as well as orbital (ℓ-m_l) resolved density of states. The recursion method is ideal for application to systems with surfaces. It was originally suggested by Haydock *et al* 1972 precisely for such a problem. With these results at our disposal we have performed a detailed analysis of how charge redistributes itself amongst the various orbitals as a result of alloying in the Cr/Fe site and due to the quasi two dimensional nature of the system. To gain better insight into the effect of disorder we have studied the thin film throughout the concentration range though we will mainly focus at $Co_2Fe_{0.4}Cr_{0.6}Al$.

The total DOS of parent thin films are compared with the $L2_1$ partially disordered

thin film. The spin resolved total DOS for the three cases x = 0,0.4 and 1 are displayed in figure 3.6. The spin resolved total DOS of the thin films resemble their bulk counterparts. Just like the bulk, in thin film also E_F is situated in a valley in the minority spin density of states. It is seen that for x = 0, spin minority band shows a gap in the thin film , but with increase in the Fe concentration first the gap disappears and then for x = 1 it exhibits a sharp dip forming a pseudo gap. Here also we attribute this to the introduction of disorder in the 4*b* site. The contribution from majority density of states at E_F decreases with increase in Fe concentration. This decrease is monotonic in nature and maximum for Co_2FeAl .

The layer resolved DOS are shown in Figure 3.7 . All the three surface states (Al, Fe and Cr) exhibits characteristic surface narrowing due to reduced coordination. The majority surface state of Cr shows a broadening at E_F and is also slightly but importantly shifted towards left, whereas the minority band has almost been pushed out of the E_F , and this is of prime importance, which results in a large increase in the Cr magnetic moment in surface. The majority surface state of Fe does not show much change apart from the fact that the lowest lying peak has broadened out compared to bulk. The structure and height of the minority surface Fe are less developed compared to its bulk counterpart below E_F, whereas above the E_F its structure though prominent, is broadened, left shifted and less sharp than the bulk ones. The layer below the surface layer are occupied by Co and its relative peak width and height have changed with respect to bulk Co. As we move down to the central layers, they start resembling the bulk DOS for all types. This reflects a very important phenomena of electronic structure, that the Local density of states is exponentially insensitive to boundary conditions, i.e., the Heine's Black body theorem. Table-3.2 shows the magnetic moments of Cr , Fe and Co in different sites (layer projected) of the thin film and bulk . We can see that the magnetic moment for the Cr surface state is spectacularly enhanced whereas for the surface Fe , the enhancement is more conservative. The Co magnetic moment below the surface is slightly suppressed compared to its bulk value. From third layer onwards the magnetic moments are more in tune with their bulk counterparts, which is precisely reflected in the layer variation of the DOS.

Since both Co_2FeAl and Co_2CrAl possess a $L2_1$ symmetry and the partially disordered

$Co_2Fe_{0.4}Cr_{0.6}Al$ has also been considered in this phase, owing to the cubic symmetry of the crystal structure the five-fold degenerate d-orbital of the atomic case (because of spherically symmetric coulomb potential prevailing in atoms) has been broken into three fold degenerate t_{2g} orbitals (d_{xy},d_{xz} and d_{yz}) and the two fold degenerate e_g orbitals ($d_{x^2-y^2}$ and d_{3z^2-1}) i.e., the crystal field effect. But for a (001) thin film the z-direction is also rendered inequivalent with respect to x and y direction. This results in further lifting of the degeneracies. Now out of the five d-orbitals only two states still retain their degeneracy (d_{xz} and d_{yz}) as a signature of the remnant planar x-y symmetry of the smooth thin film. In a (001) film the three orbitals have their lobes (d_{xz},d_{yz} and d_{3z^2-1}) pointing towards the vacuum and other two ($d_{x^2-y^2}$ and d_{xy}) have their probability distribution perpendicular to vacuum.

Figure 3.8 shows the spin resolved DOS for constituent d-orbitals of surface Fe (upper panel) and Cr (lower panel) and are compared with their bulk counterparts. Table-3.3 shows the (ℓ-m_l) resolved charges and the resulting magnetic moment for surface and bulk states of Fe and Cr.

The Cr majority d_{xy},d_{xz} and d_{yz} surface states show reduction in peak heights for the lower lying states within E_F whereas the peaks near E_F shows a marked sharpening and are importantly shifted to the left of E_F. The same can be said about the majority d_{3z^2-1} state. For the $d_{x^2-y^2}$ state, its peak near E_F is also shifted towards the left, but not sharp(compared to its bulk). Below E_F all the minority d-states of surface Cr, with the exception of $d_{x^2-y^2}$, are less sharp than corresponding bulk ones, whereas the structure of the DOS are more developed above E_F. The $d_{x^2-y^2}$ state displays an opposite behaviour. Consequently, for Cr each of the majority d-orbitals gain a sizable amount of charge compared to bulk, whereas for minority d-orbitals each of them loses charge, except for a small gain in $d_{x^2-y^2}$ state. This results in a large enhancement in magnetic moment of surface Cr . Since among all the d-orbitals minority state of d_{xy} loses the maximum amount of charge, its enhancement is maximum. The surface enhancement of Cr though remarkable is not surprising, as even for a anti-ferromagnetic thin film of pure Cr , the surface Cr state exhibits similar enhancement.

Unlike Cr at the surface, where the individual d-orbitals participate in surface enhancement, the magnetic moment of the Fe $d_{x^2-y^2}$ orbital is suppressed. The majority

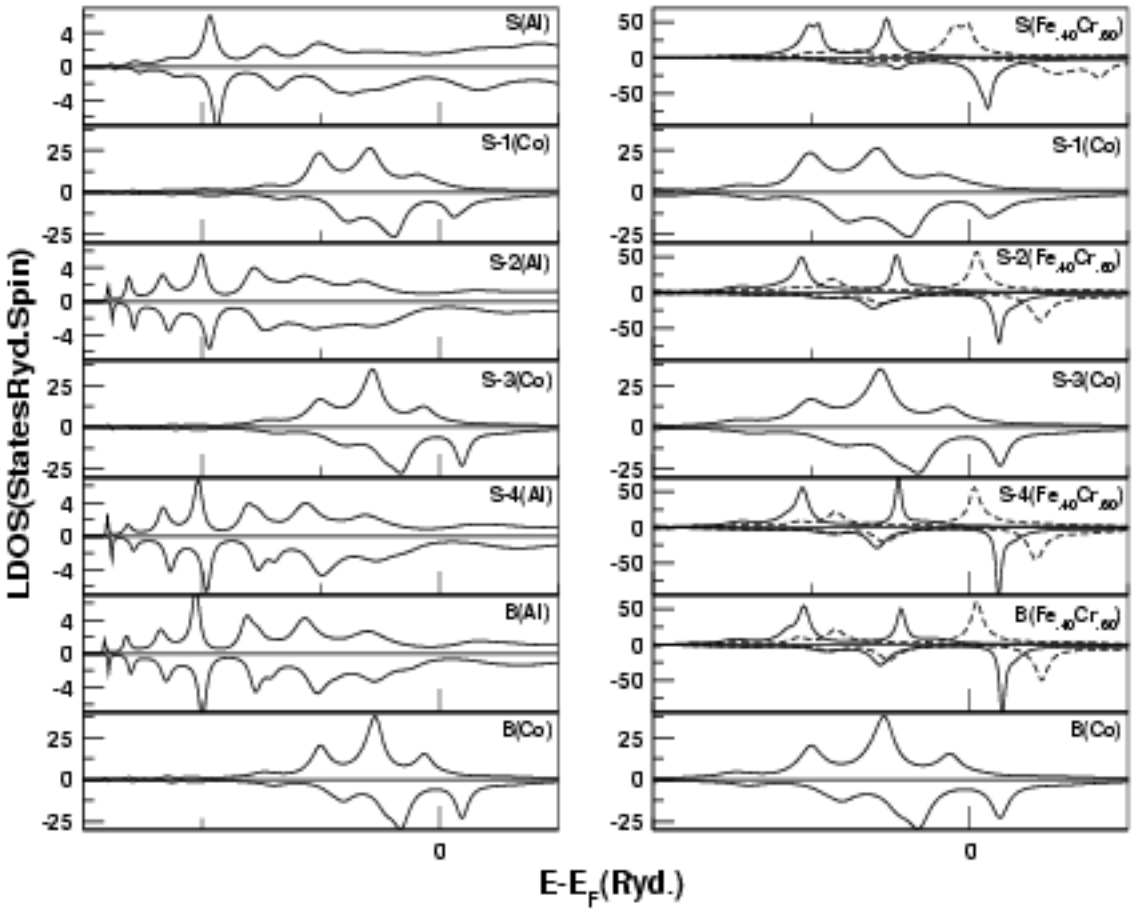

Figure 3.7: Site projected spin and layer resolved DOS of $Co_2Fe_{0.4}Cr_{0.6}Al$ thin film(001). Minority states are shown on a negative scale

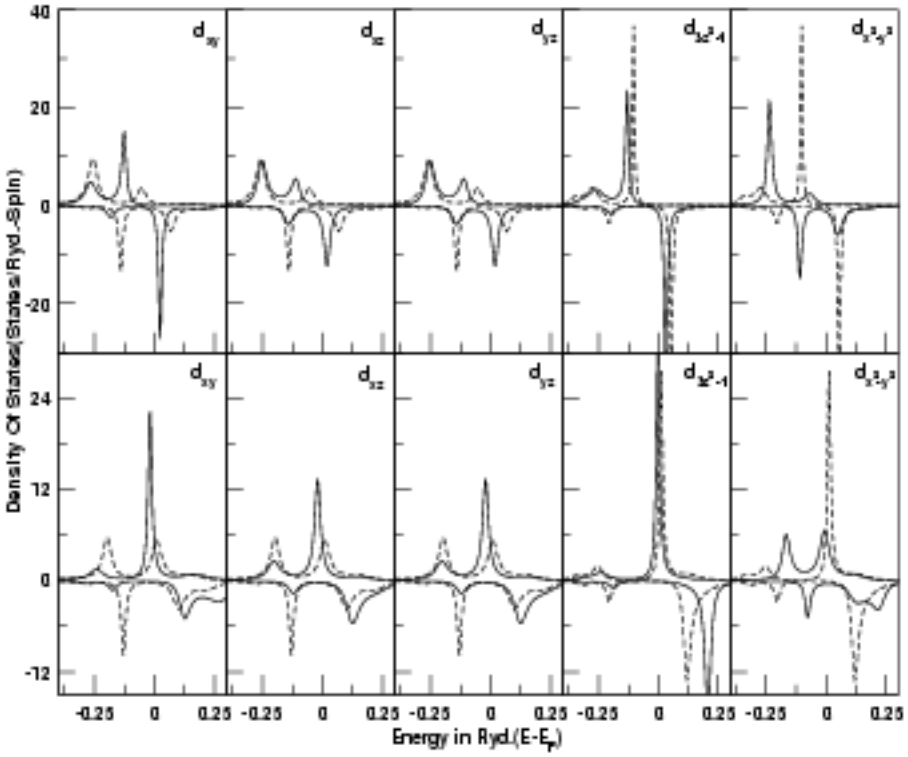

Figure 3.8: Spin resolved DOS of different surface d states of Fe(top row) and Cr(bottom row) in $Co_2Fe_{0.4}Cr_{0.6}Al$ thin film(001). Minority states are shown on a negative scale

	Cr	Fe	Co
S	2.81	2.80	
S-1			0.89
S-2	0.87	2.59	
S-3			1.067
S-4	0.90	2.57	
B	0.97	2.62	1.069

Table 3.2: The magnetic moment of Fe and Cr and Co for different layers of the thin film and Bulk.

band of the $d_{x^2-y^2}$ state of a surface Fe has its peak near E_F substantially reduced. The main role in the magnetic suppression of surface Fe $d_{x^2-y^2}$ state is played by its minority component. The density of states for minority $d_{x^2-y^2}$ state is pushed below E_F with respect to the corresponding bulk state. This results in a gain in charge in the minority state and consequent reduction in the moment of Fe.

The Fe d_{xz} and d_{yz} at the surface share a similar fate by virtue of remnant planar symmetry. Their majority states have their lowest lying peaks within E_F almost at the same position as that of the corresponding bulk state, whereas the peaks near E_F, are shifted to its left, resulting in small charge gain . Their minority states at the surface have their peaks near E_F sharpened, while the lower lying peaks are much reduced , compared to the corresponding bulk states, resulting in small loss of charge compared to the bulk. This in turn results in small moment enhancement for d_{xz} and d_{yz}. The surface d_{3z^2-1} of Fe displays similar changes as the d_{xz} and d_{yz} states, when compared to its bulk, with the exception that its peak height near E_F is less than that of its bulk. As a result its contribution to the surface enhancement is less than d_{xz} and d_{yz} states.

The major contribution to the surface enhancement of Fe comes from the d_{xy} state. The reason for this is that its minority band is almost pushed out of E_F(i.e., to its right). In the majority band the structure near E_F is relatively well developed(i.e., compared to its bulk state) among all the d-states of surface Fe atoms. It is because of the d_{xy} state, that there is an enhancement in moment of surface Fe, despite moment suppression in the $d_{x^2-y^2}$ state at the surface.

Figure 3.9 shows the surface states of Fe and Cr for different concentrations of $Co_2Fe_xCr_{1-x}Al$

Surface

m_l	Charge		Mom.	Charge		Mom.
	Cr ↑	Cr ↓	Cr	Fe ↑	Fe ↓	Fe
s	0.238	0.225	0.014	0.301	0.285	0.016
p_x	0.082	0.084	-0.002	0.107	0.103	0.004
p_y	0.082	0.084	-0.002	0.107	0.103	0.004
p_z	0.048	0.05	-0.002	0.059	0.057	0.002
d_{xy}	0.720	0.11	0.61	0.94	0.285	0.654
d_{yz}	0.725	0.147	0.578	0.925	0.464	0.461
d_{xz}	0.725	0.147	0.578	0.925	0.464	0.461
d_{3z^2-1}	0.678	0.084	0.594	0.972	0.185	0.787
$d_{x^2-y^2}$	0.654	0.211	0.443	0.913	0.508	0.405

Bulk

m_l	Charge		Mom.	Charge		Mom.
	Cr ↑	Cr ↓	Cr	Fe ↑	Fe ↓	Fe
s	0.294	0.299	-0.005	0.347	0.345	0.002
p_x	0.123	0.132	-0.009	0.145	0.153	-0.008
p_y	0.123	0.132	-0.009	0.145	0.153	-0.008
p_z	0.123	0.132	-0.009	0.145	0.153	-0.008
d_{xy}	0.572	0.392	0.180	0.892	0.500	0.392
d_{yz}	0.572	0.392	0.180	0.892	0.500	0.392
d_{xz}	0.572	0.392	0.180	0.892	0.500	0.392
d_{3z^2-1}	0.414	0.182	0.232	0.959	0.228	0.731
$d_{x^2-y^2}$	0.414	0.182	0.232	0.959	0.228	0.731

Table 3.3: The orbital (ℓ-m_l) resolved Fe and Cr projected charges and corresponding magnetic moment for surface and bulk states

thin films. The disordered surface states of both Fe and Cr are broader compared to their ordered counterparts, an obvious effect of disorder. The lowest lying structure in majority Fe surface is basically composed of two peaks and they get better resolved with increase in Fe concentration. In the Minority Fe surface state the peak lying right of E_F suffers a slight shift to the right and also sharpens as the Fe concentration increases. This is responsible for the increase in Fe surface magnetic moment with the increase in Fe concentration. The main structure of Cr surface state(in the majority band) in $Co_2Fe_xCr_{1-x}Al$ thin films

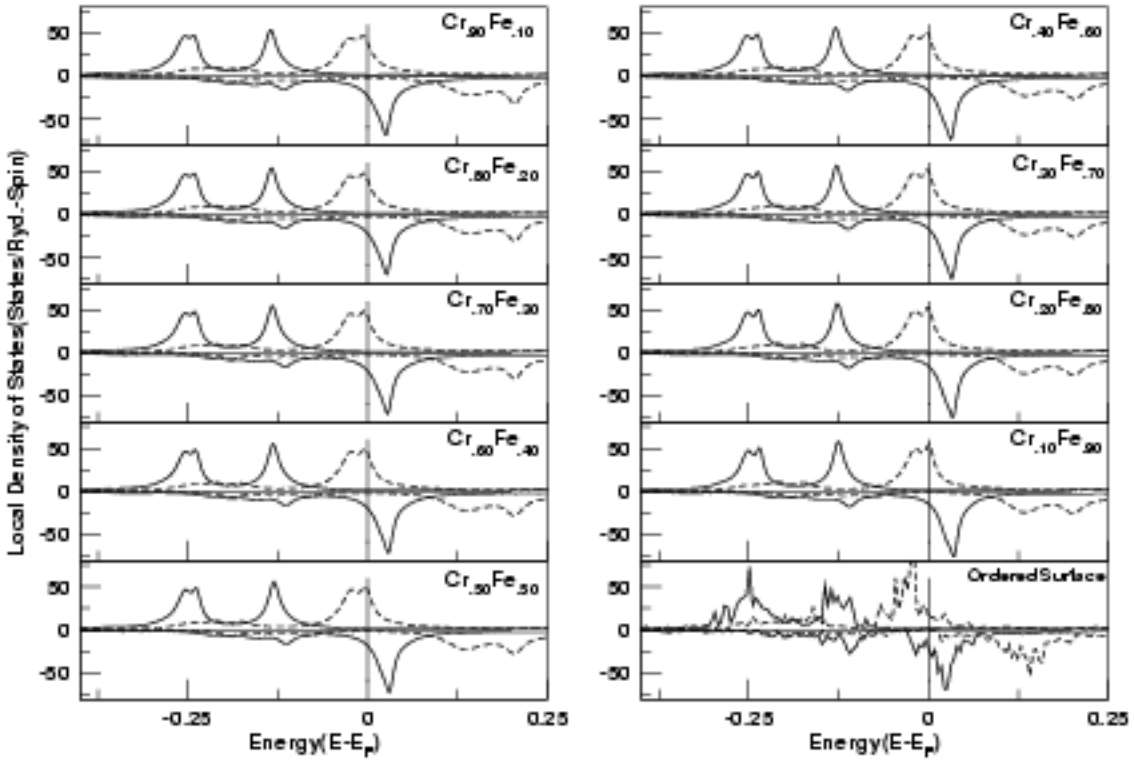

Figure 3.9: Spin resolved DOS of Surface Fe (solid line) and Cr (broken line) states of $Co_2Fe_xCr_{1-x}Al$ as function of concentration of Fe and Cr . The DOS in the bottom of the right panel are the surface states of Fe and Cr for the thin films of $Co_2Fe_{0.4}Cr_{0.6}Al$ and Co_2CrAl respectively. Minority states are shown on a negative scale

at E_F suffers a slight shift towards the right of E_F with increase in Fe concentration. This explains for the slow decrease in surface Cr magnetic moment with increase in Fe concentration. The minority Cr surface states are always pinned at E_F. Figure3.10 shows the magnetic moment of Fe and Cr surface states as a function of Fe concentration. Although the surface enhancement of Fe atom are not much compared to its bulk moment, but it increases with increase in Fe concentration.Cr surface magnetization though highly enhanced compared to its bulk, follows a similar trend as far as its variation with disorder is concerned.

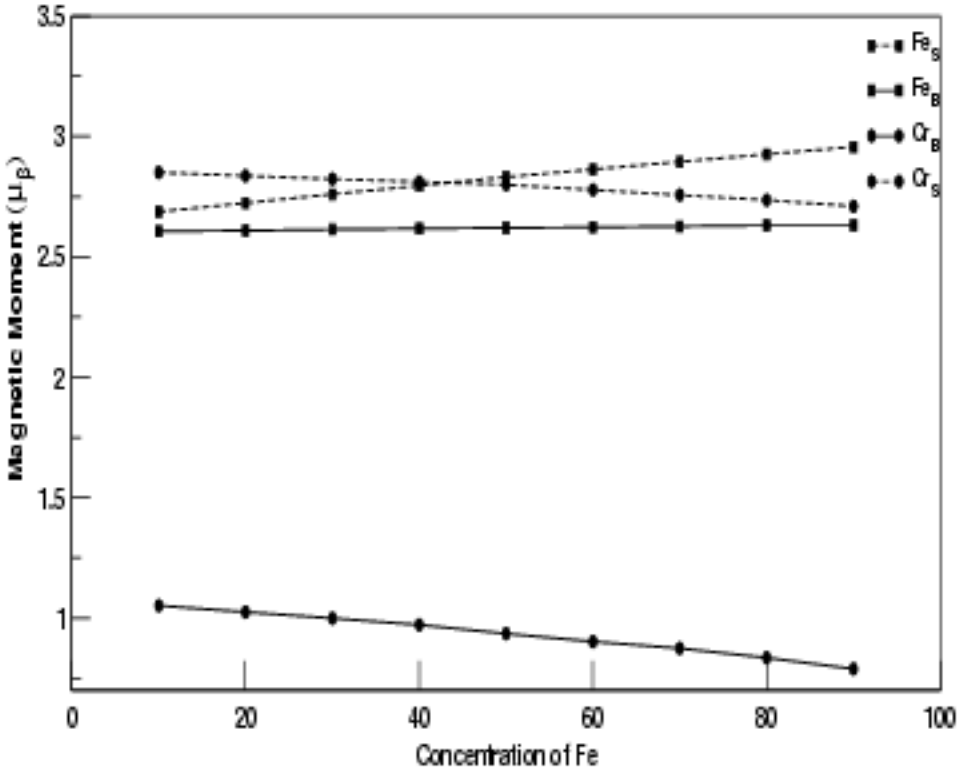

Figure 3.10: Magnetic moment of surface (broken line) and bulk (solid line) Fe and Cr of $Co_2Fe_xCr_{1-x}Al$ as function of concentration of Fe.

3.5 Summary and Conclusion

We have presented here a version of the TB-LMTO based augmented space recursion technique, modified to include systems with many atoms per unit cell and disorder only in one specific lattice site in the basis. We have shown that the technique is ideally suited to describe the doped quaternary-Heusler alloy system, both in the bulk as well as in thin films(001). We examine the local, component projected magnetic moments, which we believe are sensitively dependent on the accuracy with which we can describe the chemical environment of a component atom. Our predictions agree well with experiment

and qualitatively with earlier work. This is with the exception of the gross over-estimation of the Cr moment for all disorder compositions. All earlier work also overestimated the Cr moment quantitatively as much as ours. The question arises, do we understand why this is so ?

Miura *et al* 2004 studied the effect of disorder in the Al and Co sites on the behaviour of $Co_2Fe_xCr_{1-x}Al$. They found that disorder between Cr and Al hardly changes matters, while the disorder between Cr and Co leads to a large decrease in the Cr moment. However Antonov *et al* 2005 argue that such disorder is highly unlikely energetically. That leaves us without a reasonable explanation for the large overestimation of Cr moment. It seems from our work that this discrepancy cannot lie at the door of the type of electronic structure method used (KKR or LMTO) or the method used to deal with the partial disorder (CPA, super-cell or ASR).

We speculate that this overestimation may be either due to the use of the Density Functional approximation which cannot take into account correlation in the localized *d*-states of the constituents properly. Alternatively, one should examine the experimental data in some more detail to determine if sub-lattice disorder does exist because of the way the alloys have been prepared. In thin films, the surface Cr projected state exhibits a huge enhancement, whose magnitude decreases slightly with increase in Fe concentration in the thin film. The enhancement in the surface Fe projected state is much more conservative, but it shows a slight increase with the increase in Fe concentration. Our orbital resolved approach enables us to extract the detailed information about role of individual orbitals(ℓ-m_l-m_s) in the surface enhancement of Fe and Cr surface states.

Chapter 4

Electron-Phonon interaction in ground state: a real space study

4.1 Introduction

The physics of polarons has generated immense interest as the electron-phonon interaction play a pivotal role in many areas of condensed matter physics like, the manganites, a strongly correlated electronic material, exhibiting colossal magneto-resistance (Jaime *et al* 1997, Ramirez 1997), the organics (Campbell and Smith 2001) , and the high T_c superconducting cuprates (Baryam *et al* 1992, Alexandrov and Mott 1994). The theoretical studies of polarons has been a challenging area of research over the decades, as it involves the complex many-body interactions between the electronic and the lattice degrees of freedom (phonons).

The Holstein model (Holstein 1959) over the decades has been a paradigm, to understand the polaron problem. This relatively simple model captures the intricate physics of electron-phonon elegantly. This is the reason that its importance hasn't waned even after six decades of its inception.

Analytical approaches like the standard perturbation treatments (Alexandrov and Mott 1995) have been successful in weak and strong coupling regimes. They have problems in the intermediate coupling regime where both strong and weak coupling perturbation theory break down. Because of this inherent inadequacy of the analytic approach and huge development in computational facilities, different groups have tried to understand the problem using numerical tools, which includes the variational approach based on exact

diagonalization method (VAED) (Bonca *et al* 1999, Li-Chung *et al* 2002), the density-matrix renormalization group techniques (DMRG) (Jeckelmann and White 1998), exact diagonalization techniques (ED) (Alexandrov *et al* 1994, Wellien *et al* 1996, Wellien and Fehske 1997, Wellien and Fehske 1998, de Mello and Ranninger 1997, Capone *et al* 1997, Marsiglio 1995), the quantum Monte Carlo calculations (QMC) (De Raedt and Langedijk 1982, Kornilovitch and Pike 1997) and global-local method (Romero *et al* 1998). None of these methods work equally well in all parametric regimes. Each has some shortcomings. VAED, the most recent and successful of the methods, though highly accurate in the weak and intermediate coupling regimes, fails to maintain its accuracy in the strong coupling limit. The DMRG method is accurate in the strong and intermediate coupling regimes, but is not accurate in the weak coupling regime. But their effort has been fruitful as the physically interesting, intermediate coupling regime, where analytic approaches fails, is now more well understood.

Our group has extrapolated the ideas of VAED using augmented space approach to include more phonon rich states which enables us to scan the entire parametric space of the 1-d Holstein Model. The augmented space approach not only overcomes the inadequacies of earlier numerical studies in ordered 1-D Holstein model but this has been generalized to study quenched random disorder. This is a reciprocal space based method and uses lattice translational symmetry. This is adequate for dealing with ordered (translationally invariant) and homogeneous disordered (where occupation probability is site independent) systems(Chakrabarti *et al* 2006). But to deal with system which does not possess translational symmetry in its site occupation or where the disorder is inhomogeneous (example in defects, thin films and topological disorder), one has to take recourse to a real space based method.

In this chapter we will describe how we construct a real space basis using the idea of augmented space(Mookerjee 1973). Then we shall obtain the ground state energy and wave-function using recursion based conjugate-gradient technique(Viswanath and Müller 1993). Our calculations are highly accurate in 1-d and compare well with the k-space results. With increase in dimension the, numerical accuracy is not as good as in 1-d. For 2-d we have at least 5-6 and for 3-d, at least 4-5 digit energy accuracy. We have also applied our scheme to study the effect of electron-phonon interaction in a chemically

alternating 1-d periodic lattice. We will also present our numerical study for a tri-layered thin film (100), a system where translational symmetry is lost (in the z-direction).

4.2 The Augmented Space Formalism

In this section we shall describe the setting up of the electron-phonon Hamiltonian as an operator on the underlying Hilbert space. The electronic part will be represented in a tight-binding basis. In our simple model there will be only a single orbital per site and the tight-binding basis will be labelled by a site R. This basis will span the electronic part of the Hilbert space $\mathcal{H}^{el}$. The phonon part will be described by a *configuration state* which will indicate how many phonon excitations there are at each *site* labelled by R. Each *configuration* will be a pattern of the type $\{n_{R_1}, n_{R_2} \ldots n_{R_n} \ldots\}$ where n_{R_n} takes the values $0, 1, 2, \ldots$ and is called the *cardinality* of the site R_n. The pattern is called the *cardinality sequence* and uniquely labels a phonon state. These states will span the phononic part of the Hilbert space $\mathcal{H}^{ph}$. The total Hilbert space of states of the electron-phonon system will be $\mathcal{H} = \mathcal{H}^{el} \otimes \mathcal{H}^{ph}$. A member of the basis in this direct product space will be labelled *both* by the site labelled real-space part and a configuration part which tells us how many local phononic excitations are there at each site in the lattice, e.g. $|R_n \otimes \{n_{R_1}, n_{R_2}, \ldots\}\rangle$.

4.2.1 The Holstein Hamiltonian

In this basis, the Holstein Hamiltonian (Holstein 1959) is :

$$\begin{aligned} \mathbf{H} &= \sum_{R_n} \epsilon_n \mathbf{P}_n \otimes \mathbf{I} - t \sum_{R_n} \sum_{R_m} \mathbf{T}_{nm} \otimes \mathbf{I} + \hbar\omega \sum_{R_n} \mathbf{I} \otimes \mathrm{N}_n \\ &\quad - \lambda \sum_{R_n} \mathbf{P}_n \otimes \left(\mathbf{T}_n^+ + \mathbf{T}_n^-\right) \end{aligned} \tag{4.1}$$

- $\mathbf{P}_n$ is the projection operator $|R_n\rangle\langle R_n|$ for the electron.
- $\mathbf{T}_{nm} = |R_n\rangle\langle R_m|$ is the transfer operator in the electronic part of the Hilbert space $\mathcal{H}^{el}$.

- $\mathbf{T}_n^{\pm} = |\ldots n_{R_n} \pm 1 \ldots\rangle\langle\ldots n_{R_n} \ldots|$ are the step up or step down operator which creates or destroys phonons respectively. This operator acts on the phononic part of the Hilbert space $\mathcal{H}^{ph}$.

- N_n is the number operator $n_{R_n}|\ldots n_{R_n} \ldots\rangle\langle\ldots n_{R_n} \ldots|$ also acts on the phononic part of the Hilbert space $\mathcal{H}^{ph}$.

- In all subsequent calculations the site energy ε_n is set to zero(if not otherwise mentioned) and t the hopping strength is taken as 1.

- ω is frequency of the dispersion-less optical phonons.

- λ denotes the strength of the electron-phonon coupling.

- The parameters ε_n,t, $\hbar\omega$ and λ have the units of energy.

This type of Hamiltonian in an augmented space $\mathcal{H}^{el} \otimes \mathcal{H}^{ph}$ has been introduced earlier by us (Mookerjee 1990) to deal with time dependent disorder in an electronic system, precisely of the form produced by lattice vibrations. The advantage of this formulation is that if we have quenched disorder in $\varepsilon(R_n)$, then a simple augmentation of the Hilbert space $\mathcal{H}^{el}$ by the configuration space of the $\varepsilon(R_n)$ allows one to deal with all the configuration averaged properties of a disordered Holstein model. This extension has been carried out by Chakrabarti *et al* 2006. As mentioned earlier the Holstein model for both the case of ordered as well as quenched disorder has been carried out in reciprocal space. Here our aim is to use this technique in real space.

4.3 Results

We have obtained the ground state of the different Holstein system by applying the recursive conjugate gradient method(Viswanath and Müller 1993). First we have generated the basis states by repeated application of the Holstein Hamiltonian on the initial states. The initial states are of two types.
(1) The initial state consists of all the lattice sites of the system, with no phonon anywhere.

(2) The initial state consists of all the lattice sites of the system with no phonon anywhere as well as all the lattice sites with say $N1$ number of phonon at each of the lattice sites.

Now, suppose we operate the Hamiltonian N times on the initial state of the first kind, then the maximum number of phonons a state can have at its real space site is N and it will also have states which has at least one phonon at a distance N (if we consider the lattice spacing to be 1) from its real space site. If we act the Hamiltonian N times on the initial state of second kind, than maximum number of phonons a state can have at its real space site is $(N1 + N)$. The second kind of basis helps us to generate a phonon-rich basis which in turn helps us to get the accurate ground state in the high electron-phonon coupling regime.

With the ground state wave-function at our disposal, we have calculated different correlation functions to have a better insight about the effect of electron-phonon interaction in different parametric regimes. The correlation functions that we have calculated are:

The mean ground state(Gr) phonon number, which gives us a measure of the phononic character of the polaron in the ground state is given by

$$N^{ph}_{Gr} = \langle \psi_{Gr} | \mathbf{I} \otimes \mathrm{N_n} | \psi_{Gr} \rangle \tag{4.2}$$

The static correlation function between the electron position and oscillator displacement, which captures the amount of polaronic distortion is given by

$$\chi(\mathbf{R_i} - \mathbf{R_j}) = \langle \psi_{Gr} | \mathbf{P}_i \otimes (\mathbf{T}^+_j + \mathbf{T}^-_j) | \psi_{Gr} \rangle \tag{4.3}$$

The number of excited phonons in the vicinity of the electron is given by

$$\gamma(\mathbf{R_i} - \mathbf{R_j}) = \langle \psi_{Gr} | \mathbf{P}_i \otimes \mathrm{N}_j | \psi_{Gr} \rangle \tag{4.4}$$

4.3.1 Chemically Uniform 1-dimensional Holstein Model

To study the 1-dimensional (1-d) Holstein model we have taken a 1-d periodic lattice with 30 sites. Here we have generated the basis states of second type applying the Hamiltonian 15 times (Nh=15). Here $N1 = 15$, therefore the maximum number of phonon generated at

each electron site is 30. To check the convergence of our results in real space we have also generated a basis state on a 1-d periodic lattice with 28 sites and applied the Hamiltonian 14 times (Nh=14) on the initial state of second kind, thus ensuring maximum number of phonon generated at each electron site is 29. Table-4.1 lists the ground state energy of the 1-dimensional polaron calculated previously and compares with our real-space calculation. Our ground state energy shows an excellent matching with the calculated energies of Chakrabarti *et al* 2006 and Bonca *et al* 1999. The translational symmetry of the system is reflected in the fact that the site projected probability of the ground state wave function is uniform for all sites (i.e. 1/30).

λ/ω	1.0	$\sqrt{2}$
Present (Nh=15)	-2.46968472393	-2.9988281868
Present (Nh=14)	-2.4696847239	-2.998828186
Chakrabarti *et al* 2006	-2.469684723933	-2.998828186866
Bonca *et al* 1999	-2.469684723933	-2.99882818686
DMRG	-2.46968	-2.99883

Table 4.1: Comparison of Polaron Ground state energy for for two different set

We have calculated the static correlation function $\chi(\mathbf{R_i} - \mathbf{R_j})$ between the electron position and quanta of lattice vibration which gives us a measure of the electron-induced lattice deformation and its spatial extent.We compare our results with Chakrabarti *et al* 2006 for all parameters, with Bonca *et al* 1999 for low and intermediate electron-phonon coupling regime and with Jeckelmann and White 1998 for the strong electron-phonon coupling results. There is excellent agreement between our results and that of Bonca *et al* 1999 and Chakrabarti *et al* 2006 , for ω=0.1 (adiabatic) and λ=0.1 (weak coupling),which is shown in Figure 4.1 (a) . We can clearly see spatial extent of the polaron span the system size, therefore a large polaron. We have not shown the DMRG result for this parameter, as it is less reliable for the large polaron, since there calculation is done on lattice size of 20, which is clearly smaller than the spatial extent of the polaron.In Figure 4.1 (b) we show the χ for ω=1.0 and λ=0.5, which again matches well with both the previous results. Figure 4.1 (c) and Figure 4.1 (d) shows the χ for high electron-phonon coupling in adiabatic ω/t=0.1 (λ=4.35) and intermediate ω/t=1.0 (λ=3.0) limits. In both the cases the size of the polaron is very small i.e., small polaron has formed as a result of

electron-phonon coupling. The electron-phonon interaction almost limits the size of the polaronic distortion to the electron or the lattice site. Here we have achieved excellent agreement with both DMRG (Jeckelmann and White 1998) results and with Chakrabarti *et al* 2006. The value of our extracted DMRG χ (0) is 5.459016, the value of Chakrabarti *et al* 2006 for this is 5.374 and the value of our calculation is 5.39, which is very close to 5.4 the lower limit of extrapolated VAED data. In Figure4.1 (d), we also have a good agreement with DMRG results. Value of our χ (0) is 5.9126, that of Chakrabarti *et al* 2006 is 5.9128 and value of the DMRG extracted data is 5.725490. Unlike DMRG results , our results are reflection symmetric (i.e.,χ (1)=χ (-1)), as this basis takes proper care of reflection symmetry. We conclude that even in real space we could emulate the success of k-space based calculations of Chakrabarti *et al* 2006, for all the regimes.

We now turn our attention to the distribution of the excited phonons in the vicinity of the electron site $\gamma(R_i - R_j)$, for different parameters, which is shown in Figure 4.2. The extent of distribution of the excited phonon about the electron site varies with respect to the oscillator frequency and the electron-phonon coupling strength. But one noticeable feature of the phonon distribution in comparison with its corresponding static correlation function $\chi(\mathbf{R_i} - \mathbf{R_j})$, is that, its falls is faster, which signifies that the polaronic distortion is larger that its excited phonon distribution. In Figure 4.2 (b) we compare our real space calculation with the reciprocal-space results of Chakrabarti *et al* 2006, and there is an excellent matching of the reciprocal space and real space result.

We have also calculated the correlation functions χ (0), χ (1), (χ (0)-χ (1))/g which is shown in Figure 4.3 and they are compared with the corresponding reciprocal-space results of Chakrabarti *et al* 2006. The results of real space calculations for the ground state matches exactly with the reciprocal-space results throughout the electron-phonon coupling regime for all the three oscillator frequencies. Here, g is λ/ω. χ (0) has a non-linear behaviour in the intermediate electron-phonon coupling regime. It is linear w.r.t g both in the low and high electron-phonon coupling regime and this trend is there in all limits (i.e., for different ω). But slope of χ (0) in the low electron-phonon coupling regime depends on ω but its slope in high electron-phonon coupling regime becomes independent of ω and its value approaches 2. But the change in slope of χ (0) as we go from low to high

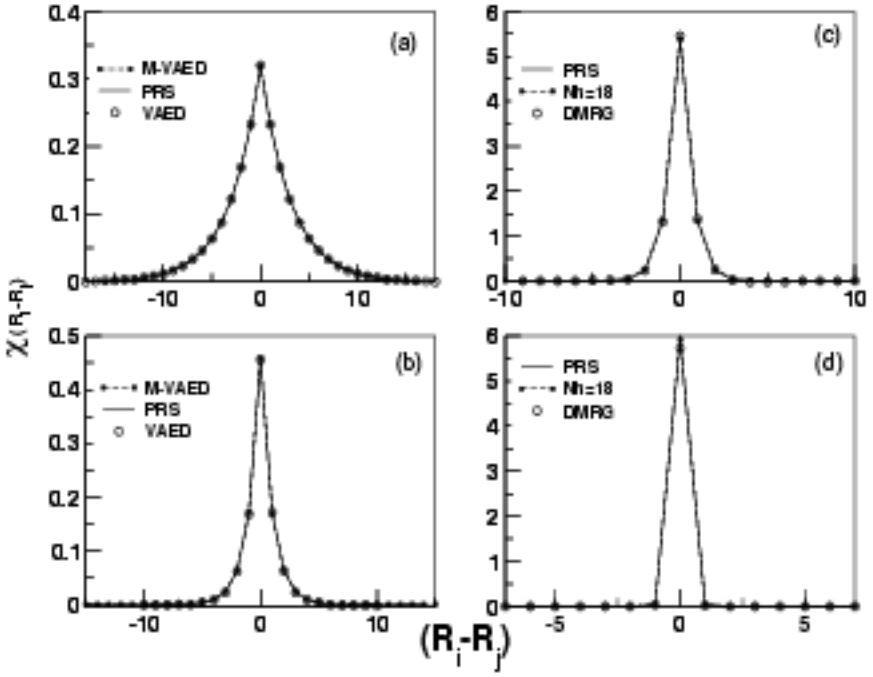

Figure 4.1: The Lattice deformation $\chi(\mathbf{R}_i - \mathbf{R}_j)$ as function of $\mathbf{R}_i - \mathbf{R}_j$ in the ground state for (a) ω=0.1 andλ=0.1, (b)ω=1.0 and λ=0.5, (c)ω=0.1 andλ=0.435, (d)ω=1.0 and λ=3.0 Here the Present Real Space results are mentioned as PRS in abbreviation. VAED are the extracted results of Bonca *et al* 1999 and M-VAED is the phonon rich basis results of Chakrabarti *et al* 2006. DMRG are the results Jeckelmann and White 1998.

g, is more prominent for lower values of ω. χ (1) increases linearly to start with (i.e., low g regime), then its rate of increment decreases and then it starts decreasing, signalling the arrival of high electron-phonon coupling regime. The decrement in χ (1) w.r.t to g and the corresponding change in χ (0) implies that, from this g onward the lattice distortion starts getting confined to the electron site. The correlation function (χ (0)-χ (1))/g substantiates these facts. It always saturates to a value 2 for high g regime. For ω=0.1 we have not gone to that magnitude of g where $(\chi(0) - \chi(1))/g$ would saturate to 2, but the trend is quite clear. For lower values of ω the cross-over is rather sharp, which is also reflected in the Average phonon number and average kinetic energy calculations

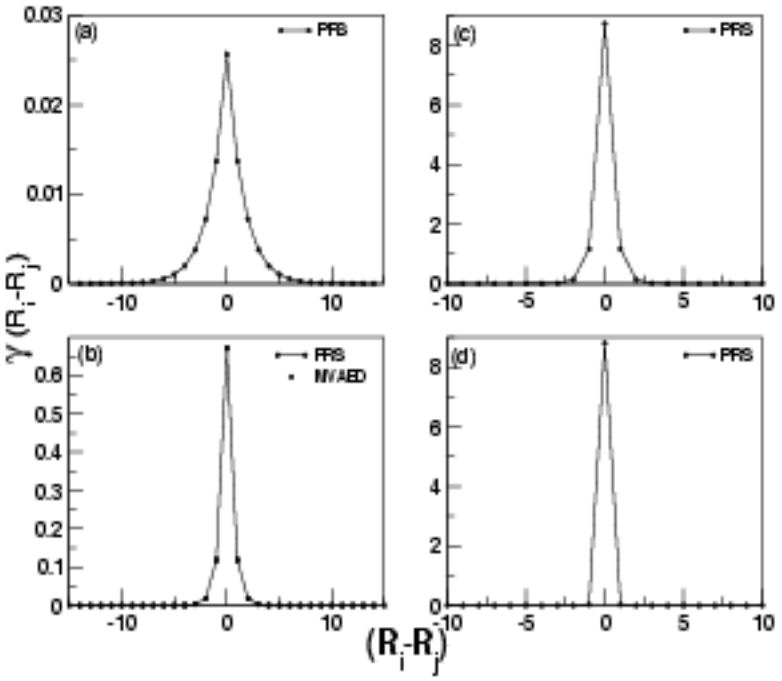

Figure 4.2: The excited phonon distribution in the vicinity of electrons $\gamma(\mathbf{R}_i - \mathbf{R}_j)$ as function of $\mathbf{R}_i - \mathbf{R}_j$ in the ground state for (a) ω=0.1 andλ=0.1, (b)ω=0.5 and λ=0.9, (c)ω=0.1 andλ=0.435, (d)ω=1.0 and λ=3.0 . Here the Present Real Space results are mentioned as PRS in abbreviation.M-VAED is the phonon rich basis results of Chakrabarti *et al* 2006

Figure 4.4 (broken lines (PRS)).

4.3.2 Chemically alternating 1-dimensional Holstein Model

In this section we will discuss the electron-phonon interaction in a 30 site periodic 1-d Ordered Holstein model, with alternate sites having energies $\varepsilon_a(=0)$ and $\varepsilon_b(=\varepsilon_a + \delta\varepsilon)$. Here also the basis states are generated by applying the Hamiltonian 15 times (i.e., Nh=15) on the initial states of second kind, thus each site has at the maximum 30 phonons at its own site. Chatterjee and Das 2005 had done an analytic perturbative study with the variational modified Lang-Firsov phonon basis for two sites with different

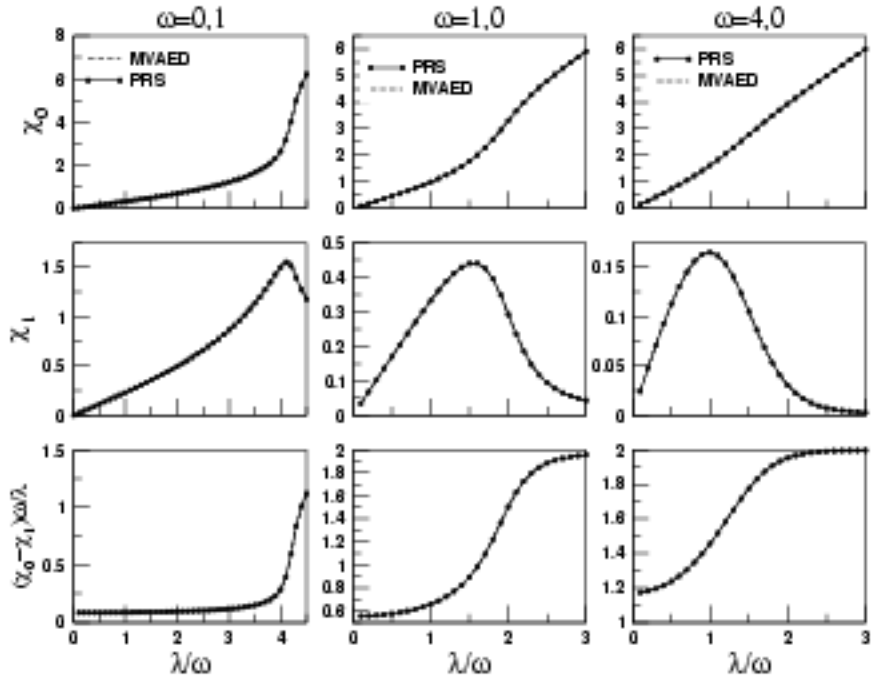

Figure 4.3: Figures in the upper row shows the χ (0) at three different ω. Middle row is for χ (1). Lower row is for (χ (0)-χ (1))/g. The solid lines with dot are the present real space calculation (PRS) and broken lines are the results of Chakrabarti *et al* 2006 using their modified basis of 19-shell.

energies. They had also incorporated spin degrees of freedom of the electron, but we will study the electron-phonon interaction for the spin-less case. Here most noticeable change which occurs due to difference in site energies of the alternating sites, is that the uniform site projected probabilities of the previous case (i.e., $\delta\varepsilon = 0$), now shows a periodic variation. The site projected probability of both the cases is shown in Fig4.5. Here, for the alternating case, $\varepsilon_a = 0$ and $\varepsilon_b = 1$, and both the calculations are done at $\omega = 1.0$ and $\lambda = 1.0$.

To show the effect of alternating site energies on the electron-phonon interaction we will take a two-pronged approach, first we will vary the electron-phonon coupling keeping the site energies fixed at particular oscillator frequencies and then we will vary the difference in site energies (i.e., $\delta\varepsilon$) at fixed values of electron-phonon coupling and oscillator frequencies.

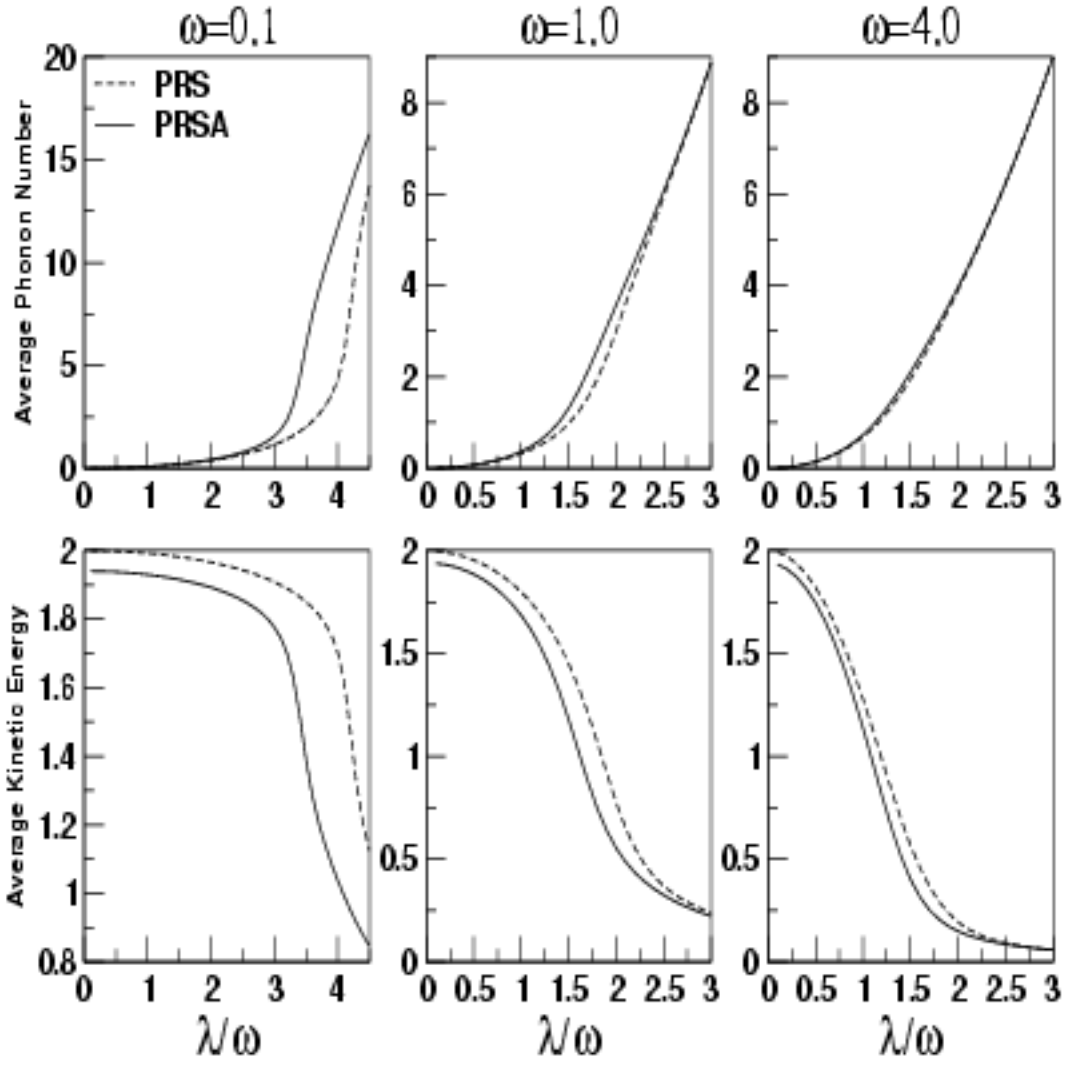

Figure 4.4: Figures in the upper row shows the ground state averaged phonon number at three different ω. Lower row is for ground state averaged kinetic Energy. The solid line are for lattice with alternating site energies (PRSA) and broken line are for lattice with uniform site energies (PRS)

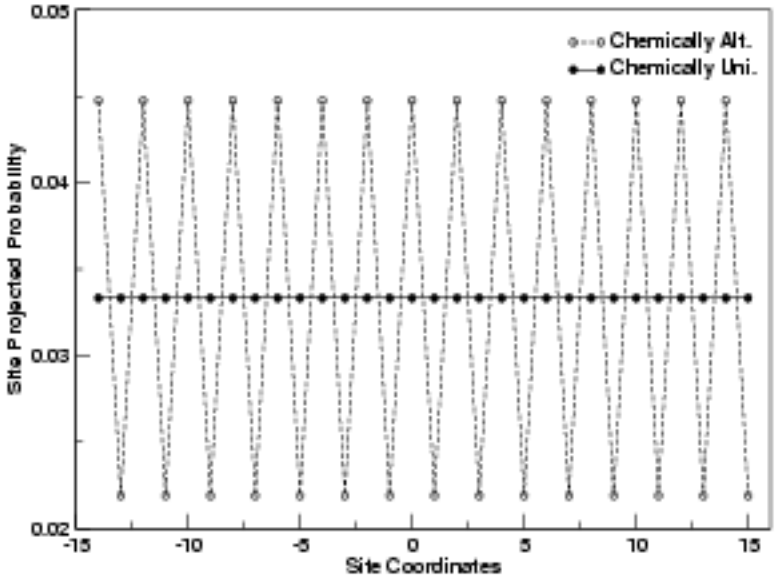

Figure 4.5: The site projected probability for 1-d Holstein model and a chemically alternating 1-d Holstein model.Both the calculations are done at $\omega = 1.0$ and $\lambda = 1.0$.

Figure 4.6 shows how the probabilities of the sites with different site energies ($\delta\epsilon = 1.0$) evolve with the electron-phonon coupling constant for three different oscillator frequencies (i.e., in three limits: adiabatic, intermediate and anti-adiabatic). At low and high electron-phonon coupling the variation of the site projected probabilities with respect to electron-phonon coupling constant is almost constant but their behaviour in the intermediate coupling is non-linear. The change in the probability profile in going from low to high electron-phonon coupling regime i.e., at the intermediate coupling regime, is sharper for the adiabatic case ($\omega = 0.1$). In the strong electron-phonon coupling regime the site with larger site energy (i.e., ϵ_b) has been almost stripped off (i.e., almost zero occupation probability). There is almost a total flow of probability from higher energy site to lower energy site. For $\omega = 0.1$, we should have gone further to achieve the probability saturation, but that would demand more phonon rich states, but the trend is quite clear.

Figure 4.7 shows the polaronic distortion at the electronic site $\chi(0)$ and at its nearest neighbour site $\chi(1)$ and their differences $(\chi(0) - \chi(1))/g$ for the chemically alter-

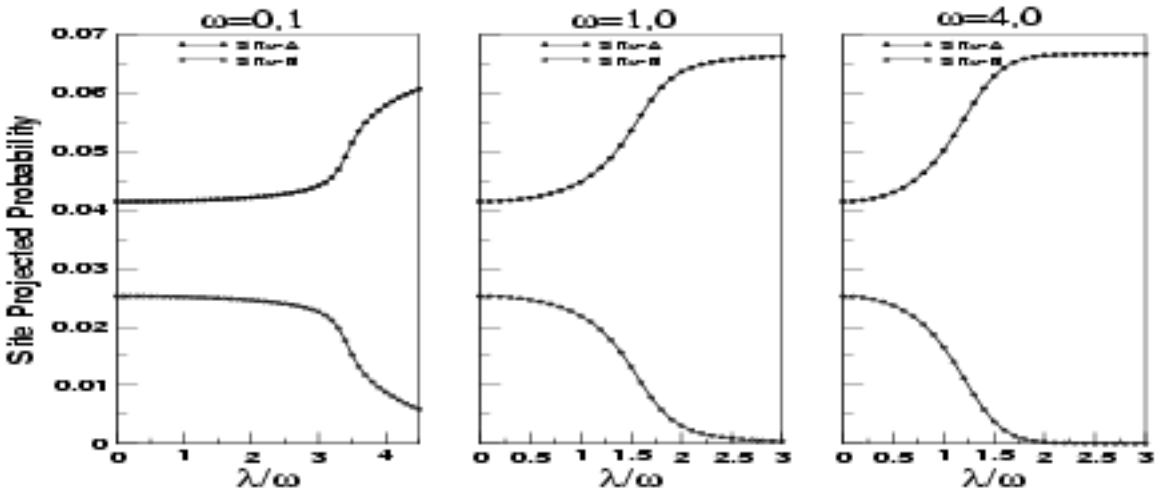

Figure 4.6: The site projected probability of a chemically alternating 1-d Holstein model at different Oscillator frequencies as a function of the electron-phonon coupling constant. Here $\delta\epsilon = 1$ for all the cases

nating lattice ($\delta\epsilon = 0$) and has been compared with their chemically uniform counterpart. The behaviour of the χ are quite similar for both types of lattice for very low and high electron-phonon coupling, it is the intermediate coupling where the two types of lattice deviates from each other. Though it is not very evident from the figure (small differences in values are not so well resolved, because y-axis spans a large region), the values of $\chi(0)$ of the alternating lattice are slightly higher and those of $\chi(1)$ slightly lower than the uniform lattice for weak electron-phonon coupling. Here a comparison with the results of disordered Holstein model (Chakrabarti *et al* 2006) is very important. This had been carried out at these frequencies up to the intermediate electron-phonon coupling. There they had considered a quenched binary disorder between species with $\epsilon_a = 0$ and $\epsilon_b = 1.0$. Figure 4.8 shows this comparison up to the electron-phonon coupling carried out by Chakrabarti *et al* 2006. The effect of disorder is most prominent in the adiabatic limit. In fact at lower values of g (less than 2.2) $\chi(0)$ for disordered lattice is slightly more than alternating and the uniform lattice, above which the value of alternating lattice overtakes the disordered one (this variation is not so clear from Figure 4.8 as the variation is indeed very small). The values of disordered $\chi(1)$ is larger than the other two, throughout the range of the

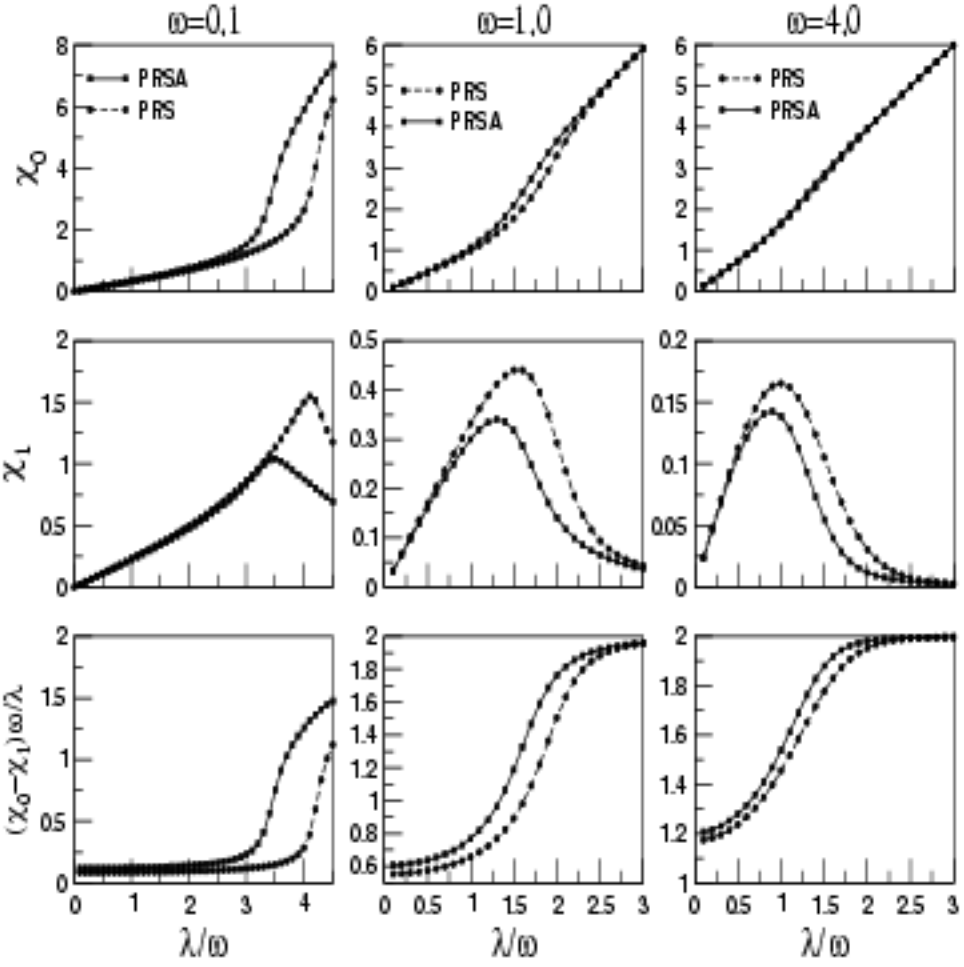

Figure 4.7: Figures in the upper row shows the χ (0) at three different ω for the chemically alternating 1-d lattice compared with the chemically uniform lattice . Middle row is for χ (1). Lower row is for (χ (0)-χ (1))/g. The solid lines with squares are the present real space calculation (PRSA) for the chemically alternating case and broken lines with circles are the results of chemically uniform case (PRS).

calculation. $\chi(1)$ values of the alternating lattice is lower than the other two. However in the intermediate ($\omega = 1.0$) and anti-adiabatic ($\omega = 4.0$) limit the disorder scattering hardly does anything to change the scenario from the uniform case, as far as the electron-phonon interaction induced lattice distortion (i.e., in $\chi(0)$ and $\chi(1)$)is concerned. But

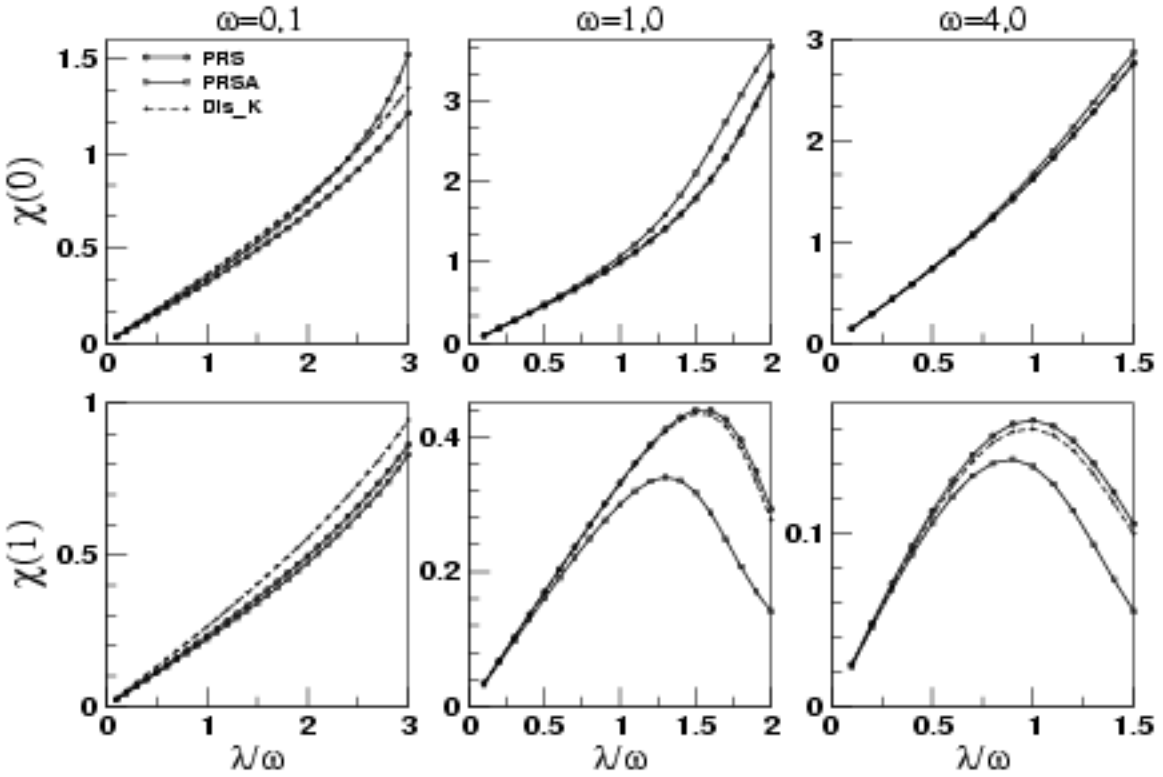

Figure 4.8: Figure compares the χs between chemically uniform, chemically alternating and reciprocal-space disordered (Chakrabarti *et al* 2006) results. The upper row shows the χ (0) at three different ω . Lower row is for χ (1). The solid lines with squares are the present real space calculation (PRSA) for the chemically alternating case, solid lines with circles are the results of chemically uniform case (PRS) and broken lines with open plus sign are disordered reciprocal-space results.

in these limits $\chi(0)$ for the alternating lattice increases and then gradually merges with the uniform lattice at high g (Figure 4.7) (if we extrapolate from our information of the low and intermediate coupling regime, we can conjecture, that values of $\chi(0)$ and $\chi(1)$ for the disordered lattice will be same as the uniform lattice for strong electron-phonon coupling, as in these limits disorder scattering hardly affects the size of the polaron). But higher the value of the lattice vibration frequency, lesser is the relative increase in $\chi(0)$. In this limits (i.e., $\omega = 1.0$ and 4.0) there is a sharp decrease in $\chi(1)$ for the intermediate coupling regime, but the relative magnitude of decrease is less for higher values of lattice

vibration. The variation of average phonon number with the electron-phonon coupling strength shown in Figure 4.4 (upper panel), displays similar characteristics as $\chi(0)$, differing from the uniform lattice in the intermediate coupling regime and this difference decreasing with increasing oscillator frequency . The lower panel of Figure 4.4 shows the average kinetic energy. The average kinetic energy for the alternating lattice starts from a lower value (compared with its uniform counterpart), with the difference increasing up to the intermediate coupling regime and then merging at strong coupling regime.

To gain further insight of the electron-phonon interaction in the alternating lattice we will look at the lattice deformation as a function of distance from the electron site and the corresponding distribution of excited phonons about the electronic site and we will also compare them with their respective chemically uniform counterpart . Figure 4.9 shows the lattice distortion ($\chi(\mathbf{R}_i - \mathbf{R}_j)$) and Figure 4.10 shows the corresponding distribution of the excited phonons ($\gamma(\mathbf{R}_i - \mathbf{R}_j)$) for four different sets of lattice vibration frequencies and coupling strength. In the inset of each figure, the contribution to the $\chi(\mathbf{R}_i - \mathbf{R}_j)$ and $\gamma(\mathbf{R}_i - \mathbf{R}_j)$ from each type of sites are given. Figure 4.9 (a) shows electron-lattice correlation or the lattice distortion in adiabatic limit ($\omega = 0.1$) and for weak electron-phonon coupling (g= λ/ω=1.0). Here a large polaron has resulted for the alternating lattice like in the uniform lattice for the same parameter with a slightly increased $\chi(0)$, but with a subtle difference. The alternating $\chi(i\mathbf{R}_i - \mathbf{R}_j)$ has a shape, which is slightly different from the uniform lattice, it wavers a bit as it falls from its own site (i.e.,$\mathbf{R}_i - \mathbf{R}_j = 0$) to its neighbors. One can find the reason for the difference in shape if one takes a close look at the corresponding inset giving the contributions from sites with site energy ε_a (a-Type) and sites with energy ε_b (b-Type). Both the a-projected and b-projected $\chi(\mathbf{R}_i - \mathbf{R}_j)$ decays in an oscillatory manner from its electronic site. More remarkably the b-projected $\chi(1)$ is greater than $\chi(0)$, i.e., the polaron is more distorted in the nearest neighbor site of the electron than at the electron's own site. Let us try to understand this. Here $\delta\varepsilon = 1$ i.e., we have a situation where $\delta\varepsilon >> \omega$, in such a scenario the electron-phonon interaction at b-type of sites will be very weak. So whether we see a-projected or b-projected $\chi(\mathbf{R}_i - \mathbf{R}_j)$ the peaks in the oscillations are always on a-type of site. The $\gamma(\mathbf{R}_i - \mathbf{R}_j)$ and its site projections shown in Figure 4.10 (a) displays similar features, which complements our understanding of the electron-phonon interaction

process for this set of parameters. Figure 4.9 (c) shows $\chi(\mathbf{R}_i - \mathbf{R}_j)$ for the $\omega = 0.1$ and g=4.34 (i.e., $\lambda = 0.435$). In this case though the $\chi(\mathbf{R}_i - \mathbf{R}_j)$ has a similar shape as the uniform lattice for this set of parameters, but $\chi(0)$ has a significantly high value and $\chi(1)$ has a lower value compared to the uniform lattice. The electron-phonon interaction being strong one expects the formation of a small polaron. But if we see the projected picture in the inset, almost entire contribution of the $\chi(R_i - R_j)$ comes from the a-type and it does not exhibit any oscillation like it did for weak coupling as the size of the polaron is very small. But for b-type though its contribution to the $\chi(\mathbf{R}_i - \mathbf{R}_j)$ of the lattice is insignificant, its $\chi(1)$ is still greater than $\chi(0)$. Figure 4.9 (b) shows the $\chi(\mathbf{R}_i - \mathbf{R}_j)$ for $\omega = 1.0$ and g=0.5 i.e., adiabatic limit and weak electron-phonon coupling. Here the nature of the lattice distortion is similar for both alternate and uniform lattice though the alternate lattice has $\chi(0)$ slightly enhanced and $\chi(1)$ slightly reduced. The contribution from a-type is much higher than from b-type but nature of both types are same. Figure 4.9 (d) shows the $\chi(\mathbf{R}_i - \mathbf{R}_j)$ for $\omega = 1.0$ and g=3.0 i.e., adiabatic limit and strong electron-phonon coupling. Here there is no perceptible difference between χs of two types of lattice and the entire show is due to a-type. If we look at the probability picture shown in Figure 4.6, the b-type of sites have been totally stripped off its occupation probability and almost the entire electronic occupation is shared by the a-type of sites. So the alternating lattice basically behaves like a lattice with only a-types of sites, with double lattice spacing and almost zero hopping (i.e., almost zero kinetic energy as reflected in Figure 4.4). The $\gamma(\mathbf{R}_i - \mathbf{R}_j)$ in Figure 4.10 exhibits similar feature as the $\chi(\mathbf{R}_i - \mathbf{R}_j)$ for all cases, but for large polarons the excited phonon are less spread about the electronic site than the lattice distortion.

Till now we tried to study the effect of electron-phonon interaction in the alternating lattice by varying the strength of the electron-phonon interaction from very low to high values. Now we will endeavor to see it from a different perspective , we will vary the parameter $\delta\varepsilon$ at different fixed oscillator frequency (ω) and electron-phonon interaction strength (λ), which is shown in Fig4.11. The figure shows the variation of $\chi(0)$,$\chi(1)$ and the site projected probability as a function of $\delta\varepsilon$. The first column is for ω=0.1 and λ=0.1, i.e., adiabatic limit and weak electron-phonon coupling. Here the difference in site energies has a significant effect on the polaronic distortion. The variation in polaronic

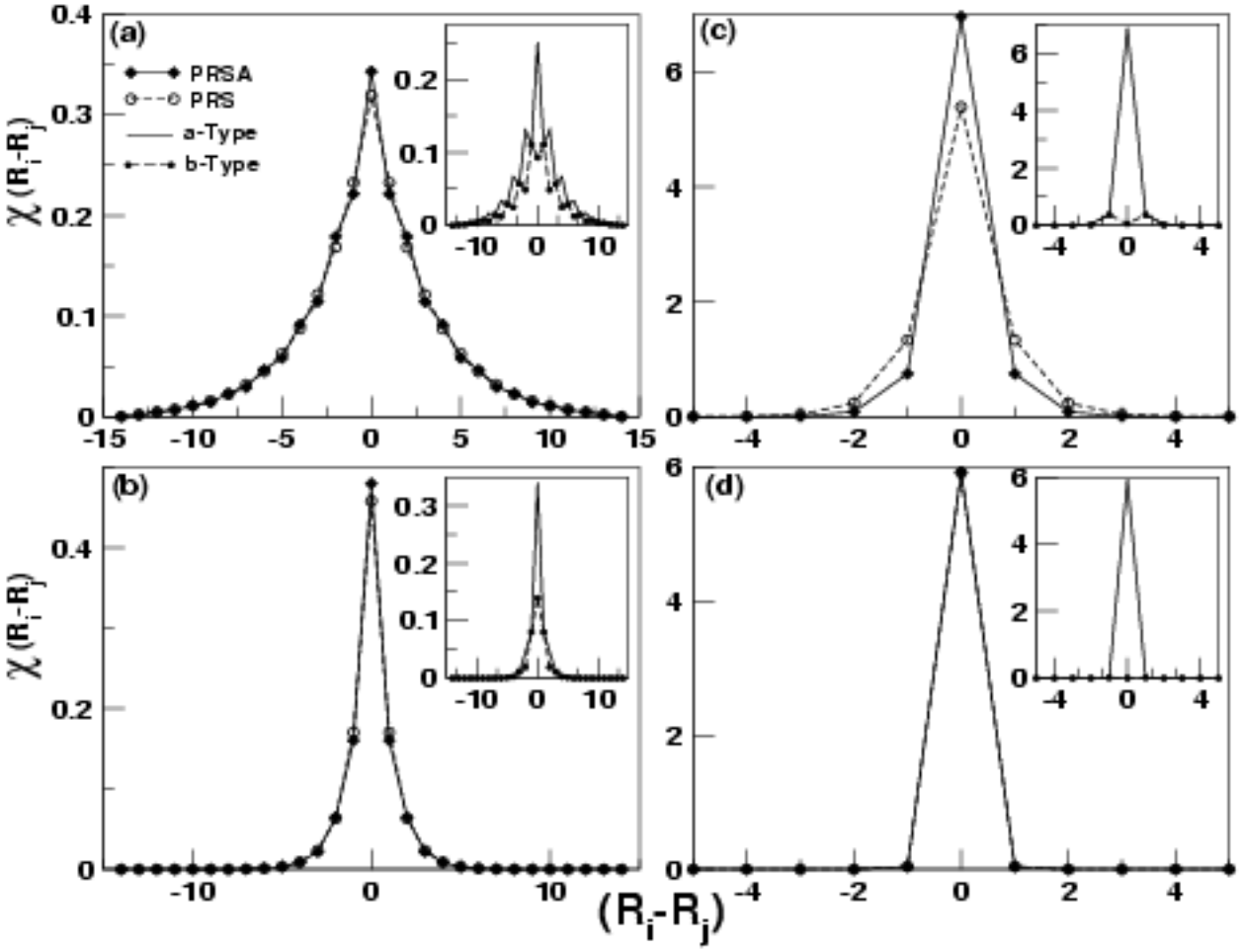

Figure 4.9: The Lattice deformation $\chi(\mathbf{R_i} - \mathbf{R_j})$ as function of $(\mathbf{R_i} - \mathbf{R_j})$ in the ground state for (a) ω=0.1 andλ=0.1, (b)ω=1.0 and λ=0.5, (c)ω=0.1 andλ=0.435, (d)ω=1.0 and λ=3.0 Here the Present Real Space results for the uniform lattice is mentioned PRS in abbreviation, results for lattice with alternating site energies is mentioned as PRSA. The $\chi(\mathbf{R_i} - \mathbf{R_j})$ contribution from sites with energy ε_a of the alternating lattice is mentioned as a-Type and contributions from those with sites energy ε_b is mentioned as b-Type and they are shown in the inset.

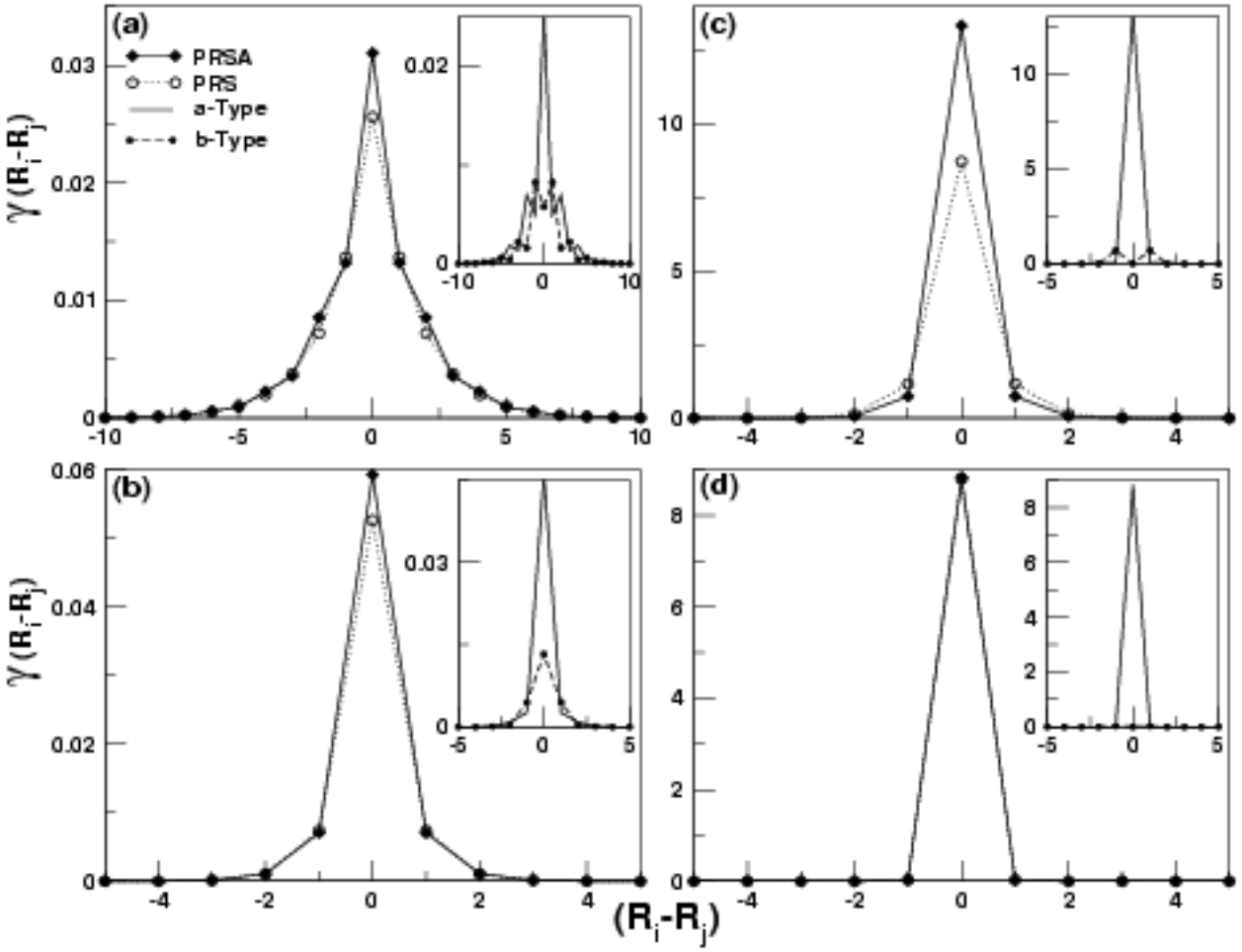

Figure 4.10: The excited phonon distribution in the vicinity of electrons, $\gamma(\mathbf{R}_i - \mathbf{R}_j)$ as function of $(\mathbf{R}_i - \mathbf{R}_j)$ in the ground state for (a) ω=0.1 andλ=0.1, (b)ω=1.0 and λ=0.5, (c)ω=0.1 andλ=0.435, (d)ω=1.0 and λ=3.0 . Here the Present Real Space results for the uniform lattice is mentioned PRS in abbreviation, results for lattice with alternating site energies is mentioned as PRSA. The $\gamma(\mathbf{R}_i - \mathbf{R}_j)$ contribution from sites with energy ε_a of the alternating lattice is mentioned as a-Type and contribution from sites energy ε_b is mentioned as b-Type and they are shown in the inset.

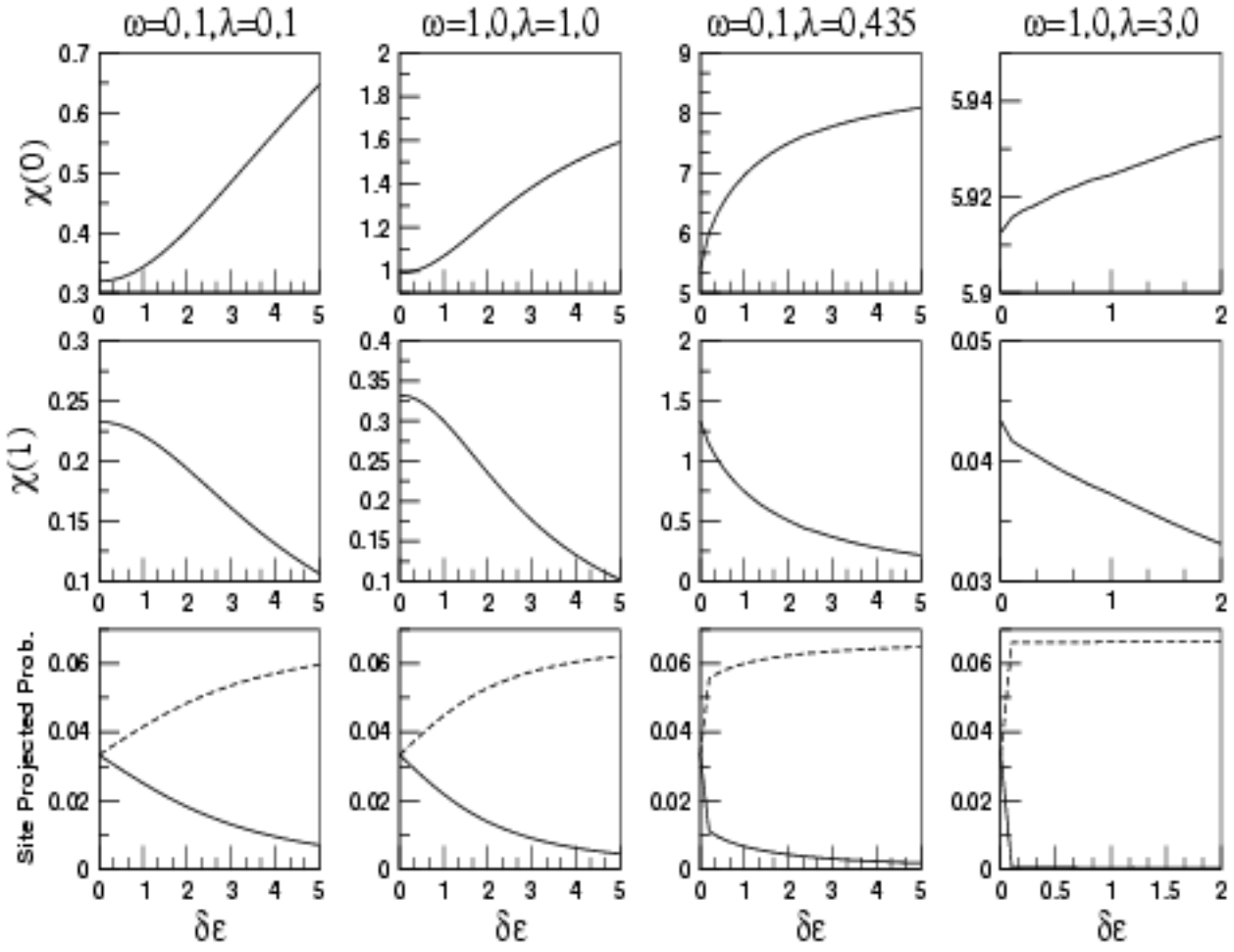

Figure 4.11: The variation of $\chi(0)$ (first row), $\chi(1)$ (second row) and the the site projected probability (third row) with respect to $\delta\varepsilon$. In the third row broken line shows the variation of a a-projected site w.r.t $\delta\varepsilon$ and the solid line that of a b-projected site.

correlation functions ($\chi 0$) and $\chi(1)$) and the site projected probability, though marked, is smooth as a function of $\delta\varepsilon$. But just as we switch on the $\delta\varepsilon$ parameter, there is a slight non-linearity in the polaronic correlation functions. The site-projected probability slowly saturates (by saturation we mean the total flow of probability from b-type of site to a-type of site) with increase in $\delta\varepsilon$, but the nature is again non-linear. The probability saturation is not complete even for $\delta\varepsilon = 5.0$.

The second column is for ω=1.0 and λ=1.0, i.e., intermediate limit and intermediate electron-phonon coupling. Here all the features are similar as the previous case, but the polaronic correlation functions show less change and the probability changes are faster (with respect to $\delta\varepsilon$).

The third column is for ω=0.1 and λ=0.435, i.e., adiabatic limit and strong electron-phonon coupling. Here polaronic correlation functions exhibit a sharp change with the switching on of the energy difference (i.e., $\delta\varepsilon$) and then with further increase in $\delta\varepsilon$ the rate of change weakens. But there is a significant increase in $\chi(0)$ and a corresponding decrease in $\chi(1)$ as we change the $\delta\varepsilon$ from zero to non-zero values. Here the site-projected probability profile registers a very sharp and immediate change, as $\delta\varepsilon$ takes a small non-zero value, the hallmark of strong electron-phonon coupling.

The fourth column is for ω=1.0 and λ=3.0, i.e., intermediate limit and strong electron-phonon coupling. Here polaronic correlation functions hardly change with the energy difference (i.e., $\delta\varepsilon$). Here also the site-projected probability profile registers a very sharp change when $\delta\varepsilon$ takes a small non-zero value, but here the change in the probability profile is sharper and the saturation is immediate. From here we can conclude that, in the strong electron-phonon coupling regime, when we are away from adiabatic limit, the electron-phonon coupling picture is hardly affected by the nature of its site occupation (i.e., whether it is disordered or vary in an alternating manner).

4.3.3 Study of a tri-layer thin film

We have studied the effect of electron-phonon interaction in a tri-layered (001) thin film. Here we have periodic boundary condition along x and y-directions. Along the z-direction we have considered three layers with open boundary. In the x-y plane we have

considered up to 8×8 lattice. In case of a tri-layer we reap the real benefit of developing a real space scheme, because this a system, where the translational symmetry breaks.

We know that the dimensionality of a system has an effect on the electron-phonon interaction (Li-Chung *et al* 2002). A thin film being a quasi two dimensional system should be an interesting study. Ideally one should vary the thickness of the film to see how the interactions evolve as a function of thickness. But anything beyond a tri-layer would be computationally very expensive. And for the tri-layer also we couldn't go beyond 8×8 size in x-y plane. We would like to emphasize on the qualitative features of the tri layer and how its correlation functions differ from its 2-d (10×10) and 3-d (7×7×7) counterparts.

Method	ω	λ/ω	Energy (2-d)	Energy (tri)	Energy (3-d)
VAED	2.0	1.0	-4.814735778337	-	-
PRS	2.0	1.0	-4.814736	-6.0585	-6.5885
VAED	3.0	1.0	-	-	-7.1623948409
PRS	3.0	1.0	-5.52533	-6.6687	-7.16236

Table 4.2: Polaron Ground state energies for for two different set for 2-d,3-d and a tri-layered system.

The calculated ground state energies of 2-d , 3-d and tri-layered Holstein model are shown in Table-4.2 for different sets of parameters and are compared with the available results of Li-Chung *et al* 2002 (VAED). For the 2-d lattice our calculated energy for the ground state matches up to six digit with the VAED for ω=2.0 and λ/ω=1.0 and for 3-d our result matches up to four digit with the VAED result for ω=3.0 and λ/ω=1.0. All the ground state energies that we have mentioned in Table-4.2 has at least a convergence of four digit with its previous shell calculations. So when we discuss the correlation functions or the layer projected occupation probabilities we will be interested, only in their qualitative features in the weak electron-phonon coupling regime. However from our knowledge of the alternating 1-d lattice we will try to predict the properties of the tri-layer for higher electron-phonon coupling.

Figure 4.12 shows the ground state probability of the central (middle or the second layer) and surface sites as a function of the electron-phonon coupling strength at different oscillator frequencies. We can see that the probability of the sites of the central

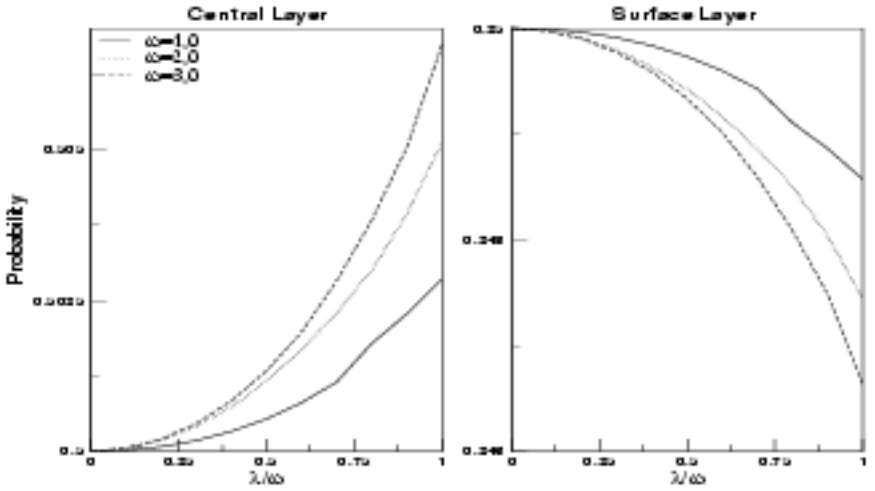

Figure 4.12: The variation of the site projected probability in the central layer(left) and the surface layers(right) at different oscillator frequencies.

layer increases with electron-phonon coupling as well as oscillator frequencies and there is a corresponding decrease in the probability of the sites in the surface layers. In the previous section we encountered a situation where there was a difference in occupation probability among the constituent sites due to the difference in site energies and here we see a similar effect due to a different reason, i.e., surface effect (the sites sitting on the surface lose some of their nearest neighbours). We can say from our experience of the alternating lattice that with increasing electron-phonon coupling the probability flow from the surface layers to the central layer will go on increasing and at very high electron-phonon coupling almost whole of the probability will flow to the central layer thus virtually rendering the quasi two dimensional tri-layer almost two-dimensional.

Figure 4.13 shows the polaronic distortion at the electron site (i.e., $\chi(0)$) and at its nearest neighbour site (i.e., $\chi(1)$) in the tri-layer and is compared with the same correlation functions in 2-d and 3-d. Again these correlation functions are shown for only low electron-phonon coupling. The $\chi(0)$ for the tri-layer lies between the 3-d and 2-d values but slightly nearer to the 3-d values than the 2-d. However the values of $\chi(1)$ are

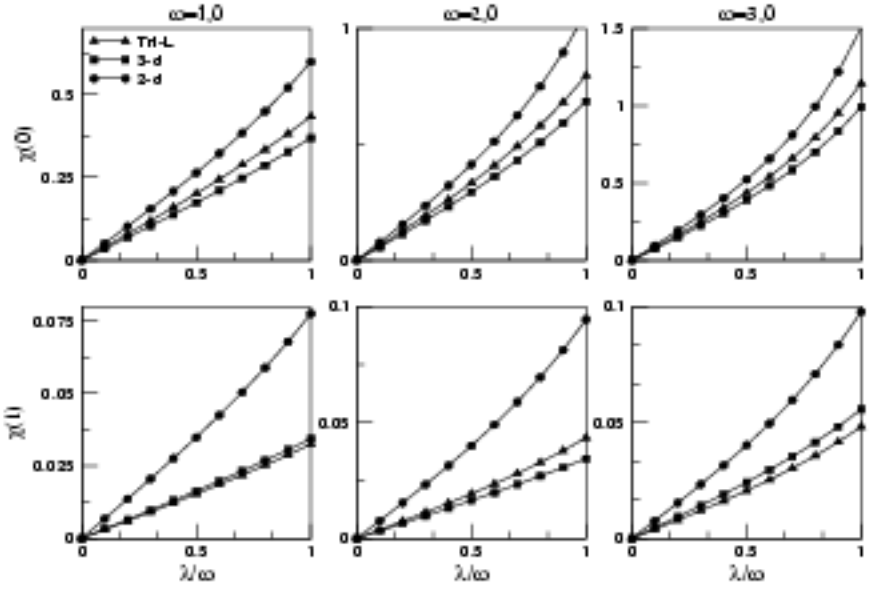

Figure 4.13: The variation of $\chi(0)$ (top row) and $\chi(1)$ (bottom row) of the trilayered thin film(Tri-L) with electron-phonon coupling, at different oscillator frequencies. They are compared with their 2-d and 3-d counterparts.

definitely much more closer to 3-d values than the 2-d ones. This is because the central layer of the tri-layer which is always favoured as far as the occupation probability is concerned, has always six nearest neighbour a characteristic of the 3-d lattice. But again, we have the gut feeling that, at sufficiently high electron-phonon coupling the tri-layer will start behaving like a 2-d lattice as we think in that regime the surfaces will be almost stripped off its occupation probability.

4.4 Reciprocal-space versus real space calculations

We have developed a method to study the effect of interaction among the electronic and lattice degrees of freedom, which does not take recourse to any translational symmetry of the underlying lattice. Now let us weigh its advantages as well as disadvantages with the much successful reciprocal-space approach.

- Since we have studied the electron-phonon interactions in different systems numerically, the reciprocal-space approach is more efficient as here the lattice degrees of

freedom are integrated out.

- A reciprocal-space study can give us information about spectral functions from which we can get the dispersion relations and the effective mass. In real space calculations we do not have access to such informations.

- The applicability of reciprocal-space methods is limited to cases where the underlying lattice is translationally symmetric. There are many examples in nature like topologically disordered systems where one does not have lattice-translational symmetry. Here real space scheme is the only technique available.

4.5 Conclusion

We have developed a real space scheme to study the Holstein polarons. Our calculated results are in excellent agreement with the most recent results for the uniform 1-d lattice. We have studied a 1-d lattice with alternate site having different energies and the effect of the energy difference on the electron-phonon interaction. This effect is most prominent in the intermediate electron-phonon coupling regime but with the increasing oscillator frequency the effect is reduced. However the energy difference between the alternate sites has the maximum effect on the probabilities of sites with different energies in the strong coupling regime. Since our scheme is entirely based on real space we could implement it on a tri-layered thin film. Here, however we could probe only in the weak electron-phonon coupling. Our real space based methodology holds out a promise, as it can be implemented to cases where k-space based method would fail due to lack of translational symmetry.

Chapter 5

An assessment and future plans

5.1 Concluding remarks

In this chapter, we shall assess our work. We shall discuss what we initially planned to work, how much we have achieved, indicate what were the limitations of our work, try to decide how to overcome these limitations, and finally lay out our future plans.

Our aim was to develop a theoretical scheme to study the electronic structure and magnetic properties of thin films and surfaces of ordered and disordered materials as well as to develop a methodology to study the effect of interaction of the electronic and the lattice degrees of freedom in model system where one cannot afford the comfort of translational symmetry. We have used and developed the recursion method married to the TB-LMTO to study the orbital resolved picture of magnetism in thin films and surfaces of different materials. We have also developed a scheme using the TB-LMTO Hamiltonian in conjunction with augmented space recursion to study disordered thin films. We went on to develop a real space scheme, which could predict the effect of electron-phonon interaction with the accuracy of reciprocal space. In the following, we would like to briefly describe the steps we followed to reach to our goal :

In chapter 2 we have used the recursion technique, an entirely real space based method, to extract more detailed information about surface magnetism of transition metal elements. With recursion we could easily take care of the broken translational symmetry at the surfaces and study how different orbital components of the surface states participate in the magnetic enhancement (or otherwise) at the surface. Most of the real surfaces are

not planar (i.e., they are rough), and recursion being a real space method can take care of rough surfaces. In chapter 2 we have studied rough surfaces of Ni and Fe in (001) plane and have seen the effect of specific rough structures on surface magnetism.

In chapter 3 we have presented the ASR formulation in conjunction with the TB-LMTO Hamiltonian to study the electronic structure of materials where there are more than one atom in a unit cell. Our formulated scheme can treat total as well as partial disorder with equal ease. We have studied the bulk as well as thin films of $Co_2Cr_{0.6}Fe_{0.4}Al$ a doped quaternary Heusler alloy applying this methodology. Here we could study the effect of partial disorder in the $L1_2$ phase in bulk and the corresponding surface in this phase. Here we could predict the effect of alloying on the specific orbitals. For the thin film the surface effects along with the effect of alloying could be clearly seen with our technique.

In chapter 4 we developed a real space method to study the effects of electron-phonon interaction of a Holstein polaron to systems where there is no translational symmetry. Here for the 1-d lattice we obtained convergent results in all parametric regimes. Most earlier techniques, though very accurate in certain parametric regimes, tended to fail in others. Our method bridges different regimes with ease.

We studied the alternating 1-d lattice and the effect of difference in energies of the alternate sites on the polaron. We compared them with the results of the disordered chain of Chakrabarti *et al* 2006. We have taken advantage of our real-space scheme and have studied the electron-phonon interaction in a tri-layer in the weak coupling regime.

5.2 Future directions

As we have already mentioned, we have developed a methodology to deal with substitutional disorder as well as partial disorder for materials with many atom per unit cell. We have not yet achieved full self-consistency. The main problem in formulating a self-consistent scheme is with the Madelung energy term. In a many-atom per unit cell there will be inter-cell as well as intra-cell contributions to the Madelung energy term. In future we will try to incorporate these terms into our self-consistency scheme to study the electronic structure of disordered and partially ordered materials with many atoms per

unit cell.

For the tri-layer thin film we studied the effect of electron-phonon interaction in the weak coupling regime. For a cubic (001) thin film there is a remnant planar symmetry in the x-y direction. So to make the problem computationally feasible we will to try to take advantage of this planar symmetry. We will reformulate our real space scheme and would adopt a reciprocal-space approach in the x-y direction while treating the z-direction in real space. We would also like to apply this scheme to study smooth(i.e., planar) thin films of disordered materials.

Bibliography

Alden M, Mirbt S, Skriver H L, Rosengaarg N M and Johansson B, *Phys. Rev. B* **46**, 10, 6303 (1992)

Alexandrov A S and Mott N F, *Rep. Prog. Phys.* **57**, 1197 (1994)

Alexandrov A S and Mott N F, *Polarons and Bipolarons* (World Scientific, Singapore, 1995)

Alexandrov A S, Kabanov V V and Ray D E, *Phys. Rev. B* **49**, 9915 (1994)

Alldredge G P and Kleinman L, *Phys. Rev. Lett.* **28** 1264 (1972)

Andersen O K, *Phys. Rev. B* 12 3060 (1975)

Andersen O K and Jepsen O, *Phys. Rev. Lett.* **53** 2571 (1984)

Andersen O K, in *The Electronic Structure of Complex Systems*, ed. Phariseau P and Temmerman W M, (Plenum, New York, 1984), p.11.

Andersen O K, Jepsen O and Söb M, in *Electronic Band Structure and Its Applications*, Vol. 283 of *Lecture Notes in Physics*, Ed. Yussouff M (Springer Verlag, Berlin, 1987), p.1. *Note :* A revised version of this article is published as lecture notes for *CECAM Workshop on Interatomic Forces*, (1987)

Antonov V N, Durr H A, Kucherenko Yu, Bekenov L V and Yaresko A N u, *Phys. Rev. B* 72 054441 (2005)

Baryam Y, Egami T, de Leon J Mustre and Bishop A R, edited *Lattice Effects in High T_c Superconductors* (World Scientific, Singapore) (1992)

Beer N and Pettifor D G, (1982), in *The Electronic Structure of Complex Systems*, ed. Phariseau P. and Temmerman W.M., NATO ASI Series B, v.113, p 769 (1982)

Bonca J, Trugman S A and Batistic I, *Phys. Rev. B* **60** 1633 (1999)

Bronold F X, Saxena A and Bishop A R, *Phys. Rev. B* **63**, 235109 (2001)

Campbell I H and Smith D L, *Solid State Phys.* **55**, 1 (2001).

Capone M, Stephan W and Grilli M, *Phys. Rev. B* **56**, 4484 (1997)

Carruthers E B, Dempsey D G and Kleinman L, *Phys. Rev. B* **14** 288 (1976)

Chakrabarti A and Mookerjee A, *J. Phys.: Condens. Matter* 3211 (2002)

Chakrabarti A and Mookerjee A, *Eur. Phys. Journal B* **44**, 21 (2005)

Chakrabarti A, Chakraborty M and Mookerjee A, *Physica B : Solid State* (2006)

Chakraborty M, Mookerjee A and Bhattacharya A K, *Int. J. Mod. Phys. B* **17** , 31 & 32 (2003)

Chakraborty M, Mookerjee A and Bhattacharya A K, *J. Magn. Magn. Mater.* **285** , 210 (2005)

Chatterjee J and Das A N, *Eur. J. Phys. B* **50** 2024 (2005)

Das G P in *Electronic Structure of Clusters, Surfaces and Alloys* ed. Sarma D D and Mookerjee A (Taylor-Francis) (1998)

Datta S and Das B *Appl. Phys. Lett.* **56** 665(1990)

de Mello E V L and Ranninger J, *Phys. Rev. B* **55**, 872 (1997)

de Groot R A, Mueller F M, van Engen P G and Buschow K H J, *Phys. Rev. Lett.* **50** 2024 (2004)

De Raedt H and Langedijk A, *Phys. Rev. Lett.* **49**, 1522 (1982)

De Raedt H and Langedijk A, *Phys. Rev. B* **27**, 6097 (1983)

De Raedt H and Langedijk A, *Phys. Rev. B* **30**, 1671 (1984)

Elmers H J, Fecher G H, Valdaitsev D, Nepijko S A, Gloskovskii A, Jakob G, Schonhense G, Wurmehl S, Block T, Felser C, Hsu P -C, Tsai W -L and Cramm S, *Phys. Rev. B* **67**, 104412 (2003)

Eriksson O, *Solid State Commun.* **78**, 801 (1991)

Ernst A, *J. Phys.: Condens. Matter* **12**, 5599-5605 (2000)

Falicov L M and Morán-Lopez J L, ed. *Magnetic Properties of Low-Dimensional systems* (Springer-Verlag, Berlin) (1986)

Felser C, Heitkamp B, Kronast F, Schmitz D, Cramm S, Drr H A, Elmers H-J, Fecher G H, Wurmehl S, Block T, Valdaitsev D, Nepijko S A, Gloskovskii A, Jakob G, Schnhense G and Eberhardt W, *J. Phys: Condens. Matter* **15** 7019 (2003)

Ghosh S, Das N and Mookerjee A, *J. Phys.: Condens. Matter* 10, 701 (1977)

Gunnarsson O, Jepsen O and Andersen O K, *Phys. Rev. B* 27 (1983)

Haydock R, Heine V and Kelly M J, *J. Phys: Condens. Matter* **5**, 28452845 (1972)

Haydock R, *Solid State Physics* ed. Ehrenreich H, Seitz F and Turnbull D, (Academic Press, New York) **35** (1980)

Haydock R and Te R L, *Phys. Rev. B* **49** 10845 (1994)

Hirohata A, Kurebayashi H, Okamura S, Kikuchi M, Masaki T, Nozaki T, Tezuka N and Inomata K, *J. Appl. Phys.* **97** 103714 (2005)

Hohenberg P and Kohn W, *Phys. Rev.* **136**, B864 (1964).

Holstein T, *Ann. Phys.* (NY) 8 325 (1959)

Howson M A, *Contemporary Physics* **35**, number 5,347-359(1994)

Huda A and Mookerjee A, *J. Magn. and Magn. Mater.* **267**, 97 (2003)

Inomata K, Okamura S, Goto R and Yezuka N, *Jpn. J. Appl. Phys., Part 2* **42**, L419 (2003)

Jaime M, Hardner H T, Salamon M B, Rubinstein M, Dorsey P and Emin D, *Phys. Rev. Lett.* 78, 951 (1997).

Jeckelmann E and White S R, *Phys. Rev. B* **57**, 11, 6376 (1998)

Jepsen O, Madsen J and Andersen O K, *Phys. Rev. B* **26** 2790 (1982)

Johnson M, *I.E.E.E.* **37** 33(2000)

Kelekar R and Clemens B M, *J. Appl. Phys.* **96**, 540 (2004)

Kleinman L and Carruthers E B, *Phys. Rev. B* 10, 3213 (1972)

Kobayashi K, Umetsu R Y, Kainuma R, Ishida K, Oyamada T, Fujita A, and Fukamichi K, *Appl. Phys. Lett.* **85** 4684 (2004)

Kohn W and Sham L J, *Phys. Rev.* 140, A1133 (1965).

Kornilovitch P E and Pike E R, *Phys. Rev. B* **R8634**, 21 (1997)

Kubota H, Nakata J, Oogane M, Ando Y, Sakuma A and Miyazaki T, *Jpn. J. Appl. Phys., Part 2* **43**, L984 (2004)

Li C and Freeman A J, *J. Magn. Magn. Mater.* **75** , 53 (1988)

Li-Chung Ku, Trugman S A, Bonca J, *Phys. Rev. B* **65**, 174306-1 (2002)

Liebermann L N, Fredkin D R and Shore H B, *Phys. Rev. Lett.* **22**, 539 (1969)

Liebermann L N, Clinton J, Edwards D M and Mathon J, *Phys. Rev. Lett.* **25**, 232 (1970)

Louie S G, Ho K M, Chelikowsky J R and Cohen M L, *Phys. Rev. B* **15**, 5627 (1977)

Louie S G, *Phys. Rev. Lett.* 40, 1525 (1978)

Ma C Q, Ramana M V, Cooper B R and Krakauer H, *Phys. Rev. B* **34**, 3854 (1986)

Marsiglio F, *Physica C* **244**, 21 (1995)

Miura Y, Nagao K and Shirai M, *Phys. Rev. B* **69**, 144413 (2004)

Mookerjee A, *J. Phys: Condens. Matter* **6**, L205 (1973)

Mookerjee A, *J. Phys.: Condens. Matter* **2**, 897 (1990)

Ohnishi S and Freeman A J, *Phys. Rev. B* **28**, 6741 (1983)

Pickett W E and Singh D J, *Phys. Rev. B* **53**, 1146 (1996)

Plogmann S, Schlatholter T, Braun J, Neumann M, Yarmoshenko Y M, Yablonskikh M V, Shreder E I, Kurmaev E Z, Wrona A and Slebarski A, *Phys. Rev. B* **60**, 6428 (1999)

Prinz G A, *Science* **282**, 1660 (1998)

Ramirez A P, *J. Phys.: Condens. Matter* **9** , 8171 (1997)

Rashba E I, *Phys. Rev. B* **62**, R16267 (2000)

Romero A W, Brown D W and Lindenberg K, *J. Chem. Phys.* **109**, 6540 (1998)

Sanyal B, Biswas P P, Fakhruddin M, Halder A, Ahmed M and Mookerjee A, *J. Phys.: Condens. Matter* 7, 8569 (1995)

Schlüter M, Chelikowsky J R, Louie S G and Cohen M L, *Phys. Rev. Lett.* **34**, 1385 (1975)

Schmidt G, Ferrand D, Molenkamp L W, Filip A T and van Wees B J, *Phys. Rev. B* **62**, R4790 (2000)

Schwarz K, *J. Phys. F: Met. Phys.* **16**, L211 (1986)

Shirai M, Ogawa T, Kitagawa I and Suzuki N, *J. Magn. Magn. Mater.* 177, 1383 (1998)

Shirai M, *J. Appl. Phys.* **93**, 6844 (2003)

Skriver H L and Rosengaard N M, *Phys. Rev.* **43**, 9538 (1991)

Viswanath V S and Müller G, *The user friendly recursion method : a cookbook for eclecticists*, Troisieme Cycle de la Physique, En Suisse Romande (1993)

von Barth U and Hedin L, *J. Phys: Condens. Matter* **C 5**, 1629 (1972)

Wang C S and Freeman A J, *Phys. Rev. B* **24** , 4364, (1981)

Wang C S and Freeman A J, *Phys. Rev. B* **21** 4585 (1985)

Wellien G, Roder H, and Fehske H, *Phys. Rev. B* **53**, 9666 (1996)

Wellien G and Fehske H, *Phys. Rev. B* **56**, 4513 (1997)

Wellien G and Fehske H, *Phys. Rev. B* **58**, 6802 (1998)

Wimmer E, Freeman A J, and Krakauer H, *Phys. Rev. B* **30**, 3113 (1984)

Wimmer E, Krakauer H, Weinert M and Freeman A J, *Phys. Rev. B* **24**, 864 (1981)

Wurmehl S, Fecher G H, Kroth K, Kronast K, Durr H A, Takeda Y, Saitoh Y, Kobayashi K, Lin H J, Schonhense G and Felser C, *J. Phys. D: Appl. Phys.* **39**, 803 (2006)